Summer 8-1-2023

CHARACTERISTICS OF REFRACTIVITY AND SEA STATE IN THE MARINE ATMOSPHERIC SURFACE LAYER AND THEIR INFLUENCE ON X-BAND PROPAGATION

Douglas Matthew Pastore
Coastal Carolina University

CHARACTERISTICS OF REFRACTIVITY AND SEA STATE IN THE MARINE ATMOSPHERIC SURFACE LAYER AND THEIR INFLUENCE ON X-BAND PROPAGATION

By

Douglas Matthew Pastore

Submitted in Partial Fulfillment of the

Requirements for the Degree of Doctor of Philosophy in

Marine Science: Coastal and Marine Systems Science in the

Gupta College of Science

Coastal Carolina University

2023

X

Erin Hackett, Coastal Carolina University
Major Advisor

X

Louis Keiner, Coastal Carolina University
Committee Member

X

Robert Burkholder, Ohio State University
Committee Member

X

Keshav Jagannathan, Coastal Carolina University
Committee Member

X

Qing Wang, Naval Postgraduate School
Committee Member

X

Erin Hackett, Coastal Carolina University
CMSS Graduate Program Director

X

Chad Leverette, Coastal Carolina University
Dean, Gupta College of Science

Dedication

This work is dedicated to my parents, Daniel and Karen Pastore. Their unwavering love and support have given me the opportunity to pursue my goals, making this work possible.

Acknowledgements

I would like to begin by thanking my advisor Professor Erin Hackett. I would not be the successful student, scientist, or person I am today if not for working with you for the last 6 years. Your work ethic, attention to detail, and high expectations have shown me how to elevate my work to levels I did not think I could achieve. It has been a great privilege learning from you and hope to continue to do so in the future. I would also like thank my committee members Professors Robert Burkholder, Qing Wang, Louis Keiner, and Keshav Jagannathan. They have helped me through the Ph.D. process and aided in the research I am privileged to put forth in this dissertation. Specifically acknowledging Professors Burkholder and Wang as well as Tracy Haack for providing data from the CASPER East field experiments, which this work focuses on. I would like to thank Coastal Carolina University for funding my Ph.D. and giving me the opportunity to teach as I have thoroughly enjoyed working with undergraduate students pursuing their educational goals. I would also like to thank the Office of Naval Research for helping to fund this research (grant numbers: N00014-16-1-2075 and N00014-19-1-2350).

Throughout this process I have received so much support from the faculty, staff, and students here in the Marine Science Graduate Program. To the faculty and staff, thank you for the assistance and support throughout the courses here at CCU. My success is directly related to this support and my degree would not be possible without it. To all the graduate students I have known in my five and half years in the Ph.D. program, I cannot thank you enough for the friendships and collegiality you have all offered. To the students in the EFL that have been a staple in my life during this time, you have endlessly helped me break through my educational and research goals, as well as helped me tackle any obstacles in life along the way, thank you. Specifically, I would like to thank Mathew Stanek, Ian Matsko, AJ Kammerer, Danny Greenway, Sarah Wessinger, Maddie Bruno, and Lexi Vaughan for their support and aid in my work. I will always be grateful to these people and the friends I have made over the past seven years here at Coastal Carolina University.

Abstract

Predictions of environmental conditions within the marine atmospheric surface layer (MASL) are important to X-band radar system performance. Anomalous propagation occurs in conditions of non-standard atmospheric refractivity, driven by the virtually permanent presence of evaporation ducts (ED) in marine environments. Evaporation ducts are commonly characterized by the evaporation duct height (EDH), evaporation duct strength, and the gradients below the EDH, known as the evaporation duct curvature. Refractivity, and subsequent features, are estimated in the MASL primarily using four methods: *in-situ* measurements, numerical weather and surface layer modeling, boundary layer theory, and inversion methods.

The existing refractivity estimation techniques often assume steady homogeneous conditions, and discrepancies between measured and simulated propagation predictions exist. These discrepancies could be attributed to the exclusion of turbulent fluctuations of the refractive index, exclusion of spatially heterogeneous refractive environments, and inaccurate characterization of the sea surface in propagation simulations. Due to the associated complexity and modeling challenges, unsteady inhomogeneous refractivity and rough sea surfaces are often omitted from simulations.

This dissertation first investigates techniques for steady homogeneous refractivity

and characterizes refractivity predictions using EDH and profile curvature, examining their effects on X-band propagation. Observed differences between techniques are explored with respect to prevailing meteorological conditions. Significant characteristics are then utilized in refractivity inversions for mean refractivity based-on point-to-point EM measurements. The inversions are compared to the other previously examined techniques. Differences between refractivity estimation methods are generally observed in relation to EDH, resulting in the largest variations in propagation, where most significant EDH discrepancies occur in stable conditions. Further, discrepancies among the refractivity estimation methods (*in-situ*, numerical models, theory, and inversion) when conditions are unstable and the mean EDH are similar, could be attributed to the neglect of spatial heterogeneity of EDH and turbulent fluctuations in the refractive index. To address this, a spectral-based turbulent refractive index fluctuation model (TRIF) is applied to emulate refractive index fluctuations. TRIF is verified against *in-situ* meteorological measurements and integrated with a heterogenous EDH model to estimate a comprehensive propagation environment. Lastly, a global sensitivity analysis is applied to evaluate the leading-order effects and non-linear interactions between the parameters of the comprehensive refractivity model and the sea surface in a parabolic wave equation propagation simulation under different atmospheric stability regimes (stable, neutral, and unstable). In neutral and stable regimes, mean evaporation duct characteristics (EDH and refractive gradients below the EDH) have the greatest impact on propagation, particularly beyond the geometric horizon. In unstable conditions, turbulence also plays a significant role. Regardless of atmospheric stability, forward scattering from the rough sea surface has a substantial effect on propagation predictions, especially within the lowest 10 m of the atmosphere.

Table of Contents

List of Figures

List of Tables

Chapter 1

Introduction

Nomenclature	Definition
ED	Evaporation Duct
EDH	Evaporation Duct Height
EDS	Evaporation Duct Strength
eFAST	Extended Fourier Amplitude Sensitivity Test
EM	Electromagnetic
MASL	Marine Atmospheric Surface Layer
MOST	Monin Obukhov Similarity Theory
NWP	Numerical Weather Prediction
OAT	One-At-A-Time
p	Pressure
PTP	Point-to-Point
PWE	Parabolic Wave Equation
q	Specific humidity
RF	Radio Frequency
T	Temperature
TRIF	Turbulent Refractive Index Fluctuation
U	Wind speed

Accurate representation of the environment is an essential part of optimizing X-band radar system performance within the marine atmospheric surface layer (MASL). The

MASL is a dynamic and turbulent region dominated by temporally and spatially varying momentum, heat, and water vapor exchange between the ocean and atmosphere, making it difficult to accurately predict or model surface layer processes. Vertical variations in temperature (T), pressure (p), wind speed (U), and specific humidity (q) in the marine environment are commonly studied due to their importance in ocean-atmosphere exchange as well as their strong influence on electromagnetic (EM) wave propagation (Hitney et al., 1985; Fairall et al., 1996; Wang et al., 2018). At X-band frequencies, anomalous propagation in the MASL is caused by refraction of EM waves due to the rapid decrease in humidity over the ocean causing evaporation ducts (ED), which are common in the marine environment. Effects of EDs are typically characterized by evaporation duct height (EDH) and M-deficit (sometimes referred to as evaporation duct strength) (Cherrett, 2015).

Estimation of MASL meteorological profiles, and associated refractivity (including EDH), has become the focal point of meteorological predictive capabilities in application to EM propagation. Previous research has explored *in-situ* measurement techniques to estimate p, T, and q in the MASL where most often radiosondes mounted on rockets, tethered or untethered weather balloons or kites, or ship- or buoy- based mast towers are used (Edson et al., 2004; Kang and Wang, 2016; Wang et al., 2018). Further, semi-empirical surface layer models have been developed to represent the mean state of vertical variations of wind, humidity, and temperature within the lowest ~50 m of the atmosphere (Fairall et all, 1996; Fairall et al., 2003; Frederickson et al., 2016). These models apply Monin Obukhov similarity theory (MOST) to estimate surface fluxes using universal, non-dimensional functions based-on measured bulk environmental parameters (i.e., mean T, p, q, U, and sea-surface properties). Numerical weather prediction (NWP) models are also

employed to estimate MASL refractivity and are often augmented with MOST profiles through a blending process to resolve physical phenomena such as EDs (Hodur et al., 1997; Karimian et al., 2013).

The described meteorological estimation techniques employed within the MASL are susceptible to errors from simplifications and limitations. For *in-situ* measurement systems, measurement uncertainty, logistical challenges, and limited temporal and spatial coverage make it difficult to collect the information needed to accurately predict propagation from *in-situ* measurements (Stanek et al., 2023). In semi-empirical and NWP models, temporal and spatial resolution is often lacking (although spatial resolution tends to be better than *in-situ* measurements) and are susceptible to approximations, assumptions, and simplifications of the models (Gerstoft et al., 2003; Pastore et al., 2022). To overcome these limitations, inverse methods that utilize simulated and measured EM data to back-out the refractive environment have become more prevalent (Gerstoft et al., 2003A; Fountalakis and Earls, 2016; Wagner et al., 2016; Zhang and Yang, 2018; Matsko and Hackett, 2019; Pastore et al., 2022). Theoretically, refractivity inversions could capture short-timescale and small spatial variations in the refractive index due to the nearly instantaneous sampling in time (i.e., EM waves travel at the speed of light), and high sensitivity to small spatial variations on the order of the RF wavelength. These resolutions and sensitivities are near impossible to attain via the other methods, creating an opportunity for increased precision and accuracy of refractivity estimation using inversion techniques.

In contrast, EM inversions are limited by their description of the refractive environment, which is performed via a parametric model. Thus, inversion techniques have developed in parallel with refractive parameterizations in the MASL (Gerstoft et al.,

2003B; Zhang et al., 2011; Saeger and Hackett, 2015; Wessinger et al., 2022). Most parametric refractivity models are range homogenous and solely include mean refractivity characteristics – such as evaporation duct height, evaporation duct strength (EDS), and near surface refractive gradients (describing profile shape), which have been shown to have first-order effects on propagation (Turton et al., 1988; Whalen, 1998; Lentini and Hackett, 2015). These models commonly disregard parameters describing spatial inhomogeneity and turbulence assuming these processes have negligible effects on propagation. Thus, discrepancies between modeled and measured propagation could be due to the parametric refractivity model not encapsulating these variations in the refractive index (Chou and Kang, 2014).

Along with refractive environments influencing EM propagation in the MASL, EM interaction with the sea-surface can also affect propagation. Commonly, sea-surface effects on EM propagation within Parabolic Wave Equation (PWE) simulations are included via computation of a roughness reduction factor augmenting propagation relative to a flat surface (Freund et al., 2006; Sirkova, 2011). While this roughness reduction factor is common in the literature, it is limited by the pseudo-physical derivations of the Fresnel reflection correction parameter (i.e., reduction factor). More recently, as computing power and parabolic wave equation EM simulations have become more robust, 2-D sea-surface wave models have been implemented into PWE simulations (Lentini and Hackett, 2015; Penton and Hackett, 2018). For these wave-models, the full EM wave solutions are computed including the bottom boundary condition, realized via a wave model, producing a more physically accurate representation of the EM wave field relative to the roughness reduction factor approach.

While studies have documented the influence of atmospheric refractivity (including the effects of turbulence and spatial heterogeneity) and the sea-surface on propagation independent of one another (Chou and Kiang, 2014; He et al., 2015; Wagner et al., 2016; Penton and Hackett, 2018; Gao et al., 2019), few have looked at the coupled effects. Chou and Kiang (2014) perform experiments that include mean refractivity appended with turbulent fluctuations in the refractive index over smooth and rough sea surface conditions, revealing variations between the two scenarios. Though Chou and Kiang (2014) display these differences, they do not explicitly quantify the relative effects of each phenomenon on propagation. A novel study by Lentini and Hackett (2015) represents a first attempt at quantifying the relative importance of variations on propagation due to mean refractivity and sea-state. Lentini and Hackett (2015) employ the extended Fourier amplitude sensitivity test (eFAST) to estimate first-order and total order-sensitivity of EM propagation to refractivity and sea-state parameters. First-order sensitivity is akin to a one-at-a-time (OAT) test where one parameter is varied while others are held constant, while total order sensitivity accounts for effects of non-linear interactions between the parameters on EM propagation. This method has been shown to be a viable option for future studies and one that can shed light on the relative importance of various physical processes on EM propagation (Lentini and Hackett, 2015).

The current study aims to improve the fidelity of EM propagation predictions within the MASL through characterization of atmospheric refractivity and the marine surface. Comparisons of nearly co-located and synchronous measured and modeled refractivity and the impact of their differences on propagation give insight into prominent atmospheric drivers of propagation variation. The identified drivers of propagation

variations will then be applied to a point-to-point (PTP) inversion approach to estimate refractivity from *in-situ* propagation measurements where EM simulations include sea-state conditions similar to those observed during the EM measurements. Presumably, inaccuracies in the inversion are tied to the lack of, so-called, secondary drivers of propagation variations – such as turbulent and heterogenous aspects of the refractive index along with inaccurate representation of the sea surface. Thus, a turbulent refractive index model (TRIF) is investigated for its validity within the MASL via optimization of the TRIF model to *in-situ* refractivity. This optimization derives turbulent scales of the refractivity fluctuations and can be evaluated against *in-situ* measurements to gain confidence in the TRIF model. Finally, global sensitivity analysis is implemented to investigate the relative importance of mean, turbulent, and heterogenous refractive as well as sea-state characteristics on EM propagation predictions in differing atmospheric stability regimes. In totality, this dissertation puts forth results illustrating how differing components of refractivity and the sea surface contribute to the accuracy of EM propagation predictions, and how and when they should be represented within inversion methods and EM simulations to enhance propagation predictions within multiple atmospheric regimes.

Chapter 2

Background

Nomenclature	Definition
a	Radius of the Earth
ANOVA	Analysis of Variance
C_D	Drag Coefficient
C_n^2	Refractive Index Structure Constant
Cp	Specific Heat
dM/dz	M-gradient
e	Partial Vapor Pressure
ED	Evaporation Duct
EDH	Evaporation Duct Height
EDS	Evaporation Duct Strength
eFAST	Extended Fourier Amplitude Sensitivity Test
EM	Electromagnetic
g	Gravitational Acceleration
GA	Genetic Algorithms
GHz	Gigahertz
h_k	Kinematic Heat Flux
M	Modified Refractivity
MO	Monin Obukhov
mPDB	Modified Pearson Donelan Banner Spectrum

NOMENCLATURE	Definition
N	Refractivity
n	Index of Refraction
OAT	One-at-a-Time
PTP	Point-to-Point
PWE	Parabolic Wave Equation
RFC	Refractivity from Clutter
SA	Sensitivity Analysis
SST	Sea Surface Temperature
T	Temperature
T_0	Surface Temperature
$\bar{u}$	Mean Velocity
u_*	Friction Velocity
VTRPE	Variable Terrain Radio wave Parabolic Equation
X-band	Frequency band between 8-12 GHz
z	Altitude
z_0	Surface Roughness Parameter
z/L	Stability Parameter
κ	Von Karman constant
θ	Potential Temperature
ρ	Air Density
$\emptyset$	Indicates Universal Function
ψ	Indicates Integrated Universal Function

This chapter discusses background information concerning the influence of the environment on electromagnetic wave (EM) propagation within the marine atmospheric surface layer (MASL), where description of the MASL illustrates how this environment plays a unique role in EM propagation. Methods for modeling refractivity in the MASL

are also discussed where inversion and semi-empirical Monin Obukhov (MO) theory (Foken, 2006) based models are specifically highlighted.

2.1 Electromagnetic Propagation

EM wave propagation in X-band frequencies (8-12 GHz) is strongly related to the index of refraction (n) and, subsequently refractivity (N), of the medium in which the EM wave propagates (Skolnik, 2001; Sirkova, 2012). n is simply the ratio between the speed of light in a vacuum and the speed of light in the propagation medium where atmospheric refractivity is defined as:

$$N = (n - 1) \times 10^6 \tag{2.1}$$

The vertical gradients present in refractivity determine the magnitude of EM wave refraction and therefore greatly influence the propagation (Craig and Levy, 1991; Adediji and Ajewole, 2008; Cherrett, 2015). In the lower layers of the atmosphere significant negative refractive gradients can be observed, leading to anomalies in EM propagation. These anomalies are commonly referred to as trapping, or ducting, which can increase EM energy downrange of the transmitter, relative to a normal atmosphere.

Multiple types of ducts exist (i.e., surface, surface-based, and elevated), where the current research will focus on evaporation ducts (ED), an essentially permanent feature over marine environments (Gunashekar and Warrington, 2010). EDs are a type of surface duct, which induce trapping between the surface and the top of the trapping layer, termed the evaporation duct height (EDH). Due to ED prominence in marine environments, predicting and understanding this phenomenon is critical to implementing EM technologies

(Turton et al., 1988; Babin et al., 1997; Brooks, 2001). Ease of identification of EDs in vertical refractivity profiles is found through the computation of modified refractivity:

$$M = N + \left(\frac{z}{a}\right) \tag{2.2}$$

where a is the radius of the earth, z is altitude above mean sea level, and an M-gradient ($\frac{dM}{dz}$) of zero defines the EDH. EDs are commonly characterized based on the EDH, a key feature in describing ED trapping (Cherrett, 2015). The evaporation duct strength (EDS) or M-deficit, the difference between surface refractivity and refractivity at the EDH, is another descriptive ED feature (Turton et al., 1988). Refractivity, and therefore, trapping layers are a function of the environment and can be described via meteorological parameters through the empirical relationship defined by Bean and Dutton (1968):

$$M = \frac{77.6}{T}\left[p + \frac{4810e}{T}\right] + \left(\frac{z}{a}\right) \times 10^6 \tag{2.3}$$

where T is temperature in Kelvin, p is pressure in millibars, and e is partial vapor pressure also in millibars. In the MASL, evaporation ducts occur due to evaporation at the sea surface injecting water vapor into the air, a process not sustainable with increasing altitude which creates a sharp gradient in moisture near the sea surface.

In addition to refractivity of the atmosphere, reflection and scattering from the sea surface can create anomalies in EM propagation patterns. Multipath is a feature caused by interference of EM waves from two different paths – destructive interference of the waves at the receiver from multiple propagation paths results in nulls and constructive interference results in peaks. The heights of the receiver and transmitter along with the range between them and the wavelength of the radio wave determine the location of the

nulls and peaks over a smooth sea surface. Unsteady roughness at the bottom boundary (i.e., a rough sea surface) causes variations in forward scattering, specifically the direction of the scattered wave due to sea state wave phase and slightly varies the location of multipath nulls and peaks resulting in large variations in propagation in isolated locations near these nulls and peaks (Penton and Hackett, 2018).

2.2 Marine Atmospheric Surface Layer

The MASL spans the first ~10% of the planetary boundary layer above the sea-surface, where the exchange of momentum, heat, and water vapor influence distributions of atmospheric properties. Vertical fluxes in this boundary layer are considered approximately constant and turbulence is primarily influenced by atmospheric stability and wind shear, with surface roughness also playing a role (Geernaert, 2003). Most commonly, to estimate vertical distributions of atmospheric properties in the MASL, empirical functions that incorporate mean surface layer measurements are employed to provide estimates of surface layer fluxes (Businger et al., 1971; Beljaars and Holtslag, 1991; Grachev et al., 1997; Edson and Fairall, 1998; Grachev et al., 2000; Persson et al., 2002; Fairall et al., 2003). The empirical functions are derived by applying MO-similarity theory (Monin and Obukhov, 1954) and estimate the mean gradients of flow and thermodynamic properties (Garratt, 1994).

In MO theory, the wind and temperature gradients in the surface layer are functions of friction velocity, surface heat flux, height above the surface, and the buoyancy parameter (Garratt, 1994; Geernaert, 2003). The non-dimensional stability parameter ($\frac{z}{L}$) incorporates

these parameters to describe the relationship between buoyant and shear production (Chou and Kiang, 2014), where L is the MO length expressed as (Obukhov, 1971):

$$L = -\frac{u_*^3}{\kappa(\frac{g}{T_0})(\frac{h_k}{C_P\rho})} \tag{2.4}$$

where κ is the von Karman constant generally incorporated as 0.4 (Fairall et al., 1996), T_0 is the surface temperature, h_k is the heat flux, g is gravitational acceleration, C_P is the specific heat, ρ is air density, and u_*, friction velocity, can be estimated as:

$$u_*^2 = C_D\bar{u}^2 \tag{2.5}$$

where C_D is the drag coefficient and $\bar{u}$ is the mean velocity at a reference height (typically 10 m). Values of $\frac{z}{L} > 0$ indicate stable environments where shear turbulence can be suppressed by buoyancy forces and $\frac{z}{L} < 0$ indicates existence of thermal instabilities that could result in convection in addition to shear-driven turbulence; $\frac{z}{L}$ approaching zero indicates neutral conditions, where turbulence is predominately mechanical (Panofsky and Dutton, 1984). The sign of $\frac{z}{L}$ is determined by the sign of the heat flux in (2.4).

For different stability regimes, universal functions or non-dimensional gradients for momentum ($\emptyset_m$), heat ($\emptyset_h$), and moisture ($\emptyset_q$, the latter two are assumed equivalent) gradients have been defined empirically over land (Businger et al., 1971; Beljaars and Holtslag, 1991; Cheng et al., 2005) and over the ocean (Grachev et al., 2000; Grachev et al., 2007). The empirical relationships from the Kansas experiments (Businger et al., 1971) are defined via the non-dimensional stability functions within the surface layer as:

$$\emptyset_m\left(\frac{z}{L}\right) = \left(\frac{\kappa z}{u_*}\right)(du/dz) \tag{2.6}$$

$$\emptyset_h\left(\frac{z}{L}\right) = \left(\frac{\kappa z}{\theta_*}\right)(d\theta/dz) \tag{2.7}$$

where the "$*$" denotes surface layer scaling defined in Fairall et al. (2003), and k is the von Karman constant commonly set to 0.4. Specifically, (2.6) and (2.7) relate the fluxes of momentum and sensible heat to their mean gradients, respectively. The empirical universal functions were determined in the infamous Kansas experiments (Businger et al., 1971):

$$\emptyset_m\left(\frac{z}{L}\right) = \begin{cases} \left(1 - 15\left(\frac{z}{L}\right)\right)^{-\frac{1}{4}}, -2 \le \frac{z}{L} \le 0 \\ 1 + 4.7\left(\frac{z}{L}\right), \quad 0 \le \frac{z}{L} < 1 \end{cases} \tag{2.8}$$

$$\emptyset_h\left(\frac{z}{L}\right) = \begin{cases} \left(1 - 9\left(\frac{z}{L}\right)\right)^{-\frac{1}{2}}, -2 \le \frac{z}{L} \le 0 \\ 0.74 + 4.7\left(\frac{z}{L}\right), \quad 0 \le \frac{z}{L} < 1 \end{cases} \tag{2.9}$$

From (2.6) and (2.7) similarity relationships can be integrated with respect to z:

$$\bar{u} = \left(\frac{u_*}{\kappa}\right)\left[ln\left(\frac{z}{z_0}\right) + \psi_m\left(\frac{z}{L}\right)\right] \tag{2.10}$$

$$\bar{\theta}_z - T_0\left(\frac{\theta_*}{\kappa}\right)\left[ln\left(\frac{0.74z}{z_{0t}}\right) + \psi_h\left(\frac{z}{L}\right)\right] \tag{2.11}$$

$$\bar{q}_z - q_s = \left(\frac{q_*}{\kappa}\right)\left[ln\left(\frac{0.74z}{z_{0q}}\right) + \psi_h\left(\frac{z}{L}\right)\right] \tag{2.12}$$

where $\bar{u}$ is the mean wind velocity, $\bar{\theta}_z$ is the mean potential temperature, $\bar{q}_z$ is the mean specific humidity, q_s is the surface specific humidity, and SST is the skin sea surface temperature. Surface roughness is defined for momentum (z_0), temperature (z_{0t}), and humidity (z_{0q}), respectively (Frederickson et al., 1999; Fairall et al., 2003) as are the

scaling parameters denoted with the subscript asterisk. The scaling parameters and roughness scales are based on bulk meteorological measurements (Fairall et al., 1996; Fairall et al., 2003). ψ_m and ψ_h are the integrated universal stability functions ($\emptyset_h$ and $\emptyset_m$) with respect to *z* (Garratt, 1994). It is important to note that recent research has been performed to determine the empirical coefficients within the universal functions for differing stabilities and environmental settings (i.e., ice, land, rough sea), where models are appropriately appended for their specific use.

2.3 Estimating Refractivity in the MASL

Estimation of refractivity in the MASL occurs via three general methods: *in-situ* measurements, modeling techniques, and inversion methods. High resolution vertical measurements of meteorological parameters have recently become more prominent because of improved technologies enabling fine scale observations of meteorological parameters and thus, refractivity (Kang and Wang, 2016; Wang et al., 2018). These measurements are largely limited by measurement uncertainty, cost, and spatial coverage of datasets. Often, measurement uncertainties near the surface are greatest, where the largest refractivity gradients typically reside. Due to these limitations, semi-empirical surface layer models utilizing MO theory and bulk meteorological measurements are implemented to predict near surface refractivity (Fairall et al., 1996, Frederickson, 2016). Numerical weather prediction simulations blended with surface layer models are used to predict refractivity in the absence of measurements (Hodur, 1997).

Commonly, propagation simulations model the refractive environment with a single, range-independent, mean refractive vertical profile. Mean refractive profiles often reasonably predict propagation (Babin et al., 1997; Cherrett, 2015; Saeger et al., 2015), but

invoke two major assumptions: (i) negligible lateral inhomogeneities and (ii) negligible turbulent refractive index fluctuations. These assumptions have been challenged in more recent research (Strohbehn, 1968; Ulaby et al., 1981; Costa, 1991; Kravtsov, 1992; Koshel and Shishkarev, 1993; Goldhirsh and Dockery, 1997; Barrios, 2008; Chou and Kiang, 2014; Yang et al., 2015; Wagner et al., 2016) showing they can have non-negligible impacts on propagation.

Surface layer turbulence is commonly described via statistical methods and Kolmogorov spectra (Kolmogorov, 1941; Roussef, 1992; Ivanov et al., 2009; Chou and Kiang, 2014; Wagner et al., 2016). The Kolmogorov spectrum models turbulent energy from within the inertial subrange, where energy spectra in this range commonly yield a $k^{-5/3}$ (where k is wavenumber) slope (Tennekes, 1975; Ortiz-Suslow and Wang, 2019).

Use of the Kolmogorov spectrum to model refractive index fluctuations is described in detail by Ishimaru (1978), and their derivation of the turbulent refractive fluctuation spectrum culminates in (Ishimaru, 1978):

$$\emptyset(\boldsymbol{k}) = \frac{0.033C_n^2}{(L_0^{-2} + \boldsymbol{k}^2)^{\frac{11}{6}}} \tag{2.13}$$

where C_n^2 is the refractive index structure constant with units of $m^{-2/3}$, and L_0 is the outer length scale delineating the energy containing or "mixing" range from the inertial subrange, with units of meters. Average L_0 have been reported to be ~10 m in the free atmosphere (Van Zandt et al., 1978; Rouseff, 1992) where the assumption of isotropy is valid (Garrat, 1994). The assumption of isotropy breaks down within the surface layer and consequently reduction of L_0 occurs (Garrat, 1994; Chou and Kiang, 2014). L_0 have also been shown to

change with varying $\frac{z}{L}$ within the surface layer, where stable environments tend to suppress vertical outer length scales and neutral to convective environments tend to increase the magnitude of this length scale (Ludi and Magun, 2005; Emes et al., 2019).

The magnitude of turbulence in (2.13) is related to C_n^2, with ranges commonly observed on the order of 10^{-12} $m^{-2/3}$ for strong turbulence and decreasing down to 10^{-16} $m^{-2/3}$ for weak turbulence (Rouseff, 1992; Chou and Kiang, 2014, Wang et al., 2016; Qing et al., 2016). Multiple methods exist for estimating C_n^2 where methodologies employ two-point meteorological measurements (Qing et al., 2016), and bulk aerodynamic formulations (Fairall et al., 1996; Qing et al., 2016). Observed diurnal variations in C_n^2 suggest that the structure constant is dependent on stability (Ludi and Magun, 2005; Chou and Kiang, 2014). The notion of stability dependence is echoed by Frederickson et al. (1999), as they observed C_n^2 are greater in periods of thermal stability and instability, where periods of thermal neutrality corresponded to C_n^2 minima.

EM propagation through turbulent media is found in the literature, specifically, Chou and Kiang (2014) propose a comprehensive methodology for theoretical calculation and subsequent simulation of EM propagation through turbulent media. The authors compute turbulent refractive profiles for varying stability regimes and suggest that duct leakage of EM energy is enhanced by the addition of turbulence. Similar methodologies for turbulent refractivity profile realizations are found in Rouseff (1992) and Wagner et al. (2016), where the latter employs refractive turbulence when inverting synthetic PL data for refractivity.

Along with vertical fluctuations, spatial inhomogeneities in meteorological and sea surface conditions, can lead to range dependent variability in refractivity (Brooks, 2001). Goldhirsch and Dockery (1998) illustrate that as target range from EM transmission increases, neglecting inhomogeneities in refractivity can lead to propagation errors of more than 20 dB. Heterogenous refractive environments have become more prominent in the literature, where range-varying EDH is the general focus of these models (Zhao et al., 2017). Limitations in modeling range dependency of refractivity are also due to the limited research investigating how gradients below the duct can vary with range.

In addition to measurement and modeling methods for estimating refractivity, inverse methods are also considered a viable option for deriving refractivity (Rogers et al., 2000; Gerstoft et al., 2003; Rogers et al., 2005; Wagner et al., 2016; Fountoulakis and Earls, 2016; Zhang et al., 2016; Zhang and Yang, 2018; Penton and Hackett, 2018; Matsko and Hackett, 2019). Inverse problems use a set of observations that can be described by an unknown set of parameters, which are estimated through minimization of an objective function. For this EM application, measured or synthetic RF data make up the observations whereas the “unknown set of parameters” describe the refractive environment through parametric refractivity models that estimate mean refractive environments (Gerstoft et al., 2003; Karimian et al., 2011; Penton and Hackett, 2018; Matsko and Hackett, 2019). These refractivity inversions optimize refractive conditions to match the RF data set; thus, inverse methods remotely sense the refractive environment.

RF observations used in inversion methods are commonly implemented in the form of sea clutter, a technique referred to as refractivity from clutter (RFC; Rogers et al., 2000; Gerstoft et al., 2003; Rogers et al., 2005; Yardim et al., 2009; Karimian et al., 2011; Zhao

and Huang, 2012; Karimian et al., 2013; Zhao et al., 2017, Tepecik and Navruz, 2018; Compaleo et al., 2018). Although simple in the sense that the transmitter and receiver are co-located, RFC is complicated by the requirement to estimate a sea surface scattering coefficient to perform an RFC inversion, which is usually a large element of uncertainty in this approach (Plant and Irisov, 2017). More recently, inversions using point-to-point (PTP) propagation data have been studied using both measured and synthetic PTP propagation data; inversions using synthetic PTP propagation data are significantly more common in the literature (Gringas et al., 1997; Tabrikian and Krolik, 1999; Gerstoft et al., 2000; Zhao et al., 2017; Zhao, 2016; Wagner et al., 2016; Fountoulakis and Earls, 2016; Zhang et al., 2016; Zhang and Yang, 2018; Penton and Hackett, 2018; Matsko and Hackett, 2019). The limited studies using measured PTP PL data are likely because such RF measurements are more difficult to acquire than sea clutter (Pozderac et al., 2018; Wang et al., 2019). Despite the sea surface playing a smaller role in PTP propagation than clutter, the influence of the sea surface on forward scattering and propagation is also complex and has been shown to influence the accuracy of PTP inversions (Penton and Hackett, 2018).

The final component of an inversion is the optimization engine and corresponding objective function. A multitude of optimization methods exist: gradient descent, adjoint methods, particle swarm optimization, matched-field array, Markov-chain Monte Carlo approaches, support vector machines, Bayesian approaches, Kalman filters, and genetic algorithms (GA), (Gerstoft et al., 2003; Vasudevan et al., 2007; Douvenot et al., 2008; Yardim et al., 2009; Zhang and Yang, 2017; Penton and Hackett, 2018; Pozderac et al., 2018; Wang et al., 2019; Matsko and Hackett, 2019). GAs will be used as the optimization

method in this research as they have been applied successfully in previous studies (Gerstoft et al., 2003; Penton and Hackett, 2018; Matsko and Hackett, 2019).

2.4 EM Propagation Over Marine Surfaces

The sea surface plays an important role in point-to-point EM propagation as it relates to the forward scattering of EM waves propagating within the marine environment. Sea surfaces present a highly complex boundary conditions that include a multitude of scales as wind-driven processes disturb the ocean surface. Sea surface roughness effects on EM propagation are included in PWE via: (i) the computation of a roughness reduction factor augmenting propagation relative to a flat surface (Freund et al., 2006; Sirkova, 2011) or (ii) PWE solution of the EM wave over a 2-D realization of sea-surface displacement at the bottom boundary.

Direct comparison between the two approaches have been made in the literature (Benhmammouch et al., 2009; Gao et al., 2019). The roughness reduction factor approach, or Miller Brown methodology (Brown et al., 1974) incorporates sea surface effects in a statistical manner, and thus does not account all the effects of the rough surface such as the blockage of EM energy resulting in a “shadow” behind ocean wave crests. This shadowing effect can lead to large discrepancies in propagation predictions between PWE simulations that incorporate Miller-Brown as compared to a sea surface realization method when accounting for the sea surface effects (Gao et al., 2019).

Due to the combination of larger wavelength (swell/wind wave) and shorter wavelength (capillary wave) waves, forward scattering of EM energy can either be more diffuse or specular in nature. The Miller-Brown method likely does not capture the effects

of small-scale variation in propagation because of the surface phase independent calculations. Further, it has been reported that variations in propagation are restricted to null positioning when employing the Miller-Brown method suggesting the specular nature of the sea surface is primarily considered (Freund et al., 2009). Due to this drawback, in recent years, as computational power and complex PWE frameworks have become more accessible, the 2-D realization approach has been applied more frequently (Ryan, 1991; Chou and Kiang, 2014; Penton and Hackett, 2018). This approach will also be adopted in this dissertation.

Inclusion of sea-surface roughness in PWEs requires ocean wave field information down to the order of the propagating EM wave (~0.03 m for X-band); thus, down to capillary wave scales. Spectral wave models are implemented within PWE models and transformed into sea surface realizations to accurately resolve forward scattering at the rough ocean surface. An example of such a model is the modified Pierson-Donelan-Banner (mPDB) wave model (Donelan et al., 1985; Ryan, 1991; Donelan et al., 1999; Cavaleri et al., 2007) employed in the Variable Terrain Radio wave Parabolic Equation (VTRPE; Ryan, 1991) model. The mPDB models waves over a large range of wavenumbers from swell down to capillary waves covering all the relevant spatial scales needed for accurate computation of the interaction between a propagating EM wave field and sea-surface (Ryan, 1991).

2.5 Extended Fourier Amplitude Sensitivity Test (eFAST)

Propagation prediction is commonly performed via parabolic wave equation (PWE) methods, which are deterministic models, which can be explored with uncertainty analysis to identify critical input parameters and the extent of their influence on model outputs.

Specifically, sensitivity analysis (SA) can be employed to quantify model output sensitivity to input parameters and initial conditions (Marino et al., 2008; Lentini and Hackett, 2015).

A multitude of different SA techniques exist, where parameters can be explored either around a nominal value (known as local SA) or explore a wide range of parameter values including extremes and parameter interactions (known as global SA; Marino et al., 2008). The latter is more common for complex models where values of input parameters can be unknown, and a large range of values can describe a higher probability of outcomes. Global SA techniques often require large sample sizes to account for the wide range of parameter values, and Monte Carlo simulations are generally employed, where this type of SA is referred to as a sampling-based method (Marino et al., 2008).

The two designations, local and global SA, can be applied to different methods of statistical investigation quantifying relationships between input parameters and model output (Saltelli et al., 1999; Lentini and Hackett, 2015). If model output can be related to inputs via linear trends or relationships, correlation and regression coefficients can be implemented to quantify parameter influence on model output (Marino et al., 2008). More complex non-linear but monotonic relationships between inputs and model output require ranked correlation coefficients. Non-linear non-monotonic relationships between input and output parameters require methods such as variance decomposition (similar to ANOVA). Variance in the input parameters is related to variance in the model output, describing the "sensitivity" of the model to the input parameters (Marino et al., 2008; Lentini and Hackett, 2015).

The extended Fourier amplitude sensitivity test (eFAST) is a variance decomposition method that is implemented for model input/output relationships that are

non-monotonic and non-linear (Saltelli et al., 1999). Schematically, eFAST varies input parameters, each associated with incommensurate frequencies, over the entire search space, thus the sensitivity of the model output to an individual input parameter can be realized by the fraction of the total variance associated with a particular input parameter; considered the leading or first order sensitivity (Marino et al., 2008). The most common way to estimate first-order sensitivity is using a "one-at-a-time" (OAT) method in which one parameter is varied while others are fixed at a nominal value – and the process repeats for each variable. Such OAT methods do not investigate non-linear parameter interactions within complex models such as PWE simulations. eFAST techniques can investigate these interactions via the total order sensitivity by examining the fraction of total variance explained by the input parameter's complementary set. A more comprehensive description of the eFAST method can be found in §7.3**.**

Most prior sensitivity studies implement an OAT approach and vary a specific refractive parameter (e.g., EDH) and quantify the effects on propagation (Turton et al., 1988; Cherrett, 2015). Many of these studies focus on aspects of the EDH due to the primary effects ducting has on propagation predictions (Turton et al., 1988; Craig and Levy, 1991; Cherrett, 2015; Lentini and Hackett, 2015). Limitations of these OAT sampling schemes inspired the study by Lentini and Hackett (2015) that employed the eFAST method to EM propagation investigating the effects of refractive parameters and boundary conditions (sea-surface model parameters) on propagation predictions. Lentini and Hackett (2015) specifically investigate these effects for evaporative and elevated ducting scenarios at differing frequencies and transmitter signal polarizations. Conclusions are drawn regionally within the propagation domain (1000 m of altitude and 60 km of

range), where the lowest region (0-200 m) that included the MASL, reveals EDH and height of the mixed layer have the largest impacts on propagation compared to other atmospheric parameters examined in this study (Lentini and Hackett, 2015).

Chapter 3

Research Objectives

Nomenclature	Definition
C_n^2	Refractive Index Structure Parameter
CASPER	Coupled Air-Sea Processes and Electromagnetic Ducting Research
EDH	Evaporation Duct Height
eFAST	Extended Fourier Amplitude Sensitivity Test
MAPS	Marine Atmospheric Profiling System
MASL	Marine Atmospheric Surface Layer
NAVSLaM	Navy Atmospheric Vertical Surface Layer Model
NWP	Numerical Weather Prediction
PSO	Particle Swarm Optimization
RF	Radio Frequency
SA	Sensitivity Analysis

Previous research has demonstrated that discrepancies between theoretical and measured radar wave propagation occur and could be due to: i) not accounting for heterogeneous environments in which evaporation duct height (EDH) and strength vary in range, ii) inaccurate representation of the sea-surface, and iii) not accounting for refractivity fluctuations due to atmospheric turbulence (Hitney, 1990; Ivanov et al., 2009; Chou and Kiang., 2014). More recent studies have attempted to address these issues (Lentini and Hackett, 2015; Wagner et al., 2016; Zhang et al., 2017; Penton and Hackett,

2018) but did not account for all the effects discussed and their coupling effects on propagation.

The research herein aims to answer: how do primary (i.e., EDH and curvature) and secondary (i.e., turbulent fluctuations, range heterogeneity, sea-surface conditions) drivers of propagation variations affect propagation in the marine atmospheric surface layer (MASL), and to what extent do they need to be accurately characterized to sufficiently predict electromagnetic wave (EM) propagation? This question will be addressed through a series of objectives:

(i) Characterize refractivity from multiple methods including *in-situ* measurements, semi-empirical modeling, and numerical weather prediction techniques, and investigate how differences in these estimates impact propagation.

(ii) Investigate the validity of a metaheuristic inversion method inclusive of primary drivers of propagation variation (i.e., EDH and curvature) to derive atmospheric refractivity from point-to-point radio frequency (RF) propagation measurements.

(iii) Explore the applicability of a turbulent refractive index fluctuation model to simulate *in-situ* turbulent refractive index fluctuations.

(iv) Delineate the relative importance of the various secondary effects on EM propagation within the MASL for varying atmospheric stability regimes.

Objective (i) explores near-synchronous and co-located vertical refractive profiles estimated with a semi-empirical model, numerical weather prediction (NWP) simulation, and *in-situ* measurements acquired during the CASPER-East field campaign (Wang et al.,

2018). Refractive vertical profiles are characterized by EDH, M-deficit, and curvature where comparisons are made between these parameters for each method at similar times and locations. Chapter 4 discusses the results from the completion of objective (i) where variations in refractivity and subsequent propagation are primarily determined by location of EDH relative to the transmitter, changing the sensitivity of propagation predictions to EDH accuracy depending on its proximity to the transmitter. Differences in EDH between the estimation methods are greatest in stable environments. M-deficit and curvature of the refractive profiles also significantly influence propagation when EDH is greater than the transmitter height. For scenarios where the EDH is below the transmitter, EDH is the primary driver of propagation differences, where M-deficit and curvature only play a secondary role.

Objective (ii) investigates the accuracy of a metaheuristic (genetic algorithm) inversion to predict refractivity within the MASL from point-to-point X-band RF propagation measurements, where the inversion method only accounts for primary sources of propagation variation (i.e., EDH and curvature; objective (i)). The inversion method is comprehensively discussed in Chapter 5 where inversion solutions are computed and compared to the parameters estimated using the methods from objective (i). The inversion-estimated EDH has reasonable agreement with the other methods. Propagation estimated by the inversion-based refractivity are shown to be more accurate than those from the forward methods: numerical weather prediction, theory, and *in-situ* atmospheric measurements, as expected, since the inversion optimizes the refractivity based-on the RF propagation measurements. There are cases where the inversion result is not consistent with *in-situ* measured refractivity – similar to the other methods. The inversion could

potentially be improved by incorporating relevant secondary effects on propagation into the refractivity model (i.e., turbulence, spatial inhomogeneity, sea state).

Objective (iii) explores a turbulent refractive index fluctuation model that is verified against observed refractive index fluctuations. Chapter 6 introduces vertical distributions of refractivity measured within the MASL during CASPER-East and discusses results associated with objective (iii). High-resolution measurements of air temperature and humidity made with a radiosonde attached to a tethered-balloon profiling system are used to optimize a turbulent refractive index fluctuation model (TRIF). TRIF is optimized to the measurements where the vertical turbulent outer length scale is derived via particle swarm optimization (PSO) for a C_n^2 estimated from meteorological measurements and a surface layer model, NAVSLaM. This optimization gives insight into the observed variability of the refractive index, estimated from the measured temperature and humidity. Vertical turbulent length scales determined from the optimization are reasonable based-on other estimates in the literature under similar conditions in the MASL (Emes at al., 2019). However, finer-scale trends of the length scale with atmospheric stability do not match expectations and thus, estimated length scales may be considered more as an order of magnitude estimate rather than an exact measurement of this scale. These discrepancies are primarily attributed to shortcomings and assumptions associated with the estimation of C_n^2. The ability to match the observed variability in the MAPS data using a turbulence model with a reasonable choice of vertical length scale suggests the MAPS data variability is dominated by physical processes like turbulence rather than being primarily driven by measurement uncertainty. It also verifies the TRIF model against observations.

Objective (iv) quantifies the relative importance of the various secondary effects on propagation predictions, such as refractivity spatial inhomogeneity and turbulent refractive fluctuations. Propagation loss for turbulent range-dependent refractivity profiles over rough sea surfaces are investigated via a global sensitivity analysis (SA); specifically, the extended Fourier Amplitude Sensitivity Test (eFAST; Saletelli, 1999). The eFAST method enables evaluation of local and total sensitivity indices of simulated PL to refractive turbulence, range dependent refractivity, and sea state parameters for differing stability regimes (i.e., stable, neutral, and unstable). Chapter 7 discusses the results for objective (iv), where relative importance of the various secondary effects differ for scenarios where the EDH is above or below the transmitter height. For stable and neutral atmospheric stability, the main secondary effects on propagation beyond the geometric horizon are due to mean refractivity (EDH and curvature) and sea-surface conditions (wind speed). Conversely, in unstable conditions, turbulence is the leading secondary effect on propagation beyond-the-geometric horizon except very close to the sea surface. For all stability regimes, variations in low altitude (2 – 10 m) propagation beyond-the-geometric horizon are primarily driven by wind-sea surface conditions.

Chapter 4

Comparison of Atmospheric Refractivity Estimation Methods and Their Influence on Radar Propagation Predictions[1]

Nomenclature	Definition
a	Radius of the Earth
ASTD	Air-Sea Temperature Difference
CASPER	Coupled Air-Sea Processes and Electromagnetic Ducting Research
COAMPS®	Coupled Ocean Atmosphere Mesoscale Prediction System
COARE	Coupled Ocean-Atmosphere Response Experiment
e	Partial Vapor Pressure
EDH	Evaporation Duct Height
EDS	Evaporation Duct Strength
EM	Electromagnetic
ET	Local Time
M	Modified Refractivity
MABL	Marine Atmospheric Boundary Layer
MAPS	Marine Atmospheric Profiling System
MASL	Marine Atmospheric Surface Layer
MOST	Monin-Obukhov Similarity Theory
NAVGEM	Navy Global Environmental Model
NAVSLaM	Navy Vertical Surface Layer Model

[1] [1] This chapter is based on the published article listed below:
Pastore, D. M., Greenway, D. P., Stanek, M. J., Wessinger, S. E., Haack, T., Wang, Q., & Hackett, E. E. (2021). Comparison of atmospheric refractivity estimation methods and their influence on radar propagation predictions. *Radio Science*, *56*(9), 1-17.

Nomenclature	Definition
NCOM	Navy Coupled Ocean Model
p	Pressure
PCA	Principal Component Analysis
PL	Propagation Loss
PL	Propagation Loss
T	Temperature
Tx	Transmitter Height
q	Specific Humidity
q_0	Surface Humidity
RH	Relative Humidity
SST	Sea Surface Temperature
VTRPE	Variable Terrain Radio-Wave Propagation Equation
z	Altitude
δ_{MIN}	Minimum Duct Height
θ	Potential Temperature
σ_{CV}	Standard Deviation of Curvature
σ_{EDH}	Standard Deviation in Duct Height
σ_{MD}	Standard Deviation of M-Deficit
σ_{PL}	Standard Deviation in Average PL

4.1 Chapter Introduction

Generally, mean refractivity profiles are applied in propagation simulations within the marine atmospheric surface layer (MASL). This approach implies that mean refractivity must capture the main features of the refractive environment, typically characterized by parameters that are known to significantly vary propagation, such as evaporation duct height (EDH), evaporation duct curvature, and evaporation duct strength

(or M-deficit). Methods to estimate mean refractivity include *in-situ* measurements, semi-empirical surface layer models that apply boundary layer theory, and numerical weather prediction models.

In-situ meteorological measurements directly measure the (MASL) and therefore could be considered the most accurate estimate of the true environment, but they have limitations due to measurement uncertainty and limited temporal and spatial coverage. Predictions of ducting environments are therefore also carried out through theoretical/semi-empirical and numerical simulations such as Monin-Obukhov boundary layer similarity theory or numerical weather prediction. While these methods have good spatial and temporal coverage, their spatial and temporal resolution is often lacking as well as being susceptible to approximations and simplifications of the models. Due to these varying limitations and advantages, differences in refractivity estimates occur between each of these methods, which result in differences in propagation predictions. This chapter addresses objective (i) (Chapter 3) by investigating the differences in co-located and synchronous refractivity estimation methods from the CASPER-East field campaign. Estimated refractivity profiles are also used to simulate X-band frequency propagation loss patterns using a parabolic equation (PWE) propagation simulation. Observed differences in mean meteorological conditions are linked to differences in refractivity, which in turn are linked to variations in propagation predictions, to illuminate the refractivity differences that impact propagation most significantly.

4.2 Methods

4.2.1 MAPS Measurements

During the CASPER-East campaign meteorological measurements within the MABL were performed offshore Duck, NC over 25 days in 2015, 12 October through 6 November (Wang et al., 2018). The goal of the CASPER-East campaign was to perform concurrent electromagnetic (EM), oceanographic, and meteorological measurements aiding in the representation and understanding of the environment within the MABL as well as explore novel techniques for modeling EM wave propagation through the observed environments. This part of the work focuses on meteorological and sea-surface measurements made within the MASL from a small workboat and the vessel from which it was deployed, the research vessel (R/V) Sharp. Sea surface temperature (SST) observations from the R/V Sharp are sampled on 5-minute intervals consisting of bulk SST measurements corrected to skin temperature measurements (Wang et al., 2018). The meteorological measurements during CAPSER-East occurred aperiodically over 12 days during CASPER-East resulting in 36 mean estimates of modified refractivity (M) profiles of which, 27 showed evaporation ducts and are therefore used in this study. Deployed from a small workboat, MAPS was composed of a radiosonde attached to a balloon tethered to and controlled by an electronic winch allowing for measurement profiles within the MASL ranging from approximately 0.5 - 50m in altitude above the sea surface. Due to the small size of the workboat and implementation of MAPS, it is assumed that effects from the sampling platform on the environment are minimal; further detail of the MAPS system can be found in Wang et al. (2018). Each MAPS dataset includes pressure, relative humidity (RH), and temperature over approximately seven repeated ascents and descents of the

system (approximately 150-450 samples), where T is subsequently converted to potential temperature (θ) and RH is converted to specific humidity. Vertical profiles of p, θ, and q were generated by fitting a 7th order polynomial model to each respective MAPS dataset as described in detail by Wang et al., (2018). M is then computed using (Bean and Dutton, 1968):

$$M = \frac{77.6}{T}\left[p + \frac{4810e}{T}\right] + \left(\frac{z}{a}\right) \times 10^6 \tag{4.1}$$

where, e is partial water vapor pressure (millibars) that is computed using q and T to estimate the saturation vapor pressure (Buck, 1981), p is the pressure profile in hPa, z is the height above the earth's surface, and a is the radius of the earth. Note that the surface values of q and T profiles were obtained by extrapolation to the surface, which determines surface refractivity, M_0 (Wang et al., 2018).

An overview of the resulting vertical refractivity profiles used for the analysis presented in this paper is located in Table 4.1. The resulting 27 vertical evaporative duct M-profiles contain modified refractivity estimated every 0.1m from the surface up to 50m.

4.2.2 COAMPS® Forecasts

COAMPS® (Hodur, 1997) is used to produce refractive environment forecasts for this study. COAMPS® is two-way coupled with the Navy Coupled Ocean Model (NCOM) with a horizontal grid spacing of 2 km and 70 terrain following levels averaging ~32 m vertical grid spacing in the lowest 1 km of the atmosphere. COAMPS® is initialized and fed with boundary conditions from the Navy Global Environmental Model (NAVGEM) for the atmosphere (Hogan et al. 2014) and the Global Hybrid Coordinate Ocean Model (HYCOM) for the ocean (Halliwell et al., 1998). COAMPS® forecasts have been validated extensively for the CASPER-East campaign by Ulate (2019) and previously over the

eastern seaboard during the Wallops-2000 experiment (Haack, 2010). Forecasts were generated hourly using a 6-hourly update cycle throughout the duration of the CASPER-East campaign. COAMPS® forecasts are merged with an atmospheric surface layer model to increase the resolution in the lowest 100 m (Karimian et al. 2013). Specifically, the Navy Atmospheric Vertical Surface Layer Model (NAVSLaM; Fredrickson, 2016) is blended with COAMPS® forecasts near the surface in order to resolve evaporation ducts. NAVSLaM is based-off MOST, and seeded with COAMPS® forecasts of q, p, and U near the surface and NCOM forecasts of bulk SST; it simulates near-surface profiles of refractivity, temperature, winds, and humidity (Fredrickson, 2016). Forecasts used in this study consist of (hourly) vertical profiles of modified refractivity along a transect from Duck Pier (North Carolina; 36.18°N, 284.27°E) to 60km offshore with ~2km horizontal resolution. The COAMPS®-NAVSLaM blended forecasts have decimeter vertical resolution in the lowest 100m of altitude above the sea surface. COAMPS®-NAVSLaM blended refractivity forecasts are used in this study for the same locations and times as the MAPS-based refractivity data (see Table 4.1), within the limits of the horizontal spatial resolution (2km) and temporal resolution (hourly). In order to compare MAPS and COAMPS®-NAVSLaM profiles on equal footing, the blended COAMPS® T, q, and p profiles for the times and locations outlined in Table 4.1 are extrapolated from 0.5 m in altitude to the sea-surface, and modified refractivity is subsequently calculated using Equation 4.1.

4.2.3 COARE Algorithm

The Coupled Ocean Atmosphere Response Experiment algorithm - COARE (version 3.0) is a bulk parametrization algorithm used to estimate near-surface air

properties based on MOST (Fairall et al., 1996; Fairall et al., 2003; Garratt, 1994). For this study, COARE is used to estimate temperature, humidity, and wind profiles from bulk measurements collected during the CASPER-East field campaign (Wang et al., 2018). COARE requires the following parameters to estimate these profiles: sea-surface temperature (SST) and wind speed, specific humidity, and temperature at a reference height. These parameters are obtained from instruments located on two platforms: the R/V Sharp and the small workboat. Temperature and specific humidity at a height of 10 meters are extracted from the 7^{th} order polynomial fits of measurements from the MAPS dataset (Wang et al., 2018) in order to match the *in-situ* data. SST is required, and here to keep the comparisons on equal footing, we utilize the surface layer temperature (SLT; temperature at $z \sim 0$ m) from the MAPS profile extrapolation. Specific humidity at the surface is estimated assuming 98% relative humidity and using a saturation value based on the SLT (Buck, 1981). Wind speed was not measured by the MAPS system; thus, it is obtained from an anemometer located on the R/V Sharp bow mast at an altitude of 12 meters representing wind speed averaged over 30-minute intervals. Wind speed averages are all within 15 minutes of the start of the MAPS measurements. The distance between the R/V Sharp and the location of any given MAPS-based dataset is between 0.038-4.83 km with an average distance of 0.6 km; thus, the use of the mean wind speed data from the R/V Sharp seems reasonable.

Again, for the purposes of maintaining equivalency between the methods, the COARE generated humidity and temperature profiles are extrapolated to the surface from 0.5m in altitude. These profiles in conjunction with the MAPS-based 7^{th} order polynomial

pressure profiles are used to calculate modified refractivity using Equation 4.1. A COARE-based M-profile is computed for each of the 27 MAPS-based M-profiles in Table 4.1.

4.2.4 Propagation Simulations

Propagation loss (PL) corresponding to the refractivity profiles outlined in Table 4.1 are estimated using the Variable Terrain Radio-wave Parabolic Equation (VTRPE) simulation (Ryan, 1991). VTRPE simulates radar wave propagation in a variety of environmental conditions. The full-wave solution of electromagnetic fields using a split-step rotated Green's function parabolic wave equation derived from Maxwell's equations is implemented in VTRPE (Ryan, 1991). PL simulations are performed at 10.7 GHz (X-band frequency) transmitted at a height of 10.4 m with vertical polarization and a Gaussian antenna pattern containing two side-lobes. Di-electric boundary conditions are used in the model, where salinity and temperature are 35ppt and 21˚C, respectively. A smooth sea surface is employed as a bottom boundary condition to ensure differences in propagation between refractive estimation methods are primarily driven by refractivity. Refractivity profiles from Table 4.1 are simulated in VTRPE as vertical profiles that are homogenous in range. At the top of the domain is an absorption layer to prevent reflections from the upper boundary into the usable portion of the domain. The resulting output simulation grid covers 60km in range and 50m in altitude with a resolution of 2m and 1m, respectively.

4.3 Results and Discussion

This study focuses on comparing approximately co-located synchronous modified refractivity profiles estimated through multiple methods (MAPS, COARE, and COAMPS®-NAVSLaM) and examining the impact of their differences on X-band propagation. Refractive profile parameters such as M-deficit, curvature or "shape"

(analogous to the potential refractivity gradient) (Paulus, 1990; Saeger et al., 2015), and evaporation duct height are used to compare profile estimation methods due to their leading order effects on propagation (Turton et al., 1988; Whalen, 1998; Yue and Yuanliang, 2006; Lentini and Hackett, 2015). Evaporation ducts are commonly described by the M-deficit (also known as evaporation duct strength; EDS) and the evaporation duct height; both parameters affect the surface refractivity gradients (Zhang and Wu, 2011; Charette, 2015; Saeger et al., 2015). To understand the effects of the environment on variations in these estimated refractive properties, M-deficit and EDH are examined with respect to thermal stability using the air-sea temperature difference (ASTD).

Although EDH and M-deficit commonly characterize refractivity profiles in evaporative ducting environments, there is dependence of propagation on the 2nd derivative of the M-profile with altitude (Craig and Levy, 1991); thus, mean curvature ($< {d^2M}/{dz^2} >$) of the refractive profiles, where < > denotes a mean over altitude within the trapping layer, is also used for refractivity profile characterization. The results include the following key components: i) compare and discuss the propagation predictions generated by the estimated refractivity profiles, ii) characterize and compare the refractive profiles from MAPS, COAMPS®-NAVSLaM, and COARE estimation methods using the properties discussed above, and iii) relate the observed environment to variations in the refractive parameter's predictions to aid in understanding how changes in the environment affect propagation predictions based on these methods of refractivity estimation.

4.3.1 Duct Height

The largest differences in PL are driven by variations in duct heights between the methods of refractivity estimation. The time series (in local time; ET) of duct height

estimations for MAPS, COAMPS®-NAVSLaM, and COARE are illustrated in Figure 4.1; EDH exceeding the transmitter height are represented by **O** and EDH below the transmitter are presented by ×. A similar subset of the MAPS evaporation duct heights from CASPER-East can also be found in Ulate et al. (2015). It should be noted that there are scenarios where all the duct height estimates are below the transmitter height and also scenarios where the duct height estimates span the transmitter height; there are only two times in which all duct heights are above the transmitter height. The sets of evaporation duct heights are compared in terms of propagation predictions. Differences in propagation related to the differences in EDH are examined with respect to effects of the environment on EDH estimation. This analysis enables discussion of how changes in the environment are reflected in PL predictions.

The relationships between propagation loss and EDH are explored using the multivariate technique, principal component analysis (PCA; Abdi and Williams, 2010), where PL is averaged over 45-60km in range and over 2-20m in altitude, where the number of PL points included in the average (N_p) is 5.4×10^6. The PL is averaged over this area because variations in PL due to duct height frequently occur at long range and within a region encapsulating the duct height (Lentini and Hackett, 2015); 2-20m includes all duct heights in this study, which range 4-18m; statistical results for this region are unique and would not be the same for other regions within the propagation domain. PCA is a multivariate statistical technique used to reduce dimensionality of a problem by introducing new variables that are orthonormal to each other referred to as components. The components describe relationships in the variances of included variables where the first component contains the maximum variance of the orthonormal projection. By examining

what parameters contribute to the same component, linear relationships between parameters are revealed. The results of the PCA shown in Figure 4.2 demonstrate the relationships between the standard deviations in average PL between the estimation methods (σ_{PL}), standard deviations in duct height between the estimation methods (σ_{EDH}), and the minimum duct height across the estimation methods (δ_{MIN}) for times where: i) EDH estimates are all below the transmitter height (10.4m), and ii) EDH estimates span the transmitter height. Here, these standard deviation metrics are being used as a measure of the variability across the estimation methods rather than a statistical measure of the deviation from the mean across these methods; for example, a large σ_{EDH} would indicate large disagreements across the methods in the estimated duct heights. Because there are only two datasets where all duct height estimates are above the transmitter, this scenario is not independently considered in this study. Component 1 accounts for 71% and 59% of the variance in the data for times when EDH heights are below and span the transmitter, respectively. Component one loadings are only shown due to the majority of variance being associated with component one. As expected, deviations in EDH vary directly with deviations in PL (Figure 4.2). Minimum duct height varies inversely with deviations in PL and EDH. This result suggests that as the duct height decreases the methods tend to have more discrepancies between them, both in terms of EDH and PL. This result is valid for duct heights of both scenarios but the relationship between PL and EDH standard deviations is much stronger when all duct heights are below the Tx suggesting that when all EDH estimates are below the Tx, discrepancies in PL directly and strongly correlate to discrepancies in EDH estimation. The relationship between minimum duct height and duct height standard deviation is weaker when the duct heights span the Tx height. When EDH

estimates span the transmitter height, the height of the minimum EDH is shown to be significantly more related to deviations in PL than deviations in EDH. This result suggests that small differences in duct height that span the transmitter height can generate large differences in PL. Not surprisingly, this means PL predictions are more sensitive to EDH discrepancies when duct height estimates are near the transmitter height. The reduced correlation between standard deviations of duct height and PL when the EDHs span the transmitter is therefore due to both small and large discrepancies in duct height influencing PL variations. Furthermore, in these scenarios, as the minimum duct height increases, the propagation regimes are likely to be more similar, which yields the strong (inverse) correlation between minimum duct height and PL variations.

An example of these trends can be seen from the duct heights and refractive estimates on 20 October 09:41 ET (profile set 14), illustrated in Figure 4.3. This example shows duct height estimates that all occur below the transmitter, have a relatively high EDH standard deviation (2.15m), and have the lowest minimum duct height observed over the study. PL predictions for this profile set can be seen in Figure 4.4. The duct heights in these profiles are 4.2, 6.4, and 8.5m for MAPS, COAMPS®-NAVSLaM, and COARE, respectively. Figure 4.4A shows a steeper slope in PL at long range at 9m altitude as duct height decreases. The lower the duct height below the transmitter the more the propagation behaves like a normal atmosphere in the region over which the average is taken – refracting away from the surface and increasing PL at long range. Figure 4.4 demonstrates that large differences (>20dB) in PL are possible due to deviations in EDH estimates when EDH estimates are below the transmitter.

The location of the largest differences between PL predictions are observed at long ranges (~45-60km). Discrepancies in long range propagation between MAPS and the other propagation predictions for 20 October 09:41 are likely due to the relatively low MAPS EDH. Charett (2015) showed similar PL (>200 dB) from refractive profiles with EDHs less than 5m at X-band frequencies, transmitting at a height of 20m at a receiver height of 15m. These results suggest that duct height can significantly influence the differences between propagation predictions particularly if one EDH is low enough to drastically reduce leakage into the duct. Consistent with this trend, the second lowest duct height from COAMPS®-NAVSLaM is associated with higher PL at long range than COARE PL, which has the highest duct height. Presumably similar signal leakage into the duct exists for these datasets due to the more similar duct height but, the duct height closer to the transmitter (COARE) shows some evidence of trapping. This discussion supports the results shown in Figure 4.2 that PL standard deviations (or discrepancies) are influenced by both the minimum EDH across methods and variations in EDH estimates. PL differences associated with discrepancies in the shapes of the profiles are discussed in the next subsection.

Significant differences in PL also occur when EDH estimates differ such that some are above and below the transmitter height. An example of this scenario is observed in Figure 4.5 occurring on 13 October 12:49 ET. Duct heights for MAPS, COARE, and COAMPS®-NAVSLaM are 8.4m, 14.5m, and 10.4m, respectively, and Tx is at 10.4m. The propagation loss for the refractive profiles is illustrated in Figure 4.6. PL variations between methods are mainly due to the COARE EDH location being above the transmitter, while the others are at or below the transmitter. COAMPS®-NAVSLaM does not show significant trapping but shows enhanced signal carry within the duct presumably due to

EM signal leakage into the duct from the EDH's close proximity to the Tx height. MAPS PL shows much less trapping relative to the modeled data due to the EDH falling below the transmitter height resulting in propagation more similar to a normal atmosphere, including multipath null positioning. Specifically, the different duct heights cause different interactions with the lowest altitude null (above the surface) depending on whether the duct height is above or below the transmitter (Skolnik, 1990). COAMPS®-NAVSLaM and MAPS (EDHs at or below the transmitter) lowest nulls are slightly deflected downward (toward lower altitudes) (Figures 4.6B and 4.6D), whereas PL prediction for the COARE profile (Figure 4.6C) shows this null more significantly bent downward and washed out - it is no longer present at 9 m altitude (Figure 4.6A). Observations from Figures 4.5 and 4.6 exemplify the results shown in Figure 4.2, that differences in propagation loss generated from profile sets with at least one EDH estimated above the transmitter are more influenced by the minimum duct height than the standard deviation of EDH between the methods. In this case, the duct height standard deviation is relatively large (3.1 m), and the minimum duct height is relatively high (8.4 m); here, Figure 4.6, the PL comparisons are more similar to each other even though the duct height standard deviation is higher than the prior case shown (Figure 4.4) demonstrating that the high minimum duct height is more influential on the PL variations than the duct height standard deviation. When duct heights span the transmitter, one duct height may invoke very different physics than another estimate because one may be influenced more by leakage into the duct while another by trapping inside the duct regardless of how close the duct heights are to each other. Thus, a small or large standard deviation between the duct height estimates can result in large propagation

differences, which weakens the correlation between standard deviation of duct height and standard deviation of PL.

Differences in EDH estimates are often largest during times when R/V Sharp ASTD estimations suggest stable conditions, and sometimes when they suggest relatively large thermodynamic instabilities; these conditions can be seen in Figure 4.7. Increases in EDH variation at times of thermodynamic stability is expected due to the documented limitations of MOST in stable environments, which is used in the COAMPS®-NAVSLaM and COARE models. NAVSLaM surface layer predictions, which are blended with COAMPS®, have been shown to sometimes construct inaccurate meteorological profiles in stable thermodynamic regimes (Babin et al., 1997; Karimian et al., 2013). Karimian (2013) shows that during times of increased stability, duct height estimates diverge significantly for varying humidity at constant wind speeds resulting in large uncertainty during periods of stability. Similar limitations are found in the COARE algorithm, which uses empirical stability functions generated for highly unstable conditions (Fairall et al., 1996) and for stable conditions (Beljaars and Holstag, 1991). The main limitation of the MAPS profile is the use of the 7^{th} order model fit to the measured data (Wang et al., 2018), and the extrapolation of variables T and q to represent surface temperature and surface humidity (q_0). The fit profile does not capture all of the variability in the measured data, likely due to essentially time averaging the data, impacting the meteorological profiles generated. Furthermore, the 7^{th} order polynomial fit is not guaranteed to work outside the range of the data, including the surface; thus, estimates of surface refractivity from extrapolation are very different from those obtained by use of bulk or skin SST and q_0 obtained assuming 98% humidity, as is typical for water surfaces. The limitations

described above likely lead to the differences in duct height estimates (Figure 4.1) suggesting that during periods of surface layer stability, EDH and, therefore, propagation predictions may vary most significantly between the methods.

4.3.2 Profile Shape and Duct Strength

Differences in propagation loss are not only driven by duct height but by the refractivity profile shape, which is reflected in changes to M-deficit and mean curvature of the M-profile. M-deficit is the difference in the surface refractivity and the refractivity at the EDH, where changes in M-deficit can shift the location of multipath nulls in propagation, presumably through ED trapping (Turton et al. 1988; Anderson, 1995; Cherrett, 2015). Mean curvature ($< {d^2M}/{dz^2} >$) is used to represent the shape of the refractive profile from 0.5m to the EDH; this parameter has been shown to affect long range propagation in a similar manner, including shifting multipath null locations (Saeger et al., 2015; Lentini and Hackett, 2015). Time series of M-deficit and mean curvature are shown in Figure 4.8 for MAPS, COARE, and COAMPS®-NAVSLaM. M-deficits of the COARE and COAMPS®-NAVSLaM profiles vary similarly with an increase from 13 through 17 October and a decrease from 20 through 25 October (Figure 4.8A and 4.8B). Average M-deficits over the study are 6.77 and 6.73 M-units for COARE and COAMPS®-NAVSLaM, respectively. MAPS M-deficits are smaller in magnitude and show no discernable pattern over time, fluctuating between 0.4 and 6.24 M-units with an average of 2.87 M-units. Mean curvature of the refractive profiles exhibits a similar trend in time as the M-deficits (Figure 4.8B). The average mean curvature over the time series are 4.6×10^{-3} and 5.9×10^{-3} M-units/m^2 for COARE and COAMPS®-NAVSLaM, respectively. Like the M-deficits, the MAPS mean curvatures are smaller than the COARE and COAMPS®

curvatures with an average mean curvature of 8.3×10^{-4} M-units/m^2. A direct linear relationship between M-deficit and curvature is present within the MAPS (linear correlation coefficient, R=0.73, p-value <<0) and COAMPS® data (R= 0.52, p<<0) suggesting an increase in M-deficit leads to an increase in curvature of the profile. A statistically significant relationship could not be determined for the COARE data.

To understand how the shape of the refractive profiles affects PL, PCA is used to explore the relationships between variations in M-deficit, mean curvature, EDH, and PL between the methods. PL is averaged over 45-60km in range and over 2-30m ($N_p = 8.4 \times 10^6$) in altitude. Slightly different from the region averaged for duct height, this region targets the area downrange of the transmitter where multipath nulls are not present at low altitude, and altitudes that encompass the curvature of the refractive profile, which extends to approximately twice the EDH (Penton and Hackett, 2018). Similarly, to section 4.3.1, PCA is performed for scenarios where at least one EDH > Tx and where all EDH < Tx; results for each case are shown in Figure 4.9A and B, respectively. Two PCAs are performed: (i) using standard deviations of PL (σ_{PL}), EDH (σ_{EDH}), and M-deficit (σ_{MD}; blue), and (ii) using σ_{PL}, σ_{EDH}, and standard deviation of mean curvature (σ_{CV}; red). Separate PCA results for curvature and M-deficit are presented for each EDH scenario to ensure variations in refractive parameters' loading on the components are not attributed to the strong relationships between M-deficit and curvature previously demonstrated in Figure 4.8C. EDH variation, a primary driver of PL variation (section 4.3.1), is included to provide insight into the relative importance variations in M-deficit and mean curvature have on variations in PL relative to variation in EDH between the methods.

Figure 4.9A illustrates how variations in refractive parameters influence variations in PL when EDH spans the transmitter. In the M-deficit PCA (Figure 4.9A-blue), loadings of σ_{MD} and σ_{PL} are primarily on component one (52.5% of the dataset variability) indicating a direct relationship between variations in M-deficit and PL. The same relationship is observed for variations in mean curvature and PL (Figure 4.9A-red) where component one accounts for 52.2% of variability in the dataset. These similar loadings of mean curvature and M-deficit variations relative to variations in PL are expected due to the direct relationships between M-deficit and mean curvature previously described. The common PCA loadings between $\sigma_{MD,}$ $\sigma_{CV,}$ and σ_{PL} suggest that as M-deficit and curvature between the methods become more similar so do PL predictions. Variations in EDH load mainly on component two for both PCAs, accounting for ~33% of variability in each dataset. These results suggest that variations in M-deficit and mean curvature are most tightly coupled to variations in PL when EDHs span the transmitter (because they primarily load on component one), accounting for the majority of variability in the dataset. Thus, although EDH is important to propagation, when EDH spans the transmitter, the shape of the profile dominates the variations observed in PL between MAPS, COARE, and COAMPS®-NAVSLaM relative to the variations in EDH. This result is also consistent with the low loading of σ_{EDH} on component one (relative to σ_{PL}) in the previous PCA from section 4.3.1. The relationship between σ_{PL} and σ_{MD} or σ_{CV} is expected due to their connection to the M-gradient below the duct height. Both curvature and M-deficit are simplified parameters ultimately describing the M-gradient, which is a primary physical driver of propagation patterns, most notably when trapping occurs. Increases in the magnitude of the M-gradient below the duct increases the reflection angle at which EM waves are bent towards the

surface of the earth, which can increase coverage of EM signal within a duct. Thus, variations in M-deficit and mean curvature between the methods suggest differing low altitude M-gradients causing different refraction of EM waves ultimately resulting in differences in propagation between the methods.

Figure 4.9B illustrates similar PCAs to Figure 4.9A except it shows results for times where EDHs are all below the transmitter. These PCAs illustrate that variations in EDH load primarily on component one accounting for 58.6% and 52.9% of the variability for M-deficit and mean curvature PCAs, respectively. The loading of σ_{EDH} and σ_{PL} on component one indicates a direct relationship between the two parameters consistent with results in Figure 4.2. In this case, variations in EDH are primarily related to variations in PL due to EDH influence on the magnitude of signal leakage into the duct; divergence of EDH from the transmitter towards the Earth's surface restricts leakage into the duct creating PL patterns more similar to a normal atmosphere. Although σ_{EDH} loads primarily on component one, there are also differences in the loading of σ_{PL} between the two scenarios for the duct curvature PCA (Figure 4.9A vs. 4.9B, red), where σ_{PL} loads more evenly onto the two components when all the EDHs are below the duct height. This result suggests that variations in mean curvature are also significantly related to variations in PL because they both load heavily onto the same component (two). The direct relationship between σ_{MD} or σ_{CV} and σ_{PL} on component two accounts for ~33 % of variability in the data for both PCAs. This direct relationship suggests that, although increased variability in EDH is the primary cause of PL differences between the methods, an increase in variability of the profile shape can also increase variability in PL (i.e., it is a secondary effect). As previously discussed, variability in PL due to profile shape can be attributed to the

relationship between M-deficit, mean curvature, and M-gradient, where increases in M-deficit and mean curvature likely increase EM signal leakage into the duct, leading to the direct relationship on component two (Figure 4.9B). In summary, when duct heights are all below the Tx height, both the variation in EDH as well as M-deficit and/or curvature influence variations in PL with EDH variation exhibiting a stronger relationship.

It is also noteworthy that the relative influence of curvature on PL is slightly greater than that of M-deficit. σ_{PL} loads evenly on both components in both scenarios for the M-deficit PCA (blue) whereas in the curvature PCA (red) σ_{PL} loads onto component one strongly in the case where the EDHs span the transmitter height but in the other case it loads more evenly on both components. This higher loading of σ_{PL} on component one for the case where the EDHs' span the transmitter (Figure 4.9A) implies that curvature variations are more closely coupled to PL variations in these cases than are variations in M-deficit. The shift of the loading of σ_{PL} onto component two in the case where all the EDHs are below the duct height (Figure 4.9B) implies that curvature plays a larger secondary role in PL variations compared to M-deficit. Consequently, albeit slight, both cases suggest that curvature variations are more closely linked to variations in PL than variations in M-deficit.

Figure 4.10 illustrates an example profile set of refractivity estimates for MAPS, COARE, and COAMPS®-NAVSLaM where all EDHs are similar; the associated propagation predictions are illustrated in Figure 4.11. The MAPS profile in Figure 4.10 has an EDH of 8.8, an M-deficit of 2.54 M-units, and a mean curvature of 8.04×10^{-4} M-units/m^2. The COAMPS®-NAVSLaM profile has an EDH of 7.9m, an M-deficit of 6.74 M-units, and a mean curvature of 0.007 M-units/m^2. The COARE profile has an EDH of

7.8m, an M-deficit of 4.53 M-units, and a mean curvature of 0.004 M-units/m^2. As expected, MAPS propagation (Figure 4.12B) reveals less PL at long range relative to the other propagation predictions (see r ~ 50-60 km and z < 5 m). This result is likely due to increased leakage of the EM signal into duct for MAPS, which has an EDH located closest to the Tx for this profile set. Similar EDHs (~0.1m difference) are observed between COARE and COAMPS®-NAVSLaM, which are therefore expected to produce very similar PL predictions, but some discrepancies can be observed in PL between the two methods. This result is likely due to the relatively large difference in M-deficit and mean curvature between COARE and COAMPS®-NAVSLaM (COAMPS® curvature/M-deficit ~1.5 times greater than COARE curvature/M-deficit). Comparison of refractivity profiles with similar EDHs highlights the differences in PL for variations in M-deficit and curvature. The profile exhibiting a larger M-deficit should be associated with lower PL in long range due to increased duct strength. Mean curvature is also expected to introduce similar effects on propagation. This result can be seen between COARE (Figure 4.11C) and COAMPS®-NAVSLaM (Figure 4.11D) PL, where the variation in PL (~10dB) between the propagation predictions occurs beyond 40km in range and beneath ~8m in altitude. These results exemplify PCAs (Figure 4.9) previously discussed for EDH < Tx, where larger variations in propagation are observed for differences in duct heights and for similar EDHs discrepancies can be explained by differences in M-deficit and mean curvature. These results further demonstrate that evaporation duct shape influences low altitude long range propagation significantly.

The differences observed in refractive profiles that result in propagation loss discrepancies are examined to shed light on environmental factors that might cause such

discrepancies. Thermodynamic regime changes influence temperature and humidity profiles that change modified refractivity, thus observations of air-sea temperature difference and mixing ratio are included in the following discussion. Figure 4.12 shows σ_{MD} (Figure 4.12A) and σ_{CV} (Figure 4.12B) and how these statistics vary with air-sea temperature difference and mixing ratio (colorbar) at 12m based on measurements from the R/V Sharp.

Thermodynamic conditions during the CAPSER-East study range from unstable to stable where most environmental observations from the R/V Sharp reveal unstable thermodynamic conditions, and these unstable conditions typically coincided with lower mixing ratios. Variations in M-deficit are shown to be inversely related to ASTD ($R=-0.56$, $p<<0$) and mixing ratio ($R=-0.62$, $p<<0$) at 12m (Figure 4.12A), as ASTD approaches neutral conditions, variations in M-deficit between the estimation methods become smaller. This result suggests that as the surface layer (between 0-12m) becomes more neutral and humid the M-deficits between the methods become more similar. A similar inverse relationship is observed between σ_{CV} and ASTD ($R=-0.79$, $p<<0$) or mixing ratio ($R=-0.75$, $p<<0$; Figure 4.12B). The stronger relationship between σ_{CV} and the environmental variables is presumably due to the observed decreases in σ_{CV} past the neutral and into the stable regime, where σ_{MD} only decreases until a neutral regime is observed. This result suggests as environmental conditions become more humid and approach neutral conditions σ_{MD} and σ_{CV} decrease, thus profile shape between the refractive estimation methods becomes more similar.

Differences in the M-deficit and curvature are likely driven by the different surface characterization by each estimation method where variations in surface characterization

can be attributed to the estimated humidity and temperature at the surface. Despite aligning the surface conditions to be as similar as possible by extrapolating all the profiles (MAPS, COARE, and COAMPS®) from 0.5 m to the surface to determine the surface refractivity, the conditions at the surface appear to influence the overall profile shape. The MAPS profile is generated from a 7^{th} order polynomial model that does not necessarily capture the expected exponential increases in humidity at the surface. In contrast, the COARE and COAMPS®-NAVSLaM use an assumption of 98% relative humidity at the surface. The COARE used the same approximation for SST as the MAPS data but COAMPS®-NAVSLaM uses NCOM forecasted SST. Although each of these surface conditions are not explicitly included due to modifying the profiles such that they are extrapolated from 0.5 m to the surface, the influence of these surface conditions on the overall profile shape is evidenced by the different curvatures and M-deficits. In short, the stability functions implemented in MOST create much larger increases in T and q near the surface, thus M-deficits and curvature are greater than they are for MAPS data for both COARE and COAMPS®-NAVSLaM. In addition, COARE and NAVSLaM humidity profiles rely on empirical stability functions that may not be ideal for the present experiment – e.g., in some cases, they are based on measurements performed over land surfaces (Beljaars and Holstag, 1991; Fairall et al., 2003; Grachev et al., 2007; Frederickson, 2016).

4.4 Conclusions

This study explores the differences in refractivity estimates between the COARE algorithm, COAMPS® numerical weather prediction model, and MAPS measurements as they relate to propagation characterization. Variations in the predicted refractivity are linked to differences in propagation predictions to improve understanding of which

variations impact propagation most significantly. These analyses give insight into how MAPS, COARE, and COAMPS estimations of the refractive environment differ and how they impact propagation predictions. The study utilizes data from the CASPER-East experiment (Wang et al., 2018A) that includes tethered balloon measurements, shipboard measurements, NWP forecasts, and semi-empirical model estimates for approximately the same locations and times. This study parameterizes the refractive environment using the EDH and M-deficit to describe refractive profiles and associated PL as well as introducing mean curvature of the profile beneath the duct height as a factor affecting PL; analogous to the potential refractivity gradient (c_0) parameter incorporated in refractivity models (Paulus, 1990; Zhang et al., 2011; Saeger et al., 2015; Penton and Hackett, 2018; Matsko and Hackett, 2019).

Variations in duct height between COAMPS®-NAVSLaM, COARE, and MAPS cause significant variations (>10dB) between propagation predictions. For scenarios where all methods estimate EDH below the transmitter height (10.4m), discrepancies in PL predictions (σ_{PL}) are influenced by the minimum duct height across the methods (δ_{MIN}) affecting the amount of signal leaked into the duct depending on proximity to the transmitter height, and expectedly variations in duct height between the methods (σ_{EDH}). In contrast, for times where EDH estimates span the transmitter height, there is less correlation between σ_{EDH} and σ_{PL}, indicating that even small discrepancies in duct height can lead to large differences in PL. In cases where at least one EDH is above the transmitter height, the minimum duct height between the estimates is a good indicator of the magnitude of differences in PL because the further a duct height is below the transmitter height, the more likely large discrepancies will occur with another prediction based on an EDH above

the Tx. Discrepancies between duct height estimates occur primarily during periods of stability and can likely be attributed to the documented limitations of COAMPS®-NAVSLaM and COARE during these stable thermodynamic conditions (Kariman et al., 2013; Fairall et al., 1996). Results also suggest that periods of strong thermal instabilities may also result in large discrepancies between EDH estimates.

Discrepancies in PL between the measured and modeled data, specifically at long range beneath the transmitter, are also caused by differences in M-deficit and mean curvature of the refractive profiles. For scenarios where EDH span the transmitter height, variations in M-deficit and mean curvature correspond more strongly to increased variations in PL than do variations in duct height (Figure 4.9A). Conversely, it is shown for scenarios where all EDH are below the transmitter, variations in EDH are the primary driver of PL differences but variations in M-deficit and mean curvature are secondary drivers of differences in PL, which also align with results shown in Figure 4.2.

Differences in the measured and modeled M-deficits and mean curvature are likely due to differences introduced by the treatment of the surface despite efforts to make surface conditions similar by extrapolating all the data (MAPS, COARE, COAMPS®) from 0.5 m to the surface. The influence of the surface conditions in combination with MOST generates different profile shapes than that fit from the MAPS data. MOST uses empirical models for the stability functions, which may not always be representative of the environment, and the fit MAPS data also likely does not accurately capture the rapid increases in surface humidity, resulting in skewed profile shapes.

All these findings are based on the unique data set acquired during the CASPER-East experiment (Wang et al., 2018A), future studies of similar scope should examine

whether they are valid in other locations. Future research should also explore methods for accurate near surface (< 50cm) humidity measurements to enable improved estimation of surface refractivity.

Table 4.1. Summary of vertical refractivity profiles computed from the MAPS measurements, COARE algorithm, and COAMPS®-NAVSLaM numerical weather predictions. Time corresponds to the first measurement made by the MAPS system and range is the offshore distance of the workboat (MAPS) from Duck pier. COAMPS®-NAVSLaM times and locations are the closest possible time and location (within the temporal and spatial resolution of the numerical forecasts) to the start time and location of the MAPS data (4.2.2). COARE estimates are generated for each MAPS profile.

Day	Profile Set Number	Start Time (ET)	Range (km)
10/13/2015	1	12:49	4
10/14/2015	2*	9:06	28
	3*	12:42	4
	4	15:32	28
10/15/2015	5*	8:22	28
	6*	11:03	3
10/16/2015	7	9:12	28
	8	12:16	3
	9	14:38	30
10/17/2015	10	8:07	28
	11*	11:04	4
	12*	14:06	20
	13	18:25	28
10/20/2015	14*	9:41	29
	15*	12:57	4
	16*	15:29	30
10/21/2015	17*	7:01	44
	18*	8:57	28
	19*	10:29	16
	20*	12:10	3
10/23/2015	21	8:43	60
	22*	11:44	78
10/24/2015	23	8:05	60
10/25/2015	24*	11:25	28
	25	14:11	16
	26	15:58	4
	27*	18:28	28

** Denotes a profile time in which all refractive estimates possess duct heights below the transmitter height*

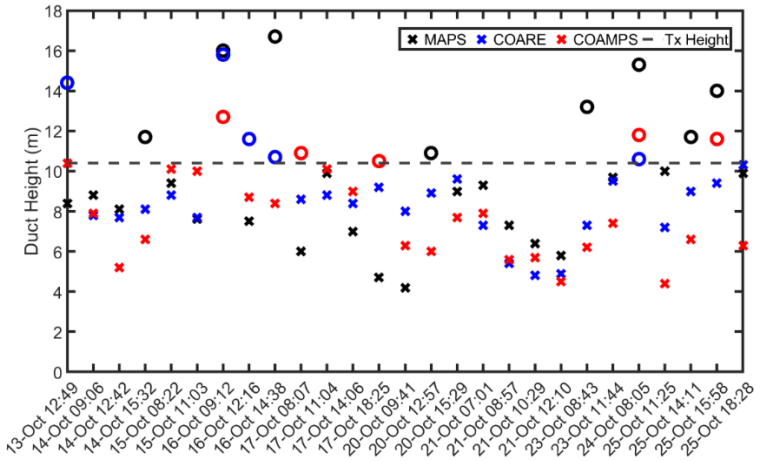

Figure 4.1. Time series of duct heights corresponding to MAPS, COARE, and COAMPS®-NAVSLaM refractivity profile estimations (see legend). Radar transmitter (Tx) height (10.4m) is illustrated by the grey dashed line and duct heights are marked by **O** and × denoting duct heights above and below the transmitter, respectively.

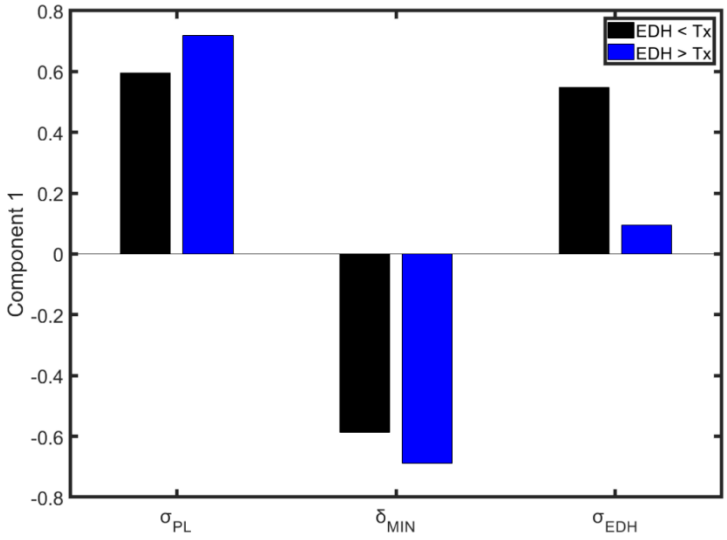

Figure 4.2. Principal component one loadings from a PCA for scenarios where all EDHs within a profile set are less than the transmitter (Tx) height (black) and where at least one EDH from within a profile set is greater than the Tx height (blue) (see legend). Component 1 accounts for 71% of the dataset variance for scenarios where all EDHs are less than the Tx height and 59% of the variance for scenarios where at least one estimate of EDH is greater than the Tx height. Variables included in the PCA are standard deviations of mean propagation loss where PL is averaged from 45-60km in range and 2-20m in altitude (σ_{PL}), minimum duct height (δ_{MIN}) across the estimation methods, and standard deviation of EDHs for the estimation methods for each profile set (σ_{EDH}).

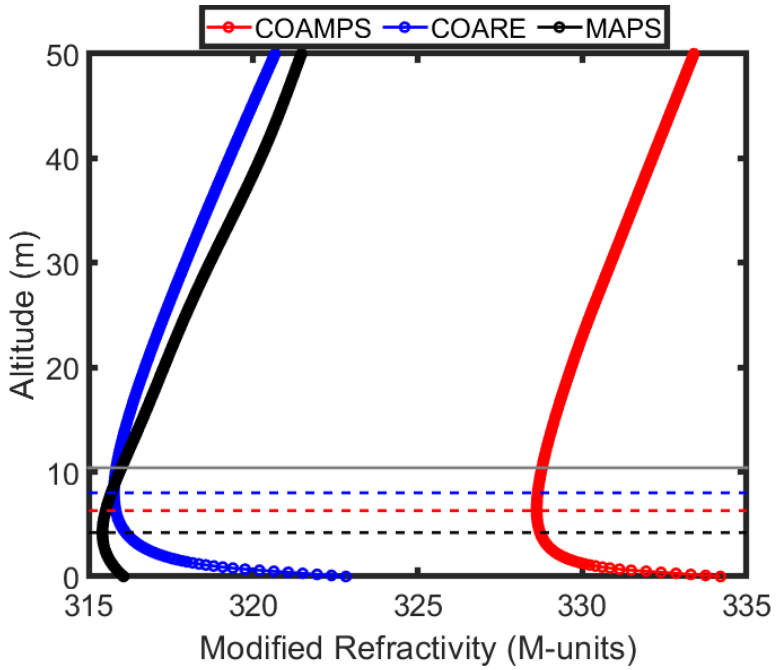

Figure 4.3. MAPS, COARE, and COAMPS®-NAVSLaM modified refractivity profiles for profile set 14, on 20 October at 09:41 local time. M-deficits in the figure are 6.4, 7.1, and 0.64 M-units for COAMPS®-NAVSLaM, COARE, and MAPS, respectively. Evaporation duct heights are denoted with the corresponding horizontal dashed lines, and the transmitter height is marked by the grey line.

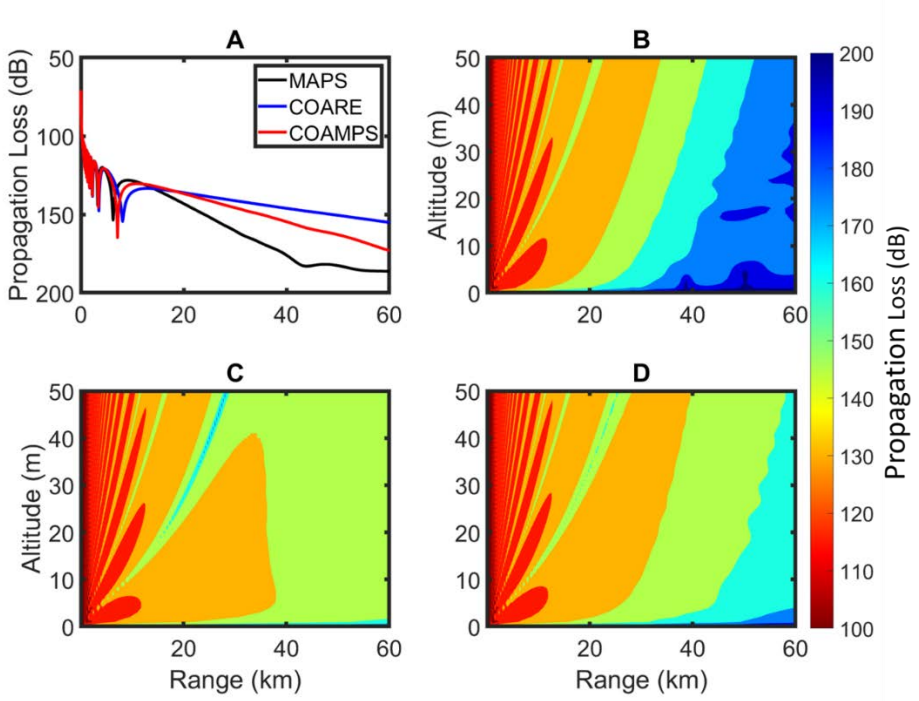

Figure 4.4. Propagation loss predictions for refractivity profile estimates shown in Figure 4.3. Propagation loss is shown in dB at a **(A)** receiver height of 9m, and for the entire prediction domain for **(B)** MAPS, **(C)** COARE, and **(D)** COAMPS®-NAVSLaM. Color bar shows PL in dB for (B), (C), and (D).

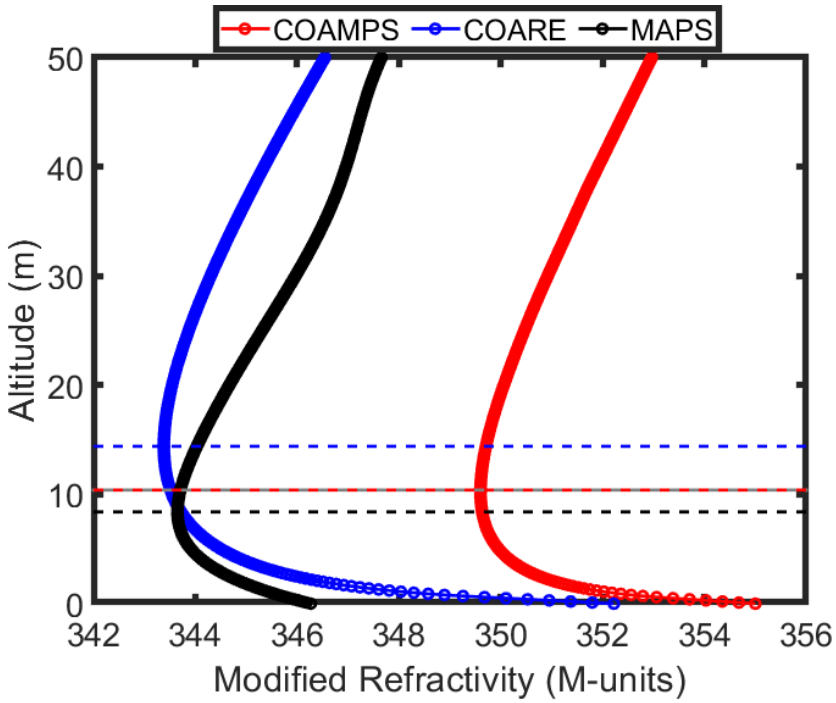

Figure 4.5. MAPS, COARE, and COAMPS®-NAVSLaM modified refractivity profiles for profile set 1, 13 October at 12:49 local time. M-deficits in the figure are 5.4, 8.84, and 2.62 M-units for COAMPS®-NAVSLaM, COARE, and MAPS, respectively. Evaporation duct heights are denoted with the corresponding horizontal dashed lines and the transmitter height is marked by the grey line.

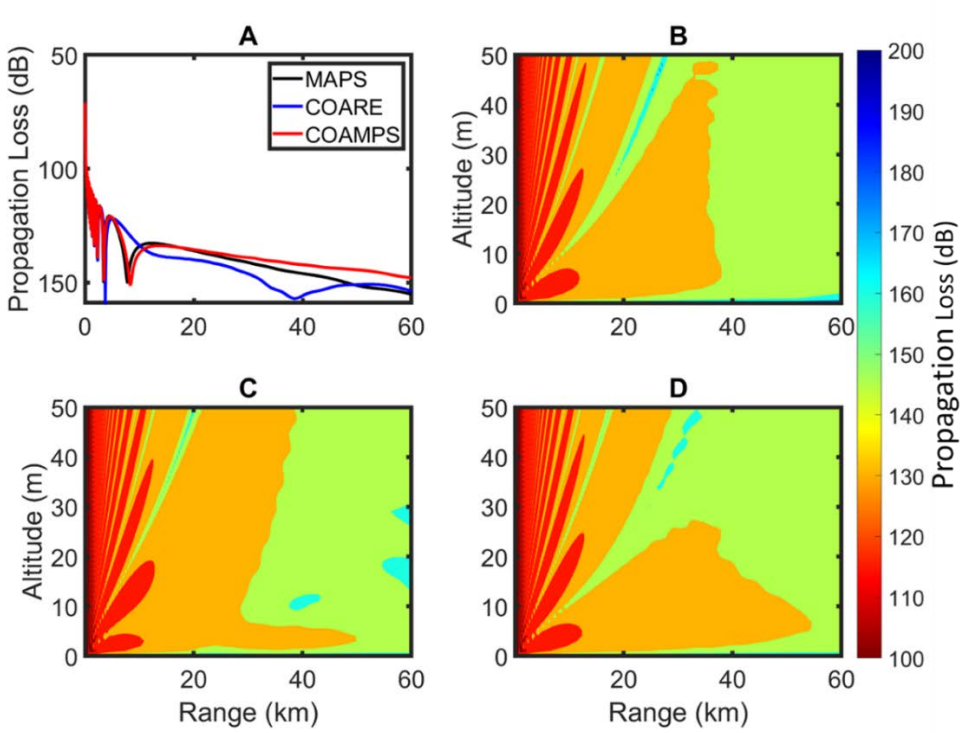

Figure 4.6. Propagation predictions from refractivity profile estimates shown in Figure 4.5, with a transmitter height of 10.4m. Propagation loss is shown in dB (color bar) for all refractive estimation methods at a **(A)** receiver height of 9m, and for the entire prediction domain for **(B)** MAPS (EDH of 8.4m), **(C)** COARE (EDH of 14.5), and **(D)** COAMPS®-NAVSLaM (EDH of 10.2). Colorbar shows propagation loss in dB for (B), (C), and (D).

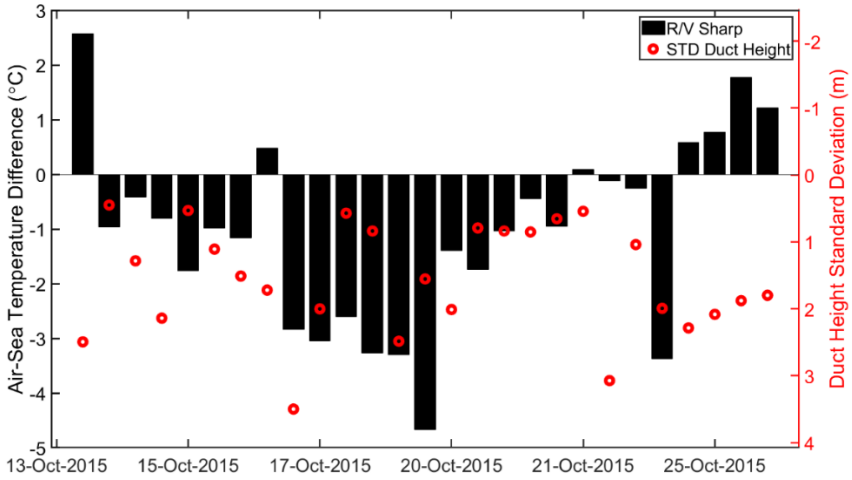

Figure 4.7. The air-sea temperature difference from the R/V Sharp (black) and standard deviation of the duct heights between MAPS, COARE, and COAMPS®-NAVSLaM for each profile set, which is indicated by the red circles and the right-hand axis.

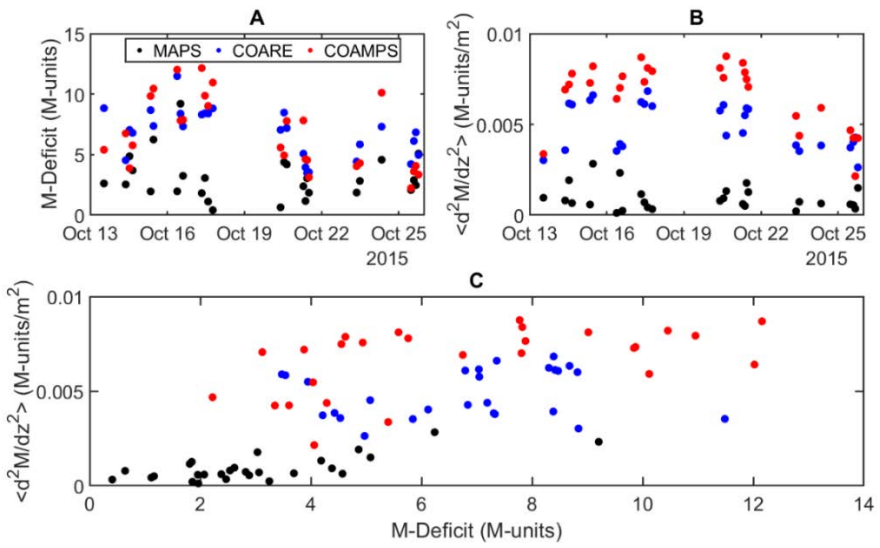

Figure 4.8. Time series of the **(A)** M-deficit and **(B)** mean curvature calculated from refractivity profile estimations generated from MAPS, COARE, and COAMPS® (see legend); **(C)** M-deficit shown in **(A)** versus mean curvature ($<d^2M/dz^2>$) shown in **(B)**. Linear relationships between M-deficit and curvature observed in **(C)** correspond to correlation coefficients of 0.75 and 0.52 for MAPS and COAMPS®-NAVSLaM, respectively.

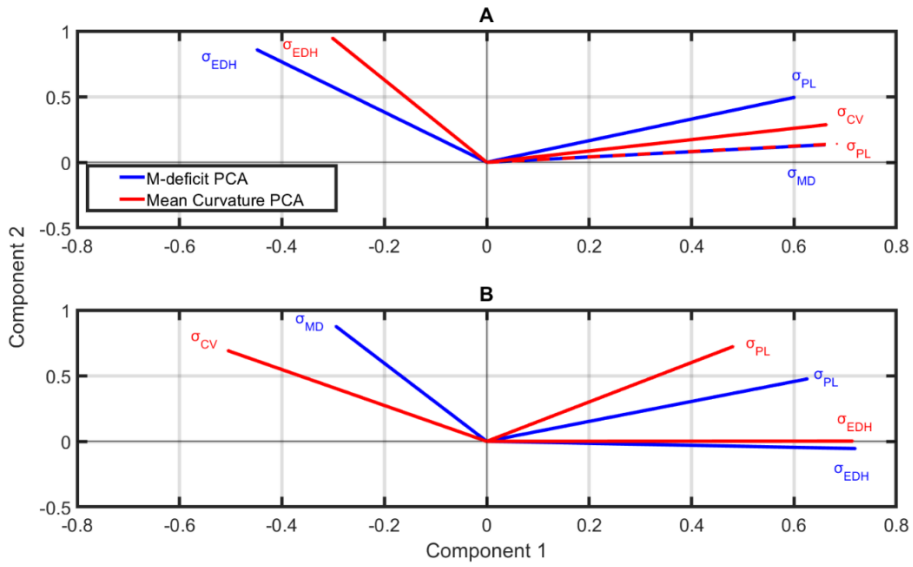

Figure 4.9. Principal component 1 and 2 loadings from a PCA on standard deviations of MAPS, COAMPS®-NAVSLaM, and COARE refractivity parameters and PL for scenarios where (A) at least one of the EDH from within a profile set is greater than the transmitter height and (B) where all EDHs within a profile set are less than the transmitter height. Component 1 in (A) accounts for 52% and 52% of the dataset variance for standard deviation of M-deficit *(σ_{MD})* and mean curvature (σ_{CV}), respectively. Component 1 in (B) accounts for 58% and 52% of the dataset variance for σ_{MD} and mean curvature σ_{CV}, respectively. Component 2 in both (A) and (B) accounts for ~33% of the dataset variance. Variables included are standard deviation of PL between MAPS, COARE, and COAMPS®-NAVSLaM (σ_{PL}), where propagation loss is averaged over 45-60km in range and 2-30m in altitude, standard deviation of evaporation duct height (σ_{EDH}), σ_{MD}, σ_{CV} for each method of refractivity estimation.

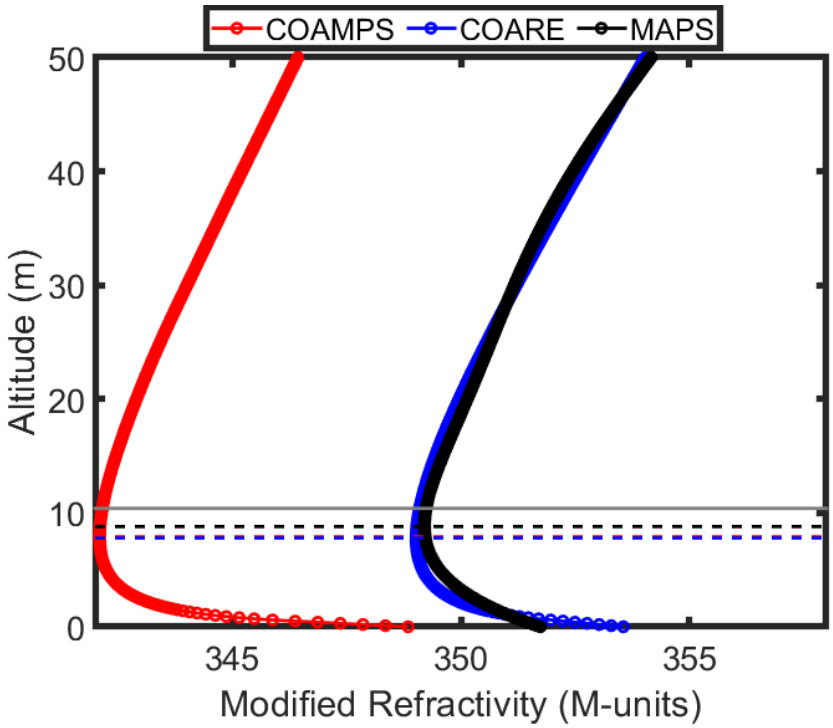

Figure 4.10. MAPS, COARE, and COAMPS®-NAVSLaM modified refractivity profiles for profile set 2, 14 October at 09:06 local time. The COAMPS®-NAVSLaM profile has an M-deficit of 6.74 M-units and a mean curvature of 0.007 M-units/m^2. The COARE profile has an M-deficit of 4.53 M-units, and a mean curvature of 0.004 M-units/m^2. The MAPS profile has an M-deficit of 2.54 M-units and a mean curvature of 8.04×10^{-4} M-units/m^2. Evaporation duct heights are denoted with the corresponding horizontal dashed lines and the transmitter height is marked by the grey line.

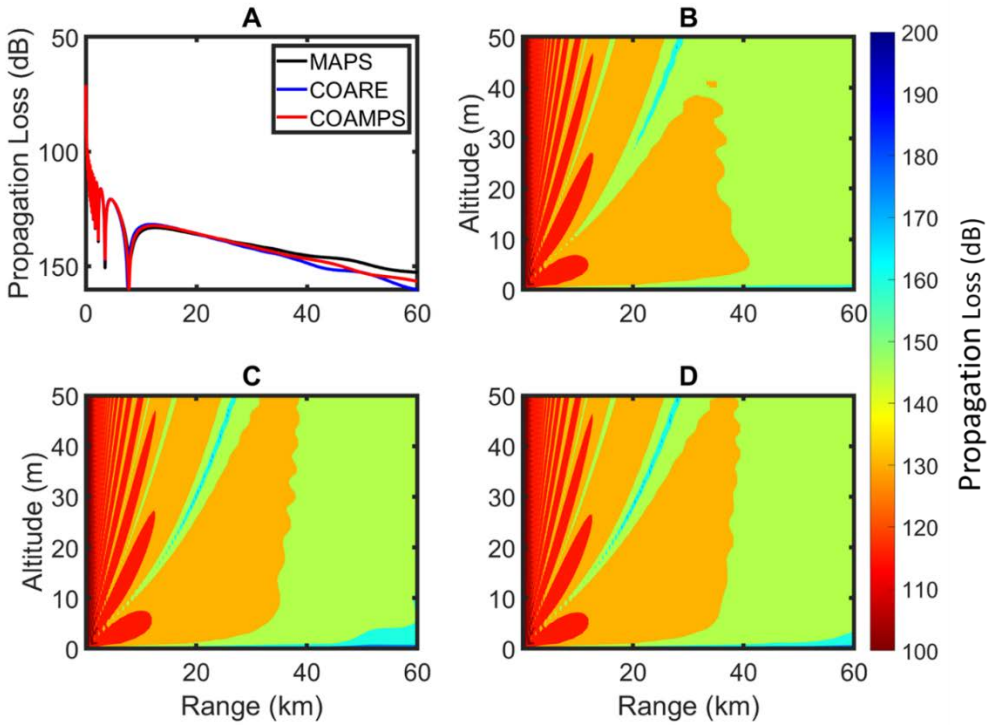

Figure 4.11. Propagation predictions from refractivity profiles shown in Figure 4.11. Propagation loss is shown for: **(A)** receiver height of 9m, and for the entire prediction domain for **(B)** MAPS, **(C)** COARE, and **(D)** COAMPS®-NAVSLaM. Colorbar denotes PL in dB for (B), (C), and (D).

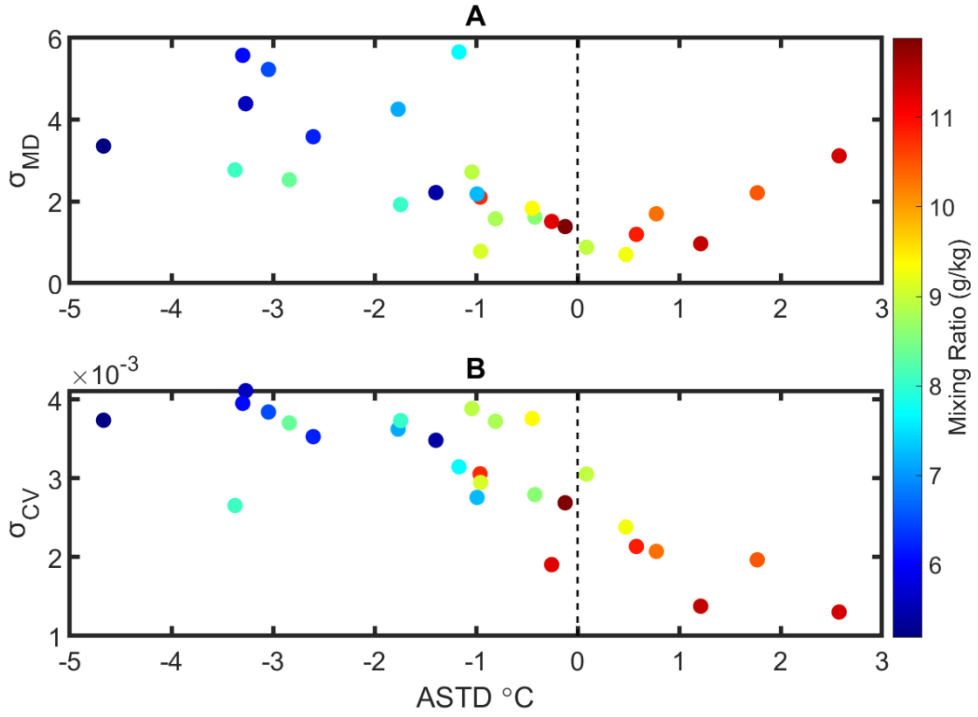

Figure 4.12. Air-sea temperature differences (ASTD) from the R/V Sharp plotted against (A) standard deviation of M-deficit (σ_{MD}) and (B) standard deviation of the mean curvature (σ_{CV}) between the profiles estimation methods. Mixing ratio at 12m represented by colors (see colorbar) and thermodynamic neutrality (ASTD =0˚) is denoted by the vertical dashed line.

Chapter 5

Refractivity Inversions from Point-To-Point X-Band Radar Propagation Measurements[2]

Nomenclature	Definition
CASPER	Coupled Air-Sea Processes and Electromagnetic Ducting Research
COAMPS®	Coupled Ocean Atmosphere Mesoscale Prediction System
COARE	Coupled Ocean-Atmosphere Response Experiment
EDH	Evaporation Duct Height
EM	Electromagnetic
GA	Genetic Algorithm
HYCOM	Hybrid Ocean Coordinate Model
M	Refractivity
M_0	Surface Refractivity
MABL	Marine Atmospheric Boundary Layer
MABL	Marine Atmospheric Boundary Layer
MAPS	Marine Atmospheric Profiling System
MASL	Marine Atmospheric Surface Layer
MOST	Monin-Obukhov Similarity Theory
MSE	Mean Squared Error
N	Number of PL Data
NAVGEM	Navy Global Environment Model

[2] This chapter is based on the published article listed below:
Pastore, D. M., Wessinger, S. E., Greenway, D. P., Stanek, M. J., Burkholder, R. J., Haack, T., & Hackett, E. E. (2022). Refractivity inversions from point-to-point X-band radar propagation measurements. *Radio Science*, *57*(2), 1-16.

Nomenclature	Definition
NAVSLaM	Navy Atmospheric Surface Layer Model
NCOM	Navy Coastal Ocean Model
p	Pressure
PL	Propagation Loss
PTP	Point-To-Point
q	Specific Humidity
R/V AE	Research Vessel Atlantic Explorer
RF	Radio Frequency
RH	Relative Humidity
SST	Sea Surface Temperature
T	Temperature
VTRPE	Variable Terrain Radio-Wave Parabolic Equation
θ	Potential temperature

5.1 Chapter Introduction

Estimation of refractive environments are typically accomplished via meteorological measurements and numerical modeling as explored in Chapter 4; however, direct measurements can be costly and impractical on a routine basis while numerical models are subject to simplifications/approximations and often have relatively coarse resolution. To overcome these limitations, inverse methods that utilize propagation models and measured propagation data to optimize a refractive environment that best matches an observed radar signal are another technique that has gained traction over the last couple decades. Considering only mean refractive parameters in the inversion problem, this chapter performs inversions to estimate mean refractivity vertical profiles and compares them with the more traditional methods discussed in Chapter 4, addressing objective (ii)

(Chapter 3). This chapter continues study using the unique CASPER-East dataset, including twelve point-to-point (PTP) electromagnetic datasets, to assess the efficacy of PTP inversion techniques for remote sensing of atmospheric refractivity within the MABL.

5.2 CASPER-East Data

The CASPER-East field campaign occurred offshore Duck, NC from 12 October – 6 November 2015 (Wang et al., 2018). The goal of the CASPER-East campaign was to perform concurrent electromagnetic (EM), oceanographic, and meteorological measurements aiding in the representation and understanding of the environment within the MABL as well as explore novel techniques for modeling EM wave propagation through the observed environments (Wang et al., 2018). This study looks to incorporate all aspects of the CASPER-East dataset to verify the remote sensing method proposed, the following paragraphs describe data incorporated from CASPER-East: (i) EM propagation measurements, (ii) wave buoy sea surface spectra, and (iii) meteorological estimates (i.e., *in-situ* measurements, semi-empirical models, and numerical weather prediction).

RF measurements during the CASPER-East campaign were comprised of both ship transmitted, and ship received (ship-to-ship) as well as shore transmitted and ship received (ship-to-shore) datasets. Due to the longer propagation path of the ship-to-shore measurements along with the fixed (non-moving) transmitter, the current study focuses on 12 ship-to-shore X-band wave propagation datasets acquired aperiodically over 9 days during CASPER-East. These datasets were sub-selected after quality control ensuring that the measurements span ranges greater than 30 km (~over the horizon) and that measurements were relatively continuous (i.e., do not exhibit frequent signal dropouts), which reduced the useable measurements to 12 datasets from an available 14 ship-to-shore

datasets collected during CASPER-East. Ship-to-shore datasets utilized vertically polarized 10.7 GHz radio frequency (RF) signals transmitted from a radio tower located on Duck pier which were received aboard the research vessel (R/V) Atlantic Explorer (AE) as the vessel transited offshore. The transmitter was located between 10.3-11.1 m above mean sea level depending on tidal phase, and receivers were located on the aft A-frame of the R/V AE at heights of 4.0m, 6.0m, 9.2m, and 12.3m (Wang et al., 2018; Wang et al., 2019). Each dataset was collected over ~1 – 3.5 hours while the R/V AE traversed 3 - 60 km offshore; datasets are illustrated in Figure 5.1 and outlined in Table 5.1. Comprehensive information on collection and post-processing of the RF data can be found in Wang et al. (2019).

Sea surface conditions during CASPER-East were measured via five moored wave buoys deployed along the research vessel excursion tracks (Figure 5.1). These mini-wave buoys sampled at a frequency of 2 Hz over ~ 40 second periods measuring sea surface wave spectra throughout CASPER-East every 30-minutes. To mitigate the fact that RF and meteorological measurements are taken over a range of offshore positions at various times throughout each day, wave spectra are averaged over each day and over all buoys to generate a single daily sea state spectrum for the study area (Figure 5.1) for each day (Table 5.1). More information about the buoys deployed and the resulting time series can be found in Wang et al. (2018). The sea surface conditions are statistically matched in the propagation simulations as described in section 5.3.

Meteorological measurements from CASPER-East are utilized for comparison of refractivity generated by the inversion. Meteorological measurements and resulting refractivity within the marine atmospheric surface layer (MASL) were obtained with the

marine atmospheric profiling system (MAPS; Alappattu et al., 2016; Rainer, 2016; Wang et al., 2018). MAPS was deployed from a small workboat, composed of a radiosonde attached to a tethered balloon raised and lowered through the MASL via electronic winch, allowing for measurement profiles spanning ~0.5 – 50 m in altitude. Effects from the deployment vessel are considered negligible due to the small size of the boat and MAPS system. MAPS datasets are collected over several repeated ascents and descents of the balloon (~150-450 samples) each including, temperature (T) – converted to potential temperature (θ), relative humidity (RH) – converted to specific humidity (q), and pressure (p). Vertical profiles of p, θ, and q are estimated by fitting a 7th order polynomial model to these measurements for each respective MAPS dataset as described in Alapattu et al., (2016), Rainer (2016), and Wang et al. (2018). M-profiles are then computed using (Bean and Dutton, 1968):

$$M = \frac{77.6}{T}\left[p + \frac{4810e}{T}\right] + \left(\frac{z}{a}\right) \times 10^6 \tag{5.1}$$

where, a is the radius of the earth, z is height above sea level, e is partial water vapor pressure (millibars) that is computed from q as well as T for estimating the saturation vapor pressure (Buck, 1981), and p is pressure in hPa. Surface refractivity (M_0) is determined by the surface values of q and T profiles after extrapolation to the sea surface (Wang et al., 2018, Pastore et al., 2021). MAPS refractivity profiles are measured within ± 12 hours of RF measurements. Variations in location and time of the MAPS data relative to the RF measurements is due to poor weather/sea state conditions and limited to daylight hours (Wang et al., 2018); MAPS profile times and locations can be seen in Figure 5.1 and Table 5.1. Further details on the deployment of MAPS and justification for the 7th order

polynomial fit can be found in Alappattu et al., (2016), Rainer (2016), Wang et al. (2018), and Pastore et al. (2021).

Modified refractivity is also estimated using the Coupled Ocean-Atmosphere Response Experiment algorithm (COARE; version 3.0); a bulk parameterization algorithm used to estimate near-surface air properties based on Monin-Obukhov similarity theory (MOST; Garratt, 1994; Fairall et al., 1996; Fairall et al., 2003). Vertical profiles of modified refractivity are computed from COARE generated meteorological profiles via equation (5.1). Meteorological and sea surface parameters required for the COARE algorithm include the following: sea surface temperature (SST), significant wave height, peak wavenumber, and wind speed, humidity, and temperature at a reference height. In this study, COARE profiles are generated using data from two measurement platforms: Duck Pier and the R/V Sharp. Data from Duck Pier used for the COARE profiles include: wind speed, T, and q, measured on 10 second intervals, and averaged over 20-minute intervals, from one of the seven fixed sensors mounted to the handrail of the pier (1.1 m above and 5.2, 4.3, 3.4, 2.4, 1.5 and 0.6 m below) (Wang et al., 2018). Sensor heights relative to the sea-surface fluctuated corresponding to tidal phase; meteorological parameters used for COARE are from the sensor nearest to 10 m above the sea-surface. Meteorological measurements from the R/V Sharp are also used to generate COARE profiles where wind speed, T, and q were measured on a bow-mast of the R/V Sharp, sampled at 1Hz and averaged over 30-minute intervals, at ~12 m above the sea-surface. Time series of the thermodynamic variables measured during the CASPER-East campaign used for COARE in this study are illustrated in Figure 5.2. SST for COARE is measured at Duck Pier and aboard the R/V Sharp consisting of the skin temperature corrected from the 5-minute bulk

SST (Wang et al., 2018). Specific humidity at the sea-surface is estimated assuming 98% relative humidity and using a saturation value based on the SST (Buck, 1981). It is important to note, the R/V AE (RF receivers) and R/V Sharp are located 0 – 58km apart during the RF measurements as ship tracks converge or diverge over the course of the day (Wang et al., 2018). Significant wave height and peak wavenumber parameters for COARE were retrieved from the daily averaged wave buoy spectra from the associated day.

To complement the *in-situ* (MAPS) and semi-empirical (COARE) estimations of refractivity, this study utilizes a numerical weather prediction model, specifically, the Coupled Ocean Atmosphere Mesoscale Prediction System (COAMPS®; Hodur, 1997). COAMPS® is initialized with boundary conditions from the Navy Global Environment Models (NAVGEM) for the atmosphere (Hogan et al., 2014) and the Global Hybrid Ocean Coordinate Model (HYCOM) for ocean conditions (Halliwell et al., 1998). Meteorological forecasts were generated hourly from a 6-hour initialization cycle throughout the duration of CASPER-East (Ulate et al., 2019; Pastore et al., 2021). In the lowest kilometer of the atmosphere, the average vertical resolution of the model is ~32 m with 70 terrain following levels; this resolution is unsatisfactory for resolving evaporation ducts thus, COAMPS® is blended with the Navy Atmospheric Surface Layer Model (NAVSLaM; Frederickson, 2016) increasing resolution to a decimeter in the lowest 100 m enabling evaporation ducts to be resolved (Pastore et al., 2021). NAVSLaM is based-off MOST, and seeded with COAMPS® forecasts of q, p, and U near the surface and the Navy Coastal Ocean Model (NCOM) forecasts of bulk SST (Frederickson, 2016). COAMPS®-NAVSLaM derived vertical refractivity profiles have hourly temporal resolution every ~2 km along a transect

from Duck Pier (North Carolina; 36.18°N, 284.27°E) to 60km offshore (Pastore et al., 2021).

5.3 Forward Propagation Modeling

Propagation predictions are generated by the Variable Terrain Radio-Wave Parabolic Equation (VTRPE) simulation; VTRPE simulates radio wave propagation in a variety of environmental conditions (Ryan, 1991). The full-wave solution of the EM field is computed via a split step rotated Green's function parabolic equation (Ryan, 1991; Sirkova, 2012; Saeger et al., 2015; Penton and Hackett, 2018; Matkso and Hackett, 2019; Pastore et al., 2021). PL data are simulated matching the antenna characteristics of the measured RF data (Table 5.1), including the Gaussian antenna pattern with two side lobes emulating the horn antennae. The simulation domain is 60km in range and 50m in altitude with an output grid resolution of 2 m and 1m, respectively.

Dielectric boundary conditions are prescribed in the simulation using the skin SST (Wang et al., 2018A) measured aboard the R/V AE and assumes a salinity of 35 ppt. Rough surface bottom boundary conditions for PL simulations are generated within VTRPE as sea surface realizations. Sea surface elevations profiles are extracted from a two-dimensional surface generated from an inverse transform of the convolution of a two-dimensional zero-mean Gaussian process and a two-dimensional ocean wavenumber spectrum (Penton and Hackett, 2018). The ocean wavenumber spectrum is produced from a modified Donelan-Pierson-Banner wave spectral model (Pierson and Moskowitz, 1964; Donelan et al., 1985; Banner et al., 1989) for the wind seas, and is appended with a Gaussian narrow-band swell spectrum. The daily average wave spectrum obtained from the buoy measurements (§5.2) is matched to the wave model spectrum via adjustment of

the wave model parameters in VTRPE to generate a statistically similar sea surface. Specifically, significant wave height was matched within 15%, where significant wave height was estimated as $H_s = 4\sqrt{m_0}$, where m_0 is the zeroth-order moment of the 1D wave spectrum. The peak wavelength of the average buoy and VTRPE sea state spectra were also matched via adjustment of the VTRPE wave model parameters. An example illustrating a comparison of the spectrum from the VTRPE wave model, and the averaged buoy wave spectrum is illustrated in Figure 5.3.

Forward modeled propagation is included in this study to evaluate the efficacy of the proposed inversion method. The following paragraphs describe CASPER-East refractivity datasets available for forward propagation modeling as well as several possible options for each refractivity estimation method (COAMPS®, COARE, and MAPS) that can be used to describe RF measurement environments (i.e., due to the temporal and spatial variability of the meteorological and RF measurements multiple options exist). No option discussed below can be considered the "true" environment due to the temporal and spatial discrepancies between the refractivity estimates and RF measurements thus, propagation comparisons based-on refractivity for the forward modeled refractivity estimation methods are performed to determine the option that best matches each RF measurement dataset. Discussion of the MSE used to determine the "best" forward model option with respect to the RF measurements (Table 5.1) is described at the end of this subsection.

Several possible options exist for comparisons of refractivity estimated by MAPS to that estimated by the inversion. The RF data was collected over several hours while the ship traversed ~60 km in range; MAPS data is collected at discrete ranges at discrete times. In other words, there exist multiple ways in which the MAPS data could be used to generate

a propagation prediction for a (single) corresponding RF dataset. In order to select the most accurate MAPS-based representation of the environment for each RF dataset, several options were compared and the option/refractivity estimate that produced the best match to the measured RF data is used for comparisons. The following options were evaluated for forward modeling associated with each inversion/RF dataset: MP1) the (range independent) profile closest in time (during if possible) – regardless of the range at which it was acquired, MP2) a (range independent) mean profile averaging all profiles measured within a ± ~12 hour window surrounding the RF measurements (which span several ranges), MP3) a (range-independent) refractivity profile closest to the mid-range of the RF collection track – regardless of time (within the ± 12 hour window), and MP4) a range-dependent profile set that consists of single profiles within the ±12 hour window at their associated ranges.

Similar spatiotemporal matching issues occur for COARE estimates of refractivity. In this case, multiple COARE estimates can be associated with a single RF dataset because the COARE data is from the R/V Sharp or Duck Pier, which collected thermodynamic data at ~30 min intervals, so the temporal resolution is better than MAPS, but the R/V Sharp samples are taken at various discrete ranges over the RF data collection time period. For COARE, the following options were considered: CR1) a (range independent) mean refractive profile inclusive of both Duck Pier and R/V Sharp based refractivity profiles over the duration of the RF measurements (that occur at various ranges), CR2) the (range independent) refractivity profile closest to the mid-range of the RF collection track – regardless of time (within a ± 6 hour window), CR3) the (range independent) mid-time profile relative to the RF measurements – regardless of the range at which it was acquired,

and CR4) a range dependent profile set comprised of a pier-based refractive profile closest in time to the RF measurements and R/V Sharp-based profiles in range that occur during the RF measurement data collection time period.

Similar to the other environmental sources, radar measurements span multiple COAMPS®/NAVSLaM forecast periods (see Figure 5.1) so several options were examined for forward modeling of the propagation: CP1) a range-dependent refractivity profile set from the time average of all forecasts during the RF measurements, CP2) range-dependent refractivity profile set estimated from the forecast closest to the mid-time of the RF measurements, CP3) range-independent refractivity estimated from the time and range average of all forecasts during RF measurements, and CP4) range-independent refractivity estimated from the range average of the forecast closest to the mid-time of the RF measurements.

PL is simulated for each refractivity source (and associated configurations) delineated above and comparisons are made between measured and simulated PL; receiver heights for the latter correspond to RF receiver height rounded to the nearest meter. The comparison is computed as a mean square error (MSE) summed over all the receiver heights (and ranges). MSE over all receiver heights and ranges is used to provide an overall evaluation of the match to the RF propagation data (rather than at one specific height or range). Before computing the MSE, both the simulated and measured RF data are smoothed with a running average filter of length equal to the peak wavelength of the sea surface. This technique minimizes the influence of slight differences in the multipath null/peak locations on the MSE statistic due to the sea surface (Penton and Hackett, 2018). For each environmental source, the option (e.g., CP1, CP2, or CP3) that produced the smallest MSE

is used for comparison to the inversion results (Table 5.1). It is assumed that the environmental configuration/option that produced the lowest MSE relative to the RF measurements is the optimal representation of the environment for each respective forward modeling method. The inclusion of range dependent refractivity forward modeling options potentially allows for more accurate propagation predictions in cases where the influence of horizontal inhomogeneity on the propagation may be significant, which is an aspect that the inversion process cannot account for, and therefore, this approach also enables an evaluation of how that assumption might impact the accuracy of inversion results. Times and locations of measurements associated with the optimal options are shown in Figure 5.1 and described in Table 5.1 (including the MSEs).

5.4 PTP Inversion Modeling

An overview of the inversion algorithm is outlined in Figure 5.4. Genetic algorithms are used to generate refractivity parameter sets that construct a refractivity vertical profile using a parametric refractivity model that is homogenous in range. Propagation loss is then simulated for the refractive profile using transmitter and sea state conditions that match those associated with the RF data, as described in §5.3 for the forward modeling. Simulated propagation loss is subsequently compared to the RF data via a fitness (or objective) function. This process is iterated until an optimal solution is reached by achieving a specified threshold for the objective function or a specific number of iterations have been completed. More information about the genetic algorithms, parametric refractivity model, and the fitness function are described in the subsequent paragraphs.

Genetic algorithms (GA), the chosen optimization method in this research, have been effective in deriving refractivity from sea surface clutter (Rogers et al., 2000, Gerstoft et al., 2003, Roger et al., 2005) and synthetic PTP propagation data (Wagner et al., 2016; Fountoulakis and Earls, 2016; Zhang et al., 2016; Zhang and Yang, 2018; Penton and Hackett, 2018; Matsko and Hackett, 2019). In addition to GAs, prior inversion studies have also used other optimization methods such as adjoint models (Zhao et al., 2017), Markov chain marching algorithms (Anderson et al., 2001), maximum likelihood estimation (Wagner et al., 2016), particle swarm optimization (Zhang and Yang, 2018), iterative local search (Wang et al., 2019), and simulated annealing (Xiao-Feng et al., 2011) all of which could be feasible for this application as well. Nevertheless, GAs optimize a set of parameters through Darwin's theory of natural evolution, where individuals in a population influence future individuals through natural selection and genetic mutation (Goldberg, 1989; Johnson and Rahmatt-Samii, 1997; Penton and Hackett, 2018). In this study we apply a GA to optimize parameters of a refractivity model that best represent the atmospheric conditions in which the RF data were collected. The parametric model is a piecewise modified refractivity model consisting of two layers – an evaporation layer and a mixed layer (Gerstoft, 2003; Saeger et al., 2015; Penton and Hackett, 2018; Matsko and Hackett, 2019):

$$M(z) = M_0 + \begin{cases} c_0\left(z - z_d \ln\left(\frac{z + 0.00015}{0.00015}\right)\right) & , z \le z_L \\ m_1 z - M_1 & , z > z_L \end{cases} \tag{5.2}$$

where M is modified refractivity, the surface refractivity is $M_0 = 333$ M-units, z_d is evaporation duct height (EDH), m_1 is mixed layer slope, and M_1 is a term defined by other parameters (c_0, z_d, and m_1) ensuring a continuous profile between layers. The potential

refractivity gradient (Paulus, 1990), c_0, allows adjustment of evaporation layer "curvature" for a given duct height (Saeger et al., 2015). The evaporation layer extends from the surface to $z_L \equiv 2z_d$. A fixed value is used for M_0 because it is the gradient of the M-profile that affects propagation, not the specific values (Wang et al., 2018A).

Refractivity parameters are randomly assigned to the 25-member initial population, which has a restricted search space of 0.03 < c_0 < 0.47 M-units/m, 0.03 < m_1 < 0.18 M-units/m, and 1 < z_d < 20 m. The search space of c_0 is relatively large compared to the value for a neutral atmosphere (0.125 M-units/m; Paulus, 1989), which is necessary to ensure c_0 is properly explored by the GA due to the unknown distribution of c_0 for non-neutral atmospheres. The range selected for m_1, similar to c_0, is selected to cover a wide range of mixed layer slopes due to the unknown distribution of m_1 for differing environments but is inclusive of the global average value of 0.118 M-units/m (Gossard and Strauch, 1983; Penton and Hackett, 2018). The range of z_d is determined from MAPS, COARE, and COAMPS® EDH estimates during CASPER-East. Ulate et al. (2019) and Pastore et al. (2021) show that during CASPER-East duct heights from the three methods generally occur below 20m in altitude.

Populates, comprised of refractivity model parameters (i.e., c_0, z_d, and m_1), generate refractivity profiles that are then used to generate PL predictions, which are directly compared to the measured RF data, generating a fitness score for each populate:

$$\Phi_{MSE} = \frac{1}{N}\sum_{i=1}^{N}\left(\zeta_i^M - \zeta_i^S\right)^2 \tag{5.3}$$

where ζ^M is the measured PL in dB, ζ^S is simulated PL in dB corresponding to modified refractivity generated by the GA, and *N* represents the number of PL data – all the points

in range for all four receiver heights. ζ^S and ζ^M are averaged over the peak wavelength as previously described in the forward modeling section prior to computing Φ_{MSE}. Measured RF data are not always continuous in range due to post-processing procedures and signal dropouts, thus only points of co-located PL between measured and simulated data at all receiver heights are included for *N*. RF receiver heights are compared to the nearest simulation altitude (e.g., ζ^M at z = 9.3m is compared to ζ^S at z = 9.0m).

Once each populate is evaluated, a new generation is produced where cross-over between and mutation of populates occurs creating the new population that can scrutinize the entire parameter search space with varying individuals. Individuals with the two best fitness scores are passed down to the next generation, this process is known as elitism. The algorithm continues to optimize the populations until one of the following is achieved: (i) 60 generations have been realized, (ii) an ideal fitness score is achieved ($\Phi_{MSE} \leq 0.2$ dB^2), or (iii) over 25 generations, the average relative change in fitness scores is below 0.002 dB^2. All inversions in this study were terminated via criterion (iii) except for inversion E (Table 5.1), which terminated satisfying criterion (i). More information on the GA configuration can be found in Penton and Hackett (2018) and Matsko and Hackett (2019).

5.5 Results and Discussion

Figures 5.5-5.8 show forward modeled PL (for the option with the lowest MSE), RF measurements, and the inversion-based PL for each receiver height, respectively. As expected, given that this is the basis for the optimization, overall, the inversion method produces the most accurate match to the propagation. In most cases, null position and PL at ranges beyond the multipath nulls are more similar to the measured data for the inversion solution than the forward model predictions, including those that describe the environment

with range-dependent refractivity. Furthermore, the inversion is significantly more successful at predicting propagation relative to the forward models as is statistically evident by comparison of the average MSEs (Φ_{MSE}): 9.94 dB^2, 54.05 dB^2, 76.15 dB^2, and 45.36 dB^2 for the inversion, COARE, COAMPS®, and MAPS, respectively. Although the lower average Φ_{MSE} for inversion PL confirms more accurate PL predictions, the better propagation predictions do not necessarily imply improved environmental predictions. The inversion approach may converge on an environment that only predicts the propagation accurately at the receiver heights and not necessarily everywhere – in other words, there can be non-unique solutions with a limited RF data set (Matsko and Hackett, 2019; Wang et al., 2019).

To evaluate the inversion-based environment, refractivity for the forward models that resulted in lowest PL MSE are compared to the (refractivity) inverse solutions in Figure 5.9, where it should be noted that forward model cases with range dependent refractivity are averaged over range to improve legibility of the figure (e.g., COAMPS® refractivity profile in Figure 5.9A). The most striking differences occur with respect to the mixed layer slope (e.g., Figure 5.9A, I or L); however, it has been shown that differences in the mixed layer slope don't affect propagation as significantly as other refractive parameters in the near surface (Lentini and Hackett, 2015; Penton and Hackett, 2018; Matsko and Hackett, 2019; Pastore et al., 2021) – resulting in a relative insensitivity of the GA optimization to this parameter. Much more important is the duct height and the shape below the duct height (Cherrett, 2015; Pastore et al., 2021). In many cases, EDHs from the inversions are similar to other estimates (see Table 5.1). Disagreements in EDH could be caused by temporal and spatial evolution of the environment during RF measurements

(collected over ~ 1.5 – 3 hours and over ~50km) as also mentioned in Wang et al. (2019). Consequently, none of the predictions are likely to represent the "true" environment that the EM waves traversed; thus, discrepancies between the refractivity estimates are expected.

To scrutinize the comparisons of EDH specifically, Figure 5.10A shows EDH comparisons between the forward methods determined to be the "best" estimate of the environment (determined by the lowest propagation loss MSE for each refractive estimation method) for each RF dataset and EDH derived from the inverse solutions; note that EDH for range-dependent refractivity is represented by an average EDH over range. Figure 5.10B shows average stability over the radar data acquisition time, $\varphi = {}^{z}/_{L}$, where $z = 12$ m and L is the Monin-Obukhov length based on R/V Sharp measurements. For bulk meteorological measurements, L is defined in Fairall et al. (1996):

$$L^{-1} = \frac{\frac{\kappa g}{T}(T_* + 0.61 T q_*)}{u_*^2} \tag{5.4}$$

where T_*, q_*, and u_* are scaled temperature, humidity, and wind speed respectively (Fairall et al., 1996). When $\varphi < -2$ (denoted by the horizontal black dashed line in Figure 5.10B), which is indicative of highly unstable environments, EDH across all methods is in relatively good agreement, and all PL estimates show good agreement with RF measurements at long range. This result is shown in Figure 5.10B, where the bars show ΔPL, which is average propagation loss difference between each respective method and the measured RF over all receiver heights at ranges greater than 30 km. Ranges greater than 30 km are used for comparison because this region is most influenced by trapping of EM waves; furthermore, this region is mostly devoid of multipath peaks/nulls that can have large impacts on the MSE statistic. Thus, this region is expected to most accurately capture

variations in propagation due to differences in the ducting phenomenon. Under such unstable environmental conditions, the inversion solution predicts the environment as well as the other methods. COARE and COAMPS®/NAVSLaM are also known to perform best during unstable conditions (Fairall et al., 1996; Frederickson, 2016). Conversely, when $-2 < \varphi < 0.05$, EDH varies more substantially between the methods. Corresponding variations in Φ_{MSE} are at least partly due to these variations in EDH, which are known to have significant effects on PL (Hitney and Vieth, 1990; Cherrett, 2015; Pastore et al., 2021). Neutral/stable regimes generally correspond to higher duct heights from the inversion solution, which is consistent with previous studies showing EDH increases in stable environments (Cherrett, 2015, Zhang et al., 2017). Higher EDH during near neutral or stable conditions predicted by the inversion coupled with the more similar propagation (Figure 5.10B) suggests that the deviation of the inversion solutions from the other methods does not necessarily indicate that it is an inaccurate representation of the environment. The possibility exists that the spatiotemporal variability during RF data collection creates non-ideal environmental estimates from the other methods presumably causing the discrepancies relative to the measured RF at the same times. Collectively, these results suggest that the inversion method employed in this study is a viable technique for obtaining estimates of atmospheric refractivity in all included stability regimes.

5.6 Summary and Conclusion

This study utilizes a unique dataset to verify a PTP radar inversion approach that utilizes a metaheuristic algorithm and inverts for three parameters associated with evaporation ducts. Twelve RF measurement sets from the CASPER-East campaign are compared to PL generated from several different forward models of refractivity and the

inverse model. Due to finite time periods over which the propagation measurements are acquired, multiple options for environmental characterization exist for these forward methods. Several options were examined and the forward method that generated PL closest to that of the RF measurements were used for comparisons of both refractivity and PL from inverse solutions. All methods, inverse and forward, were in relative agreement during periods of large instability ($\varphi < -2$) in terms of propagation and EDH. However, when conditions were stable or near neutral more discrepancies between the methods were observed. In these cases, the inversion often predicted a higher EDH than other methods and also showed more accurate PL relative to the RF measurements suggesting that this inverse-based environment might be a better representation of the environment than other estimates because high EDH is consistent with stable regimes. In general, inversion solutions provide reasonable predictions of the environment under a range of conditions relative to the other methods examined and resulted in more accurate PL predictions at the locations of the receivers. Future research should involve inverting for range inhomogeneous refractive features to investigate the effect spatial variability of the environment can have on refractivity inversions.

Table 5.1. Time and transmitter height of RF measurements, forward modeling option (e.g., CR1, MP1, CP1) that generated the lowest MSE for each method (COARE, MAPS, COAMPS®) along with times and locations associated with those options (§5.3), the MSE between each method and the RF measurements, and duct height for each method. Note in some cases there was no MAPS measurement within a ± 12 hour window of the RF measurements so that data type is not used for comparison in those cases.

* Denotes a mean

Experiment	Radar Time (EST)	Tx Height (m)	Forward Modeling Option	Profile Time (EST)	Profile Distance From Pier (km)	MSE (dB^2) All Rx	Duct Height (m)
A	10/13/2015 20:57-23:20	10.5	CR1	21:00 - 23:12	0,27,33,38,44,50	27.7	8.1*
			MP1	15:47	30	48.58	44.7
			CP1	20:00-23:00	0-60	33.14	8.1*
			Inversion	-	-	7.14	9.15
B	10/14/2015 20:01-21:53	10.3	CR4	14:42-21:42	0,44,50	34.62	13.9
			MP4	09:06 - 15:32	4, 28	26.3	8.4*
			CP4	21:00	0-60	29.37	9.4
			Inversion	-	-	25.18	12.93
C	10/15/2015 13:48-15:09	10.9	CR2	14:42	30	14.38	7.9
			MP2	08:22-14:42	3,28,30	20.13	7.1*
			CP1	13:00-15:00	0-60	14.38	8.0*
			Inversion	-	-	6.89	5.33
D	10/15/2015 18:53-22:07	10.5	CR1	19:00 - 19:42	0,35,59	79.8	7.1*
			MP4	08:22 - 14:42	3,30,28	53.17	7.1*
			CP1	18:00 - 22:00(ND)	0-60	49.56	8.7*
			Inverson	-	-	8.09	19.19
E	10/16/2015 19:23 - 21:19	10.6	CR2	19:42	50	57.29	8.8
			MP1	18:38	30	35.54	10.3
			CP1	19:00 - 21:00	0-60	162.1	11.9*
			Inversion	-	-	10.62	16.7
F	10/17/2015 13:57-15:09	10.7	CR1	14:00 - 14:42	0,29,30	18.2	9*
			MP1	18:25	28	14.28	7.8
			CP4	13:00	0-60	22.54	9
			Inversion	-	-	5.35	6.22
G	10/17/2015 18:19-20:08	10.8	CR3	19:12	29	62.44	9.3
			MP2	08:07 - 18:25	4,28,29,30	25.55	8.5*
			CP2	19:00	0-60	371.55	11.5*
			Inversion	-	-	9.06	14.99
H	10/18/2015 18:33-20:19	10.8	CR2	23:42	32	33.04	13.9
			MP	-	-	N/A	N/A
			CP4	22:00 - 00:00(ND)	0-60	46.75	14.4*
			Inversion	-	-	12.81	19.98
I	10/19/2015 14:13-15:35	10.4	CR2	15:12	30	22.13	9.8
			MP	-	-	N/A	N/A
			CP4	15:00	0-60	41.51	10
			Inversion	-	-	9.96	8.45
J	10/20/2015 15:42-17:09	10.7	CR4	16:00 - 16:42	0,29,29,30	271.6	8.5*
			MP1	15:29	30	160.99	9.9
			CP4	16:00	0-60	146.6	6.4*
			Inversion	-	-	18.78	18.83
K	10/20/2015 20:29-22:09	11.1	CR4	20:40 - 22:12	0,33,34,42,49	30.91	5.2*
			MP2	07:00 - 12:57(ND)	4,30,45	38.26	10.8*
			CP3	20:00 -22:00	0-60	70.68	9.1*
			Inversion	-	-	8.68	16.34
L	10/21/2015 12:34-14:54	10.4	CR3	13:42	16	10.53	5.8
			MP1	12:57	4	13.22	6.4
			CP1	12:00-14:00	0-60	29.9	5.3*
			Inversion	-	-	3.16	6.6

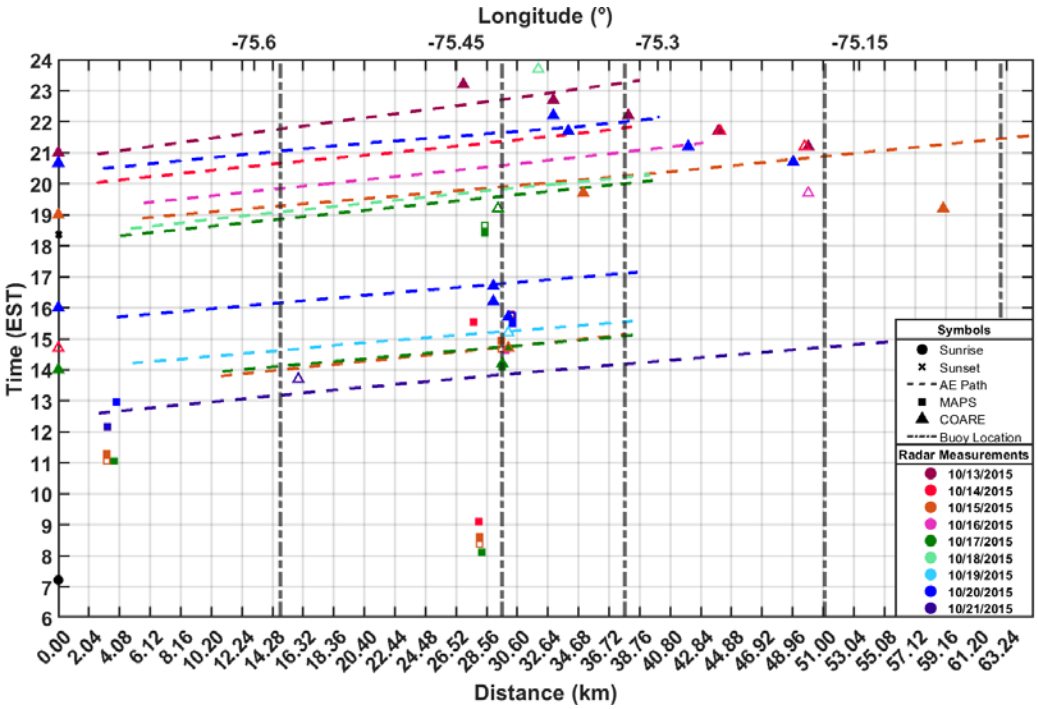

Figure 5.1. Temporal and spatial coverage of the R/V Atlantic Explorer (AE) RF measurement tracks, MAPS, COARE, and COAMPS®-NAVSLaM refractivity profiles, and moored wave buoys. The y-axis represents hours that span measurements performed throughout CASPER-East, and the x-axis represents the offshore distance or range from Duck pier which is located at the origin. Distance from the pier is shown in both km (bottom x-axis) and longitudinal position (top x-axis); resolution of the x- and y- axis corresponds to the COAMPS® spatial and temporal resolution, respectively, where intersection of the temporal and spatial lines indicates a COAMPS® prediction/forecast. Colors correspond to the day on which measurements occurred for each RF dataset. Filled markers represent refractivity profiles that contribute to a mean profile where hollow markers indicate singular profiles, which are incorporated in either range dependent or range independent refractivity forward models. This figure shows data outlined in Table 5.1. COAMPS®-NAVSLaM refractivity estimates exist at the locations denoted by the nodes on the spatiotemporal grid.

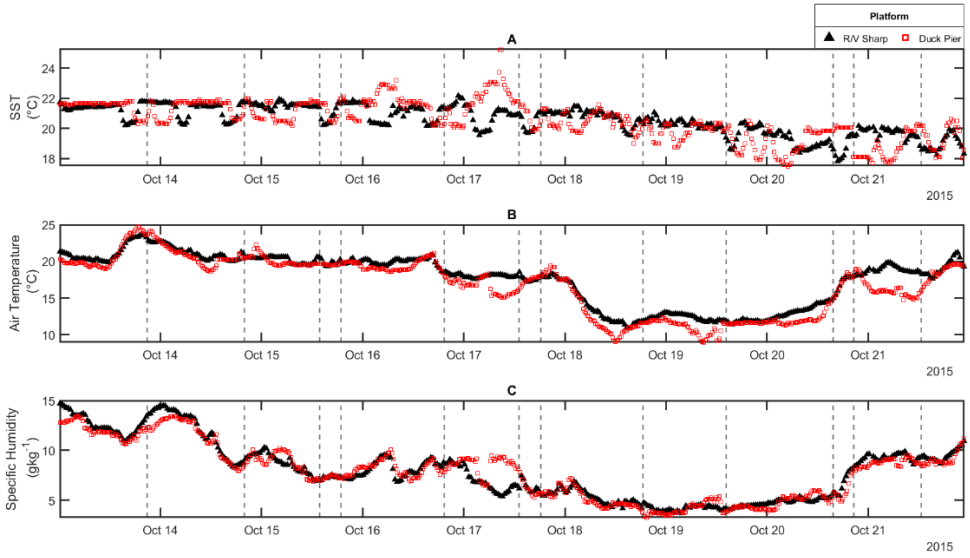

Figure 5.2. Time series of thermodynamic variables, (A) sea surface temperature (SST), (B) air temperature, and (C) specific humidity, measured at Duck Pier and aboard the R/V Sharp during CASPER-East associated with the time periods of the radar measurements – see Table 5.1. The vertical black dashed lines denote start times of the RF measurements used in the inversions.

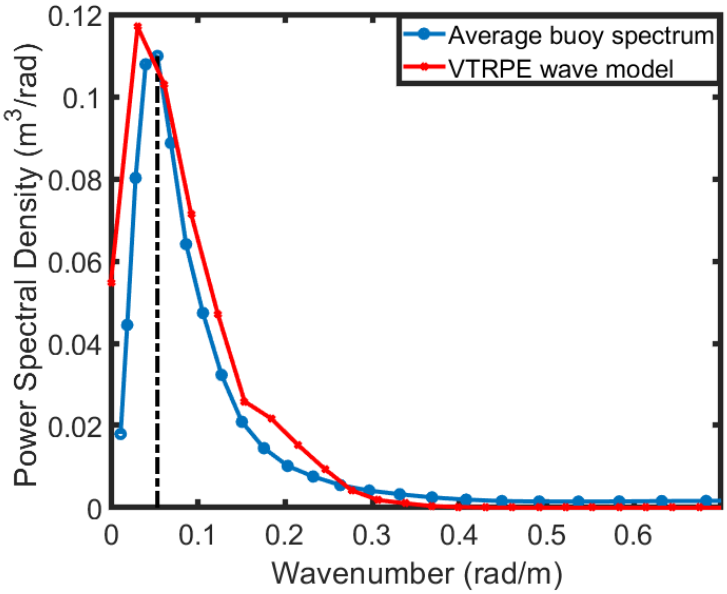

Figure 5.3 Example sea state spectra from the wave buoys and the VTRPE wave model for 21 October 2015. Peak wavelength from the average wave buoy spectrum is ~117m (vertical black dashed line) and the significant wave height is 0.43m. The VTRPE wave model has a peak wavelength of 150m with a significant wave height of 0.43m.

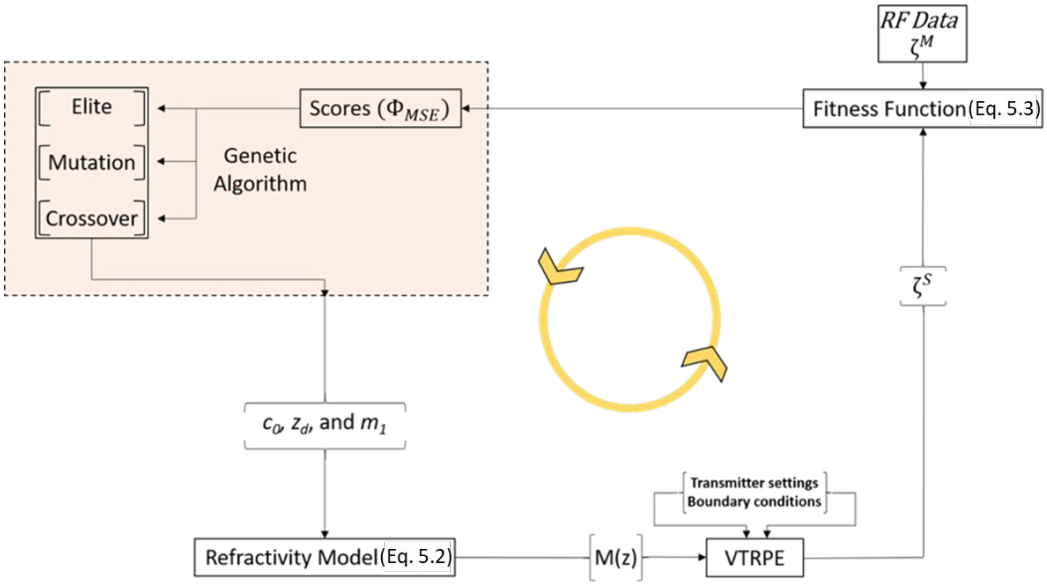

Figure 5.4. Depiction of the inversion procedure illustrating the iterative GA process.

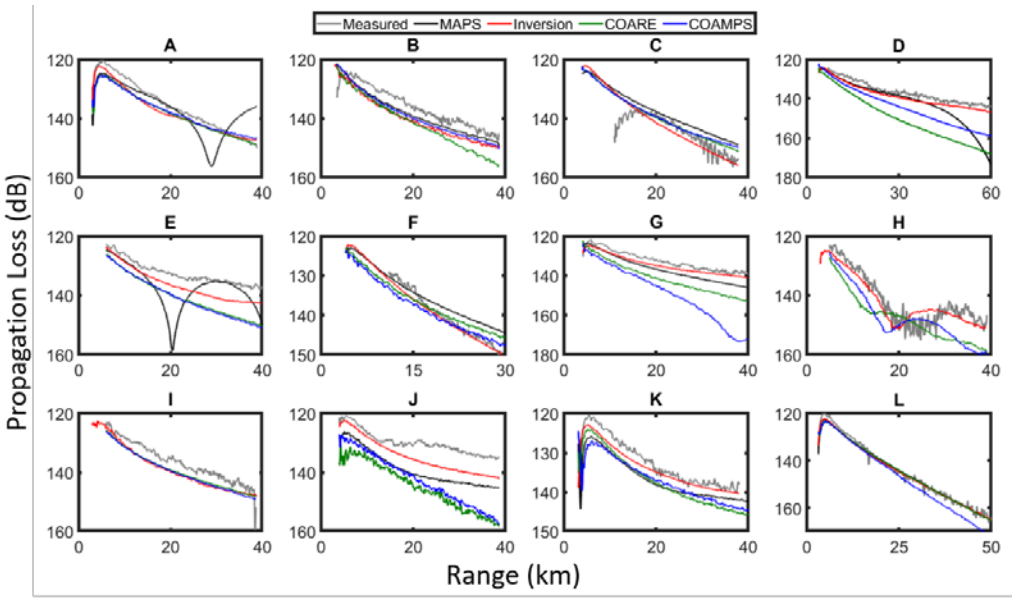

Figure 5.5. ζ^S at 4m for the forward model option with the lowest MSE for each method, and the inversion-based propagation loss along with measured RF data (4m receiver height). ζ^S predictions shown here are considered to be the "best" representation of measured propagation from each method (§5.53). A-L follow in order of the experiments outlined in Table 5.1.

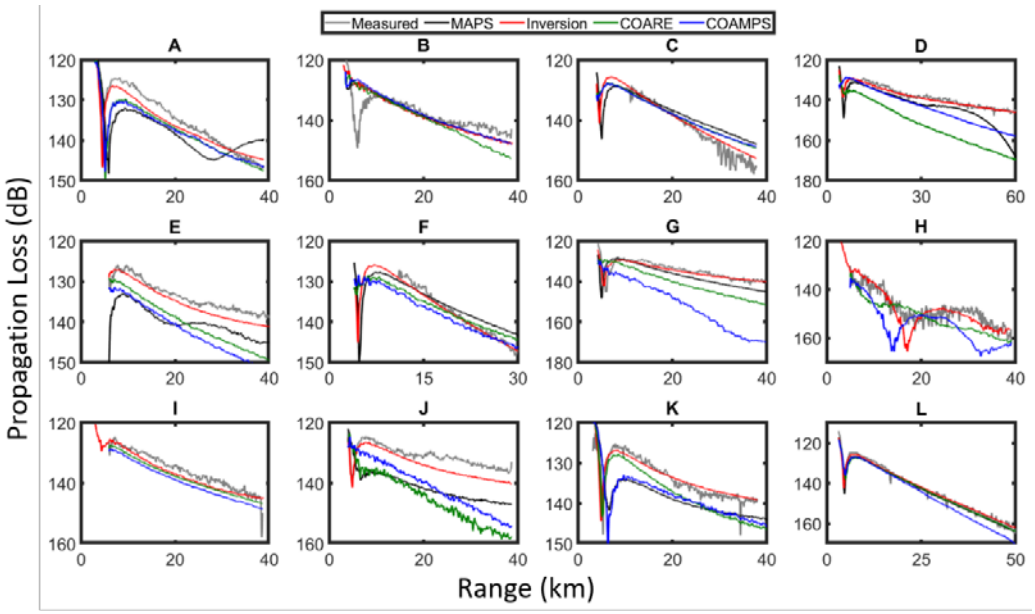

Figure 5.6. ζ^S at 6m for the forward model option with the lowest MSE for each method, and the inversion-based propagation loss along with measured RF data (6m receiver height). All other aspects of the data shown here are the same as that described in the Figure 5.5 caption.

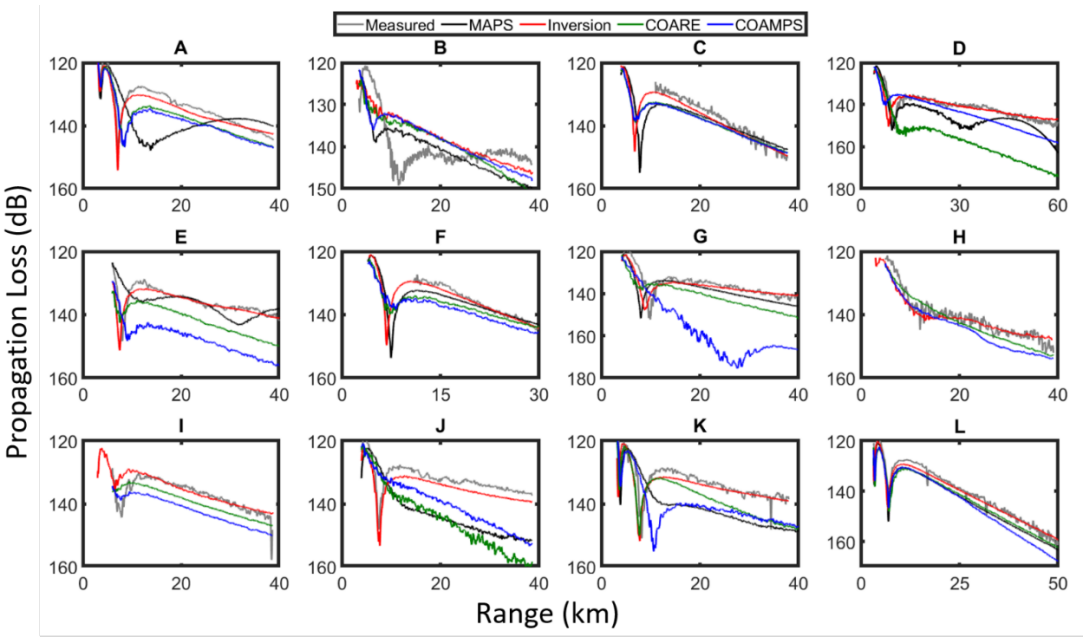

Figure 5.7. ζ^S at 9m for the forward model option with the lowest MSE for each method, and the inversion-based propagation loss along with measured RF data (9.2m receiver height). All other aspects of the data shown here are the same as that described in the Figure 5.5 caption.

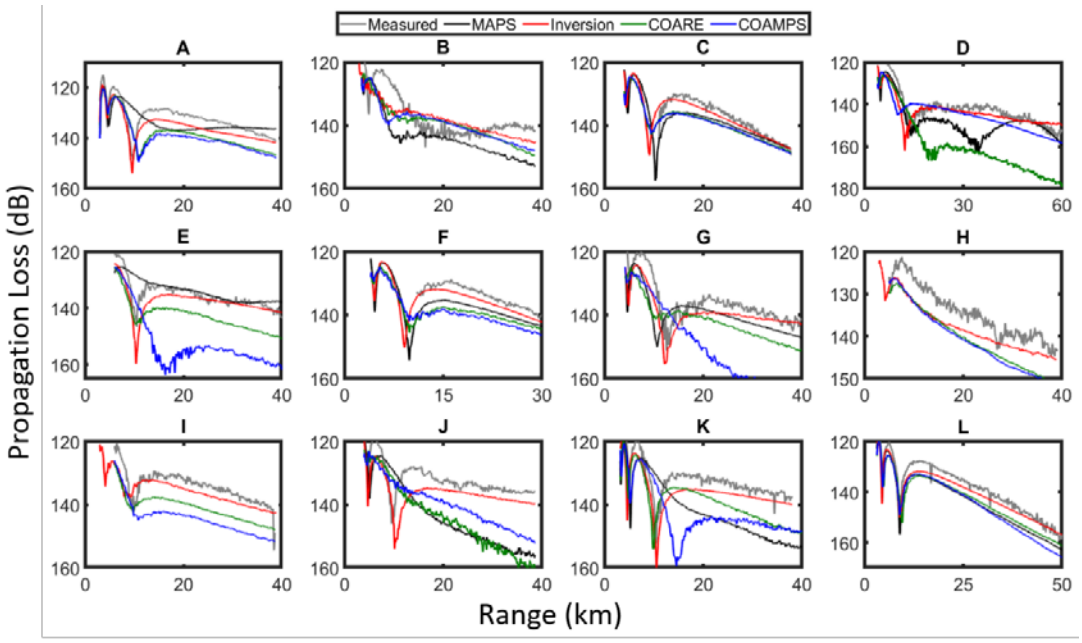

Figure 5.8. ζ^S at 12m for the forward model option with the lowest MSE for each method, and the inversion-based propagation loss along with measured RF data (12.3m receiver height). All other aspects of the data shown here are the same as that described in the Figure 5.5 caption.

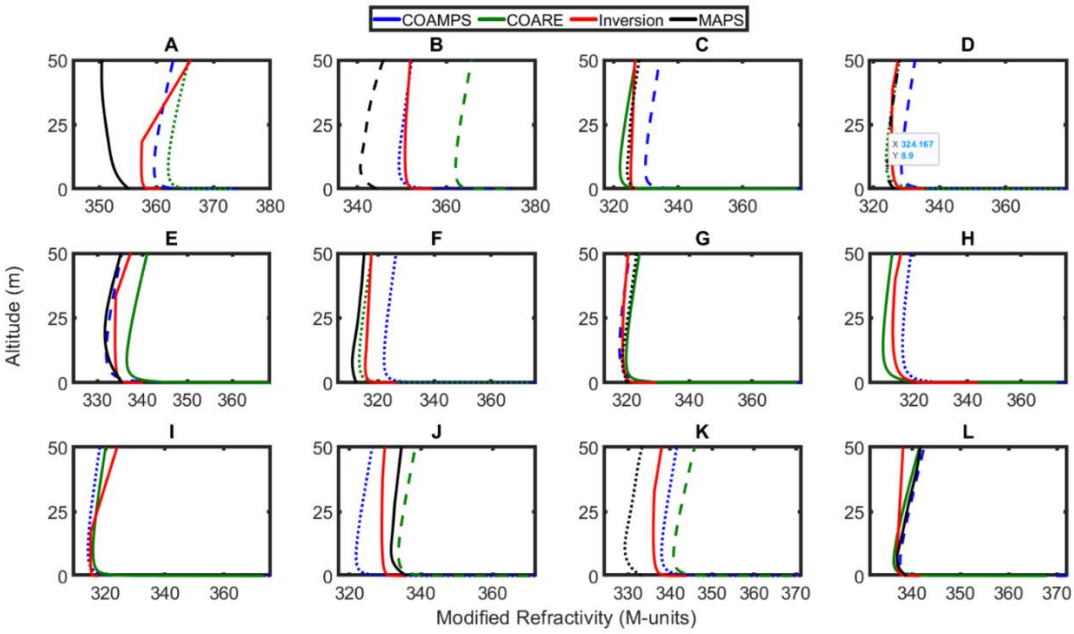

Figure 5.9. Modified refractivity profiles for the forward model with the lowest PL MSE for each method and inversion result for each experiment. Range-dependent profiles are not shown for clarity, instead, solid lines denote range-independent (singular) refractivity profiles, dotted lines denote one range-independent mean profile, and dashed lines denote range-dependent (multiple) refractive profiles averaged over range for illustrative purposes. Surface refractivity for inversion profiles is shifted such that modified refractivity at the EDH is the mean refractivity of the other environmental estimates at the EDH. A-L correspond to experiments outlined in Table 5.1.

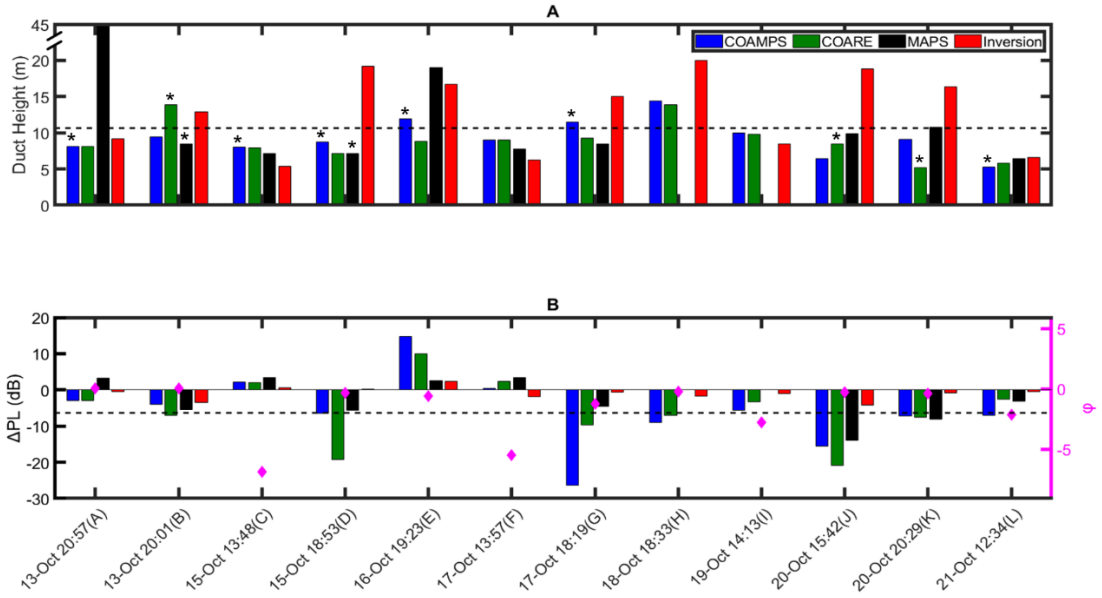

Figure 5.10. (A) Duct heights for each forward method and the inverse solution for all experiments where the horizontal dashed line represents average EM transmitter height. EDH in (A) for range dependent refractivity is a mean EDH over range, denoted with an asterisk. (B) Difference between measured and modeled propagation loss averaged over all receiver heights and ranges greater than 30km on the left y-axis and average atmospheric stability (φ) on the right y-axis. Φ = -2 is marked by the horizontal dashed line in (B). Experiment label corresponding to Table 5.1 precedes the radar start time on the x-axis.

Chapter 6

On the Variability of *In-situ* Surface Layer Refractivity Measurements[3]

Nomenclature	Definition
ASTD	Air Temperature Standard Deviation
C_n^2	Refractive Index Structure Constant
COARE	Coupled Ocean-Atmosphere Response Experiment
e	Partial Water Vapor Pressure
IOR	Index of Refraction
L_z	Outer Length Scale
M’	Modified Refractivity Fluctuation
M	Modified Refractivity
MAPS	Marine Atmospheric Profiling System
MASL	Marine Atmospheric Surface Layer
MO	Monin-Obukhov
MOST	Monin-Obukhov Similarity Theory
NAVSLaM	Navy Atmospheric Vertical Surface Layer Model
P	Percentile
p	Pressure
PSO	Particle Swarm Optimization
Q	Quantile

[3] This chapter is based on the published article listed below:
Pastore, D. M., R.T., Yamaguchi, Q. Wang, & Hackett, E. E. (2023). On the Variability of *In-situ* Surface Layer Refractivity Measurements. Atmosphere, 14(7), 1085.

Nomenclature	Definition
q	Specific Humidity
R/V	Research Vessel
RH	Relative Humidity
RMS	Root Mean Square
SD	Scintillation-Derived
SST	Sea-Surface Temperature
T	Temperature
TRIF	Turbulent Refractive Index Fluctuation
γ_{Tq}	Humidity Correlation Coefficient
θ	Potential Temperature
Ω_{FIT}	Fitness Function Error

6.1 Chapter Introduction

Chapters 3 and 4 have shown that while use of a mean refractivity profile for prediction of propagation can result in reasonable comparisons with measured propagation, discrepancies also exist. One of the reasons that measured propagation data may differ from propagation predictions using mean refractivity is due to the fast propagation speed of EM waves (i.e., speed of light). These EM waves are propagating through the mean atmosphere but also a "frozen" field of refractivity fluctuations due to MASL turbulence. To evaluate the impact of turbulence on EM propagation predictions, a turbulence model that can be implemented into a propagation simulation must be evaluated. As described in Chapter 2, models of refractive index turbulent fluctuations exist, and are implemented in this chapter. Modeled refractive index fluctuations are compared with direct measurement of refractivity near the ocean surface. Direct measurements within the marine atmospheric surface layer often and inevitably contain a large degree of variability. The variability

observed can be explained through numerous technical and natural reasons – such as temporal variability over the time span a profile is measured (unsteadiness in the mean), spatial variations (inhomogeneity), turbulent fluctuations, and measurement uncertainty. This chapter implements a turbulent refractive index fluctuation model to address, objective (iii) of this work given in Chapter 3. If model can be shown to replicate observed variability in vertical distributions of refractive index measured with a tethered-balloon-based Marine Atmospheric Profiling System (MAPS) deployed during CASPER-East, the variability of the data can be explained, and the model is verified.

6.2 CASPER-East Measurements

The CASPER-East field campaign occurred over 25 days in 2015 between 12 October and 6 November (Wang et al., 2018). The following paragraphs describe measurements made within the MASL by MAPS and aboard the Research Vessel (R/V) Sharp. Comprehensive discussion of the CASPER-East campaign can be found in (Wang et al., 2018).

The MAPS system was constructed of a radiosonde attached to a balloon tethered to a small workboat, using a winch to control the ascent and decent of the system from ~0.5 m to ~50 m in altitude. The workboat used to deploy MAPS is small enough that its effects on the measured environment are considered minimal (Kang and Wang, 2016). MAPS datasets are composed of pressure (p), temperature (T), and relative humidity (RH), where T and RH were converted to potential temperature (θ) and specific humidity (q), respectively. T, q, and p data were fit with a 7^{th} order polynomial for each MAPS dataset as in (Kang and Wang, 2016). A time series of these variables at 12 m altitude are illustrated in Figure 6.1 along with bulk meteorological measurements (30 min averages) made aboard

the R/V Sharp. Vertical profiles of modified refractivity (M) are computed from the mean meteorological profiles via (Bean and Dutton, 1996):

$$M = \frac{77.6}{T}\left[p + \frac{4810e}{T}\right] + \left(\frac{z}{a}\right) \times 10^6 \quad (6.1)$$

where z is the height above the earth's surface, a is the radius of the earth, and e is the partial water vapor pressure (millibars) computed with q and T to estimate the saturation vapor pressure (Buck, 1981). The polynomial fits of mean p, T, and RH are based-on data measured down to ~0.5m; thus, the polynomial fit is also used to extrapolate M to the surface to obtain surface refractivity (M_0). It was found that this 7th order polynomial better captured near-surface variations than linear or other lower order polynomial fits, and it also results in a smoother vertical refractivity profile than using a method like bin-averaging the data over altitude (Figure 6.2). A more extensive discussion of this methodology can be found in (Rainer, 2016; Alappattu et al., 2016).

MAPS measurements of p, T, and RH have been thoroughly verified (Kang and Wang, 2016; Wang et al., 2018; Rainer, 2016; Alappattu, 2016), this paper focuses on the modified refractivity estimated from these measurements. MAPS datasets used in this study are displayed in Table 6.1, showing 36 deployments of the system were performed over the course of CASPER-East and on average, each deployment lasts 26 minutes and contains ~1158 samples. Numerous ascents and subsequent descents of MAPS occur during each deployment, where the following use of the term "launch" will describe one ascent/descent of the system, each lasting on average ~3.5 min. For each MAPS deployment, multiple launches occurred. For this study, MAPS refractivity estimates are truncated above 50 m to remove measurement uncertainties occurring due to reorientation

of the system from ascent to descent (Rainer, 2016; Alappattu, 2016). Four examples of MAPS datasets from CASPER-East are illustrated in Figure 6.2; the 7th order polynomial fit representing the mean and, for comparison, a 1 m altitudinally binned mean profile is shown, where the former is utilized as the mean profile in this study. MAPS measurements, and subsequent estimates of refractivity, individually, can be considered instantaneous (within the longest response time of the sensors - ~1s) and can thus be decomposed as:

$$M(z) = \bar{M}(z) + M'(z) \tag{6.2}$$

where the overbar and prime denote a mean and fluctuation, respectively. In Figure 6.2, instantaneous MAPS-based M are shown as markers and the 7th order polynomial fits, representing the mean of the markers, is shown as a black line ($\bar{M}$). Refractive index fluctuations (M') computed from (6.2) are illustrated in Figure 6.3. The mean M' for all MAPS datasets are approximately zero as exemplified in Figure 6.3 for the same datasets shown in Figure 6.2. This comparison confirms that the polynomial fit is a reasonable estimate of $\bar{M}$.

In conjunction with the MAPS deployments, meteorological and sea surface measurements were conducted aboard the R/V Sharp. Wind speed was not measured by MAPS and is needed for estimation of C_n^2, discussed in section 6.3.2; thus, wind speed is obtained from an anemometer aboard the R/V Sharp bow mast (z =12 m) averaged over 30-minute intervals. Skin sea surface temperature (SST) is also measured aboard the R/V Sharp corrected from the 5-minute bulk SST (Wang et al., 2018A; Pastore et al., 2021). Time series of R/V Sharp SST and wind speed are displayed in Figure 6.1.

6.3 Turbulent Refractive Index Fluctuations Model (TRIF)

Previous studies have modeled turbulent refractive index fluctuations using a variety of models for representing turbulence—such as Gaussian, von Karman, and Kolmogorov-based spectral models (Rouseff, 1992; Levadnyi et al., 2012; Wagner et al., 2016). Because a Kolmogorov-based spectral model only emulates turbulence in the inertial subrange, it is easier to incorporate anisotropy into the model, which is a key characteristic of turbulence in the MASL. Therefore, an anisotropic Kolmogorov-based turbulent refractive index fluctuation model (TRIF) was implemented in this study (Rouseff, 1992). Details of the implementation of this Kolmogorov model are discussed in Section 3.1, where it is revealed that a refractive index structure constant is needed for the model. The method for estimating this structure constant is described in Section 3.2.

6.3.1 Spectral Modeling of Turbulent Refractive Index Fluctuations

Refractivity is assumed to be constantly perturbed by continuous fluctuations due to atmospheric turbulence. Random fluctuations, as defined in (6.2), are modeled stochastically. The stochastic fluctuating component of the index of refraction (IOR) is described by the Kolmogorov spectrum derived by (Ishimaru, 1978):

$$\emptyset(\boldsymbol{k}) = \frac{0.033C_n^2}{(L_0^{-2} + \boldsymbol{k}^2)^{\frac{11}{6}}} \tag{6.3}$$

where C_n^2 is in units of $m^{-2/3}$, L_0 has units of meters, and $\boldsymbol{k}$ is the 3-dimensional wavenumber vector. The anisotropic MASL can be introduced into (6.3) via α, a parameter describing the relationship between horizontal and vertical outer length scales, L_x and L_z, where $L_z = \alpha L_x$ (Rouseff, 1992; Levadnyi et al., 2012; Wagner et al, 2016); thus:

$$\emptyset(\kappa_x, \kappa_y, \kappa_z) = \frac{0.033 C_n^2}{\left(L_x^{-2} + \kappa_x^2 + \kappa_y^2 + \alpha^2 \kappa_z^2\right)^{\frac{11}{6}}} \tag{6.4}$$

for this study, α = 0.27 (Emes et al., 2019). To collapse the three-dimensional spectrum in (6.4) into one-dimensional space, the transverse vertical spectrum is adopted as derived in (Rouseff, 1992; Levadnyi et al., 2012):

$$S_n(\kappa_z) = (2\pi)^2 \delta x \int_{-\infty}^{+\infty} \emptyset(\kappa_x = 0, \kappa_y, \kappa_z) d\kappa_y \tag{6.5}$$

where δx is a scaling factor that would account for the distance between realizations of vertical turbulent profiles in a numerical model. In the present study, we were not generating realizations within a numerical model but rather comparing a single vertical refractive index fluctuation realization to each MAPS dataset, so no scaling was required; thus, we simplify $\delta x = 1$ in (6.5). Substituting (6.5) into (6.4) results in the one-dimensional transverse spectrum:

$$S_n(\kappa_z) = (2\pi)^2 \frac{\Gamma\left(\frac{1}{2}\right)\Gamma\left(\frac{4}{3}\right)}{\Gamma\left(\frac{11}{6}\right)} \alpha^{-\frac{8}{3}} \frac{0.033 C_n^2}{(L_z^{-2} + \kappa_z^2)^{\frac{4}{3}}} \tag{6.6}$$

where $\Gamma(x)$ is a gamma function. The full derivation of (6.6) can be found in (Rouseff, 1992; Levadnyi et al., 2012; Wagner et al., 2016). Realizations of refractive index fluctuations from $S_n(\kappa_z)$ are found using the approximate frequency domain method proposed in Percival (1993) and similarly implemented in Wagner et al. (2016). Realized refractive index fluctuations are related to modified refractivity by:

$$M = \left(n - 1 + \left(\frac{z}{a}\right)\right) \times 10^6 \tag{6.7}$$

where n is the IOR.

6.3.2. NAVSLaM Estimates of C_n^2

Estimation of C_n^2 is performed via NAVSLaM Version 1.2 (Frederickson, 2016), which is based on MO similarity theory, and estimates near-surface profiles of thermodynamic properties and wind as well as related scaling parameters of the air-sea fluxes of momentum, sensible heat, and latent heat (Frederickson, 2016). NAVSLaM employs parameterizations from COARE (Fairall et al., 1996; Fairall et al., 2003) and is only valid within the surface layer where turbulent fluxes vary by 10% or less (i.e., assumption of a constant flux layer). NAVSLaM is chosen for estimation of C_n^2 due to the dynamic employment of MO similarity theory stability functions for differing stability regimes. NAVSLaM requires the following parameters to estimate C_n^2: skin sea-surface temperature, wind speed, specific humidity, and temperature at a reference height. SST and wind speed are obtained from measurements aboard the R/V Sharp since these were not measured by MAPS; specific humidity and temperature are obtained from mean meteorological measurements of MAPS at $z = 12$ m matching the altitude of wind speed measurements from the R/V Sharp. R/V Sharp measurements were conducted synchronously with MAPS measurements and were located at a distance, on average, of 0.6 km away from the location of MAPS deployments (Pastore et al., 2021).

Estimation of the refractive index structure constant (at z = 12 m) is performed via NAVSLaM for the 36 MAPS deployment times as:

$$C_n^2 = z^{-\frac{2}{3}} f(z/L)\left(A^2 T_*^2 + 2AB\gamma_{Tq} T_* q_* + B^2 q_*^2\right) \tag{6.8}$$

where A and B are constants for radio frequencies (Frederickson et al., 2000). Subscript $*$ denotes a MOST scaling parameter (Businger et al., 1971; Frederickson et al., 2000) and $f(z/L)$ represents the MO theory stability functions employed in NAVSLaM

(Frederickson, 2016) γ_{Tq} is the temperature-specific humidity correlation coefficient, commonly 0.8 (Frederickson et al., 2007; Qing et al., 2017).

6.4 Particle Swarm Optimization

The TRIF model is optimized to the (instantaneous) MAPS refractivity datasets using particle swarm optimization (PSO) (Kennedy et al., 1995; Poli et al., 2007). PSO is implemented to investigate the physical significance of MAPS estimated refractivity fluctuations because a direct estimate of any vertical length scale is not possible with the MAPS data directly, and model complexity prohibits directly solving for L_z based on MAPS measurements. PSO is used to optimize the TRIF model to yield the best match to the statistical properties of the MAPS datasets as measured by a fitness or objective function. Because NAVSLaM is used to estimate C_n^2, PSO optimizes the TRIF model for L_z. PSO iterates through the L_z search space which ranges from 0.1 m to 50 m; such a large range is considered for L_z to incorporate the majority of possible outer length scales within the surface layer (Wheelon, 2001; VanZandt et al., 1978). If the PSO optimized length scales are reasonable given the atmospheric stability regime, then that is an indicator that the majority of the observed variance in the MAPS measurements can be attributed to turbulence.

PSO is a stochastic technique, which is a biology-inspired population-based dynamic system where a potential solution (or particle) is introduced into a solution space, with dimensions corresponding to the number of solution parameters, with a multitude of potential solutions (or swarm of particles). Each particle in the swarm moves through the solution space at a unique velocity, which is determined by the unique particle's "best" solution from previous exploration of the solution spaces and the global "best" solution

from the swarm over all previous solutions spaces. In this study, the solution parameter, or particle, is L_z from the TRIF model which corresponds to a 1-dimensional solution space (equation 6.6). Swarm size for the optimization is set to 30 and optimization is considered complete once the relative change in the objective function between consecutive swarms, after a minimum of 20 swarm iterations, is less than 10^{-6} M-units^2 (see objective function below). More information on PSO can be found in (Kennedy et al., 1995; Poli et al., 2007).

The fitness or objective function determines how "good" a particular particle is within the PSO and therefore should focus on the properties that the optimization is targeting—in this case, the MAPS dataset variability. To match the variability as well as possible, the fitness function compares quantiles of the cumulative probabilities of refractivity fluctuations between TRIF model refractivity and MAPS refractivity measurements. One hundred evenly spaced quantiles (or percentiles) are delineated for modified refractivity fluctuations for both the TRIF model and MAPS measurements. Quantiles (Q_P) are found via ordinal ranking (R_P) as

$$R_P = \left(\frac{P}{100}\right) N_s \tag{6.9}$$

where P is the percentile ($P = 1,2,3,4, \ldots 100$), and N_s is the number of samples in the dataset. Modified refractivity fluctuations are sorted from smallest to largest, and R_P identifies which value within the sorted dataset corresponds to each Q_P; thus, each quantile is associated with an M' value. For example, in MAPS dataset 2 (Figure 2A), N_s = 1264, if $P = 2$, then $R_2 = 25.3$, and Q_2 is sample 26 in the sorted dataset, −2.03 M-units (Figure 4A). This M' accounts for 2% or less of all M' in the dataset.

The quantile-based approach allows for the comparison of the cumulative probability distributions between MAPS and TRIF refractive fluctuations. A probability

distribution-based approach is logical due to the differing sample sizes between MAPS measurements and TRIF realizations of refractive fluctuations. Comparison of the quantiles between the two datasets is performed using mean-square error resulting in the fitness score:

$$\Omega_{Fit} = \frac{1}{N_Q}\sum_{P=1}^{N_Q}(Q_P^M - Q_P^T)^2 \tag{6.10}$$

where Q_P is the M' for the Pth percentile computed for either the MAPS dataset, Q^M, or the TRIF model dataset, Q^T. N_Q = 100, corresponding to the hundred quantiles delineated for each dataset. Minimization of (6.10) ensures that the statistical characteristics (i.e., mean, median, and variance) of M', for both TRIF and MAPS, are similar. Thus, relatively small Ω_{Fit} would indicate that the TRIF model appropriately estimates the distribution of MAPS refractive index fluctuations. Example MAPS and TRIF quantiles for MAPS datasets illustrated in Figures 6.2 and 6.3 are displayed in Figure 6.4.

6.5 Results and Discussion

TRIF model optimization of the vertical length scale, L_z, are compared with previous reported ranges of L_z within the atmospheric surface layer. Further, the TRIF model is used to simulate the MAPS data cloud, which are also compared directly. These results are exemplified with the four MAPS deployments illustrated in Figures 6.2 and 6.3. These examples are chosen because they represent the best (Figure 6.3A), average (Figure 6.3B), and worst (Figure 6.3D) comparisons between the TRIF model and MAPS data. The last example was chosen because it had the least MAPS measurements (Figure 6.3C) used for the optimization. These results enable insight into the source of the scatter in the MAPS measurements.

6.5.1. Vertical Length Scale - L_z

Vertical outer length scales from the PSO experiments range from 2.96 m to 17.02 m, with an average of 5.80 m over the MAPS datasets (Table 6.1). Bulk C_n^2 and corresponding L_z for the 36 optimizations are illustrated in Figure 6.5. L_z are visually compared to vertical outer length scales from Emes et al. (2019) and VanZandt et al. (1978) in Figure 6.5B. Authors in Emes et al. (2019) estimate L_z over multiple stability regimes (i.e., convective, neutral, and stable) yielding a range of values shown as the grey shaded region in Figure 6.5B. These vertical length scales included from Emes et al. (2019) are approximated at 12 m, chosen to be consistent with the TRIF model utilizing C_n^2 estimated from meteorological data at this altitude. Generally, L_z fall close to the values reported (Emes et al., 2019) apart from two MAPS datasets (24, 27) associated with near thermal neutrality. Because the optimized L_z are generally consistent with ranges in the literature, one can conclude that the MAPS data cloud could be largely driven by turbulence. If the optimization revealed an unrealistic/non-physical L_z (e.g., several orders of magnitude off the true value) to match the MAPS data, then that would have indicated that uncertainty could be a significant factor. Thus, MAPS estimated refractivity variance is potentially representative of physically relevant fluctuations in the refractive index.

To further confirm the physical nature of the optimized L_z, correlation between C_n^2 and L_z is examined. L_z reveals a significant inverse relationship with C_n^2 shown by a correlation coefficient (R) of -0.53 with a p-value << 0.05. This result is contrary to expectations as it suggests decreasing vertical outer length scales as C_n^2 increases. Presumably, in thermally unstable conditions, the increase in buoyant effects generating convective plumes, would increase both the magnitude of turbulence (C_n^2) and L_z, leading

to a direct relationship. While in stable conditions, vice versa, one would assume that the stable stratification would inhibit development of large-scale fluctuations.

To further investigate the indirect relationship between C_n^2 and L_z, we explored possible sources of error in the comparisons. One source of uncertainty is due to the C_n^2 estimate being based on an average condition (i.e., based on bulk meteorological measurements), while the MAPS measurements used for the optimization are individually instantaneous (to order 1s). Secondly, the assumption of a constant C_n^2 with altitude can also result in uncertainty. And finally, Frederickson et al. (2007) reported that for ASTD > -1 ℃ bulk C_n^2 estimates deviate from scintillation-derived (SD) C_n^2. For cases of near thermal neutrality (-0.5℃ < ASTD < 0.5 ℃) bulk C_n^2 can underestimate SD C_n^2 by greater than one order of magnitude for certain wind and humidity conditions. This underestimation can presumably explain MAPS deployment 27, where near neutral conditions are observed (ASTD = 0.11℃) corresponding to an abnormally low C_n^2 (2.97×10^{-14} $m^{-2/3}$) and the largest L_z (17.02 m). This underestimation of C_n^2 effectively leads to overestimation of L_z to match the observed fluctuations, shown in MAPS deployment 24, where a near neutral environment is also observed (ASTD = -0.26 ℃). For these cases, the relatively small C_n^2 does not correspond with relatively small RMS MAPS refractive fluctuations, thus a large L_z is derived by the optimization compensating for the small C_n^2. Further, Frederickson et al. (2000) also reported that during periods of thermal stability (ASTD > 1 ℃) bulk C_n^2 estimates can be overestimated up to one order of magnitude. For this study, the over estimation of C_n^2 would lead to derived L_z that are smaller than expected. These uncertainties in NAVSLaM bulk C_n^2 estimates could cause the indirect relationship between C_n^2 and L_z. Thus, since L_z fall within the previously reported ranges

of vertical outer length scales and considering some stability dependent error in the bulk estimation of C_n^2, it is plausible that the majority of the refractive fluctuations in the MAPS measurements are indicative of inertial to large-scale turbulent physical processes.

6.5.2. Refractive Fluctuations

TRIF modeled refractivity fluctuations using L_z derived via PSO for the example MAPS deployments (MAPS 2, 11, 9, and 33) are illustrated in Figure 6.6 and the associated instantaneous distributions of refractivity are displayed in Figure 6.7. For these examples, TRIF model fluctuations optimized to corresponding MAPS refractivity have a Ω_{Fit} of 0.001 M-units^2 (Figure 6.6A), 0.036 M-units^2 (Figure 6. 6B), 0.009 M-units^2 (Figure 6.6C), and 0.260 M-units^2 (Figure 6.6D), for MAPS deployments 2, 11, 9, and 33, respectively. The discrepancies between the Ω_{Fit} for the examples displayed in Figure 6.6 are visually apparent. TRIF fluctuations mostly occur within the bounds of MAPS refractivity in Figure 6.6A, 6.6B and 6.6C, corresponding to relatively low Ω_{Fit}, this is not the case for Figure 6.6D. Most experiments (32 of 36) are on the order of the mean Ω_{Fit} (0.047 M-units^2) and are visually akin to Figure 6.6B. Conversely in Figure 6.6D, TRIF fluctuations tend to overestimate MAPS refractivity at altitudes greater than ~8 m and underestimate MAPS fluctuations below this 8 m altitude. As expected from this discrepancy, MAPS deployment 33 corresponds to the largest (worst) Ω_{Fit} relative to all MAPS deployments. This result is presumably due to the varying magnitudes of refractive fluctuations over altitude (Figure 6.6D). These variable fluctuations in MAPS as a function of altitude are not accounted for in the TRIF model as turbulence is assumed homogenous with altitude – i.e., C_n^2 and L_z are estimated as one value for the entire profile.

The assumption of homogenous turbulence within TRIF is questionable for C_n^2 in the surface layer (Rouseff, 1992; Chou and Kiang, 2014; Geernaert, 2003) but is a reasonable assumption for L_z (Rouseff, 1992). Thus, the assumption of C_n^2 homogeneity is presumably a main driver of variation in fitness function over the 36 optimizations. The altitudinal inhomogeneity is illustrated in Figure 6.8, where fitness score is shown relative to variance of the MAPS data. M' variance is computed over two altitudinal bins, 0 – 10 m (δ_A) and 10 – 20 m (δ_B) exploring heterogeneity of the environment. δ_A is larger than δ_B for 28 of the 36 deployments, reinforcing that the assumption of vertical homogeneity is not ideal (Figure 6.8A). Additionally, this result gives physical context to variations in the MAPS measurements; further supporting the physical nature of the fluctuations captured by the MAPS measurements as one would expect turbulent fluctuation magnitudes to be largest near the surface.

Generally, experiments shown to have the largest differences between δ_A and δ_B correspond to the largest fitness scores (poorest fit between MAPS and TRIF refractive fluctuations). This result (Figure 6.8B) is verified through linear correlation between Ω_{Fit} and $|\delta_A - \delta_B|$, yielding $R = 0.75$ ($p << 0.05$) - a significant direct relationship. Thus, as the assumption of vertically homogenous turbulence degrades so follows the TRIF model accuracy; however, even the largest $\sqrt{\Omega_{Fit}}$ are small relative to the RMS M', suggesting TRIF can adequately model fluctuations in the cases presented. This result further suggests that PSO-estimated L_z falling within the ranges presented in Figure 6.5 are plausible and support the notion that MAPS fluctuation variances are primarily related to physical processes.

6.6 Summary and Conclusions

This study incorporates a novel meteorological dataset acquired with MAPS and deployed during the CASPER-East field campaign (Wang et al., 2018A). This dataset is used to examine the physical significance of variability within those measurements that were performed within the MASL. MAPS (Kang and Wang, 2016) is a cutting edge MASL measurement technique able to obtain vertical distributions of measurements of pressure, temperature, and humidity and, thus, refractivity at high temporal resolution. The goal of this study is to investigate variance captured by these MAPS measurements and determine whether it can be explained by turbulent physical processes. To do this, the turbulence refractive index fluctuation (TRIF) model is implemented. TRIF is a spectral turbulence model based on a 1-D vertically homogenous anisotropic Kolmogorov spectrum that includes parameters describing magnitude of the refractive index fluctuations (C_n^2) and vertical turbulent outer length scales (L_z). C_n^2 are estimated via bulk methods from MAPS and R/V Sharp meteorological measurements including SST, implemented via NAVSLaM. L_z are derived via PSO utilizing TRIF for 36 MAPS datasets of modified refractivity, which are decomposed into fluctuations. The derived L_z are compared to previously reported values in the MASL and the accuracy of TRIF to properly emulate MAPS fluctuations is evaluated.

Optimized solutions of L_z are generally in good agreement with previously reported values in the MASL (Emes et al., 2019), where 94% of L_z solutions fall within a range observed in (Emes et al., 2019) over a wide range of atmospheric stability conditions. Two L_z are greater than the reported ranges where these L_z occur during near thermally neutral conditions, likely causing underestimation of bulk C_n^2, as previously reported (Frederickson

et al., 2000). Furthermore, for periods of thermal stability, NAVSLaM has been shown to overestimate bulk C_n^2 contributing to possible underestimation in the derived L_z. These uncertainties in C_n^2 can explain why the L_z estimates are within the correct order of magnitude but may not follow expected trends with air-sea temperature difference (ASTD).

Fluctuations from the TRIF optimization to MAPS measurements are further examined by highlighting the relationship between Ω_{Fit} and variations in MAPS fluctuations as a function of altitude. Specifically, when the assumption of C_n^2 homogeneity degrades Ω_{Fit} increases. Vertical heterogeneity is observed, to some degree, for all MAPS deployments further suggesting the physical nature of the MAPS fluctuations. Even in cases where vertical heterogeneity is more prominent, and Ω_{Fit} is relatively large, TRIF refractive fluctuations are generally in good agreement with the MAPS refractivity. This result illuminates the effectiveness of the TRIF model to emulate refractive fluctuations over a variety of conditions. Thus, the authors suggest variability observed in MAPS measured instantaneous refractivity are physically significant and are not primarily influenced by measurement uncertainty. Future research should incorporate turbulent refractive index fluctuation models that account for vertically heterogenous C_n^2.

Table 6.1. Overview of MAPS datasets. Deployment number, time, duration, number of launches, number of samples, and root mean squared (RMS) fluctuation of the MAPS measurements over each deployment are shown. Also included are the NAVSLaM estimated refractive index structure constant (C_n^2), optimized vertical outer length scale (L_z), and corresponding fitness score (Ω_{Fit}), defined in (6.10), evaluated for each optimization.

MAPS Dataset	Deployment Time (EST)	Duration (min.)	Launches	Samples	M' RMS (M-units)	NAVSLaM C_n^2 ($m^{-2/3}$)	Derived L_z (m)	Ω_{FIT} (M-units^2)
1	13-Oct 12:49	22	7	1572	1.092	4.75E-13	4.69	0.010
2	13-Oct 15:47	25	7	1264	1.021	4.96E-13	4.24	0.001
3	14-Oct 09:06	19	5	698	1.471	4.66E-13	5.89	0.035
4	14-Oct 12:42	38	7	867	1.742	3.22E-13	8.09	0.022
5*	14-Oct 15:32	17	6	684	1.442	8.34E-13	4.51	0.022
6*	15-Oct 08:22	9	7	936	1.799	1.35E-12	4.58	0.095
7	15-Oct 11:03	54	6	981	1.835	1.17E-12	4.74	0.081
8	15-Oct 14:41	30	6	737	1.350	1.01E-12	4.08	0.019
9	16-Oct 09:12	44	2	364	1.580	1.73E-12	3.81	0.009
10	16-Oct 12:16	20	6	1077	1.664	1.79E-12	3.70	0.024
11	16-Oct 14:38	32	7	1134	2.186	1.27E-12	5.51	0.036
12	17-Oct 08:07	22	9	945	1.216	1.48E-12	3.19	0.035
13	17-Oct 11:04	14	7	1250	1.837	1.09E-12	5.01	0.091
14	17-Oct 14:06	16	7	873	1.481	1.23E-12	3.91	0.034
15*	17-Oct 18:25	35	3	295	1.164	9.47E-13	3.58	0.092
16*	20-Oct 09:41	32	20	2643	1.427	7.06E-13	4.93	0.016
17	20-Oct 12:57	23	10	1585	1.968	7.56E-13	5.87	0.060
18*	20-Oct 15:29	45	15	2287	1.749	6.74E-13	5.70	0.020
19	21-Oct 07:01	41	7	969	1.605	1.95E-13	9.42	0.125
20	21-Oct 08:57	34	8	859	1.116	2.20E-13	6.42	0.059
21*	21-Oct 10:29	17	7	619	1.094	5.30E-13	4.73	0.010
22	21-Oct 12:10	42	7	695	1.252	3.09E-13	5.85	0.030
23	23-Oct 08:43	22	14	1837	1.991	1.67E-13	11.80	0.021
24	23-Oct 11:44	18	9	1457	2.253	1.66E-13	13.57	0.061
25	24-Oct 08:05	31	6	920	2.290	1.80E-12	4.85	0.086
26	25-Oct 11:25	30	16	2072	1.870	4.43E-13	7.59	0.011
27	25-Oct 14:11	25	14	1892	1.190	2.98E-14	17.02	0.002
28	25-Oct 15:58	24	8	1187	0.955	3.44E-13	4.68	0.005
29*	25-Oct 18:28	37	6	748	0.749	3.99E-13	3.98	0.010
30*	31-Oct 17:19	25	8	799	0.958	9.96E-13	2.96	0.007
31	31-Oct 18:15	30	7	850	1.838	1.09E-12	4.85	0.072
32	01-Oct 08:31	21	10	1533	2.770	1.98E-12	5.38	0.127
33	01-Oct 10:57	19	10	1570	3.076	1.36E-12	7.07	0.260
34	01-Oct 13:30	28	8	1306	2.601	2.52E-12	4.75	0.065
35	01-Oct 15:39	19	7	1226	2.390	2.16E-12	4.78	0.019
36	01-Oct 17:32	11	12	967	1.183	1.64E-12	3.02	0.002

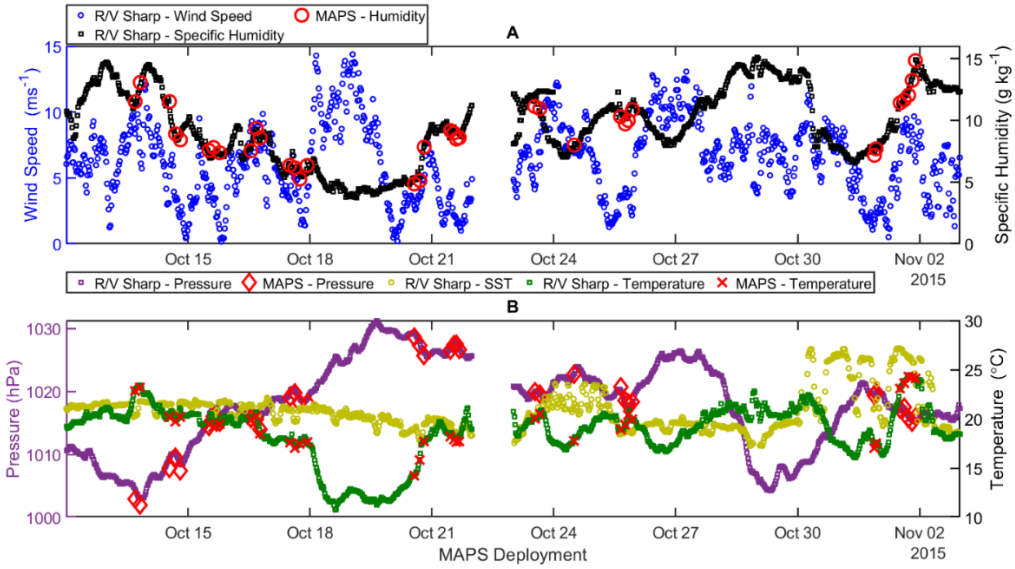

Figure 6.1. Time series of wind speed and sea surface temperature (SST) measured aboard the R/V Sharp, and pressure, air temperature, and specific humidity from the 7th order polynomial fit of the MAPS data. All meteorological parameters are measured at an altitude of 12 m above mean sea level and are displayed for all MAPS deployment times during the CASPER-East field campaign (Table 6.1).

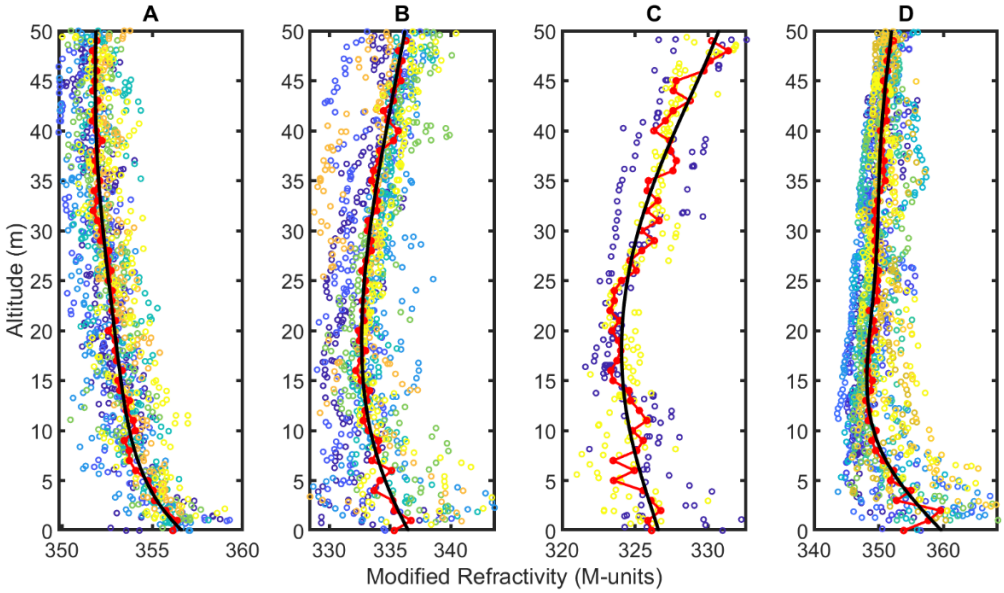

Figure 6.2. Example MAPS datasets corresponding to deployments 2 (A), 11 (B), 9 (C), and 33 (D) (Table 6.1). Circles represent the modified refractivity computed via (6.1) from the instantaneous measurements obtained from MAPS, where the black line is the 7th order polynomial fit representing the mean refractivity profile, and the red line represents a 1 m bin-averaged profile. Colors included for the instantaneous refractivity measurements correspond to different launches (single ascent and descent) of MAPS.

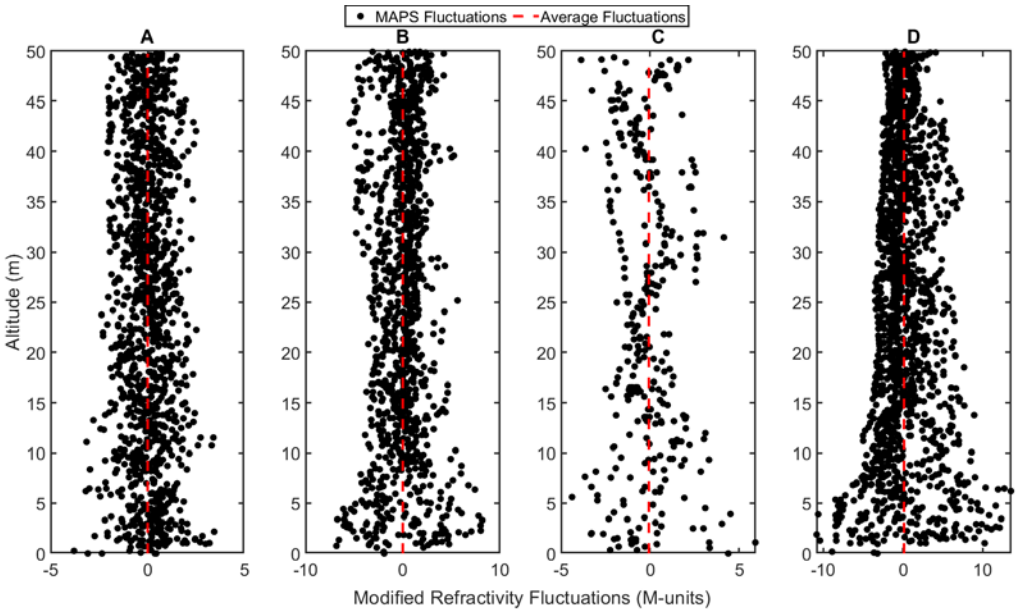

Figure 6.3. Fluctuations ($M'(z)$) computed via (6.2) corresponding to the MAPS datasets in Figure 6.2. The red dashed line shows the mean of the fluctuations verifying the 7th order polynomial fit as a good measure of the mean.

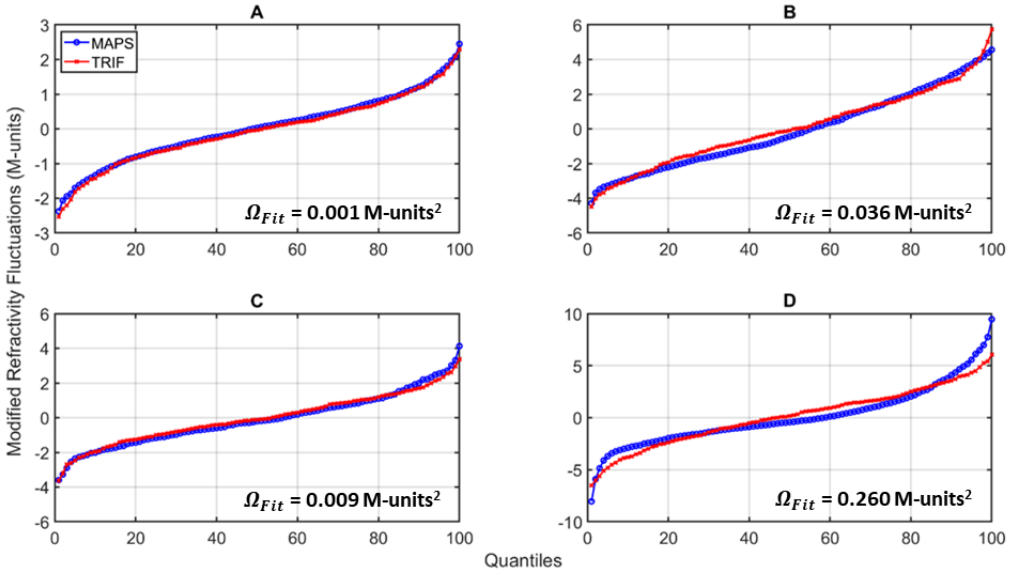

Figure 6.4. Quantiles estimated corresponding to the example MAPS fluctuations illustrated in Figure 6.3 and associated TRIF model fluctuation predictions realized via particle swarm optimization of L_z. An array of optimization results are displayed in this figure: the dataset with (A) the lowest fitness score, (B) fitness score nearest to the mean over all optimizations, (C) MAPS dataset with the fewest measurements (dataset 2), and (D) the largest fitness score. Fitness scores (Ω_{Fit}) for each example are included in each subplot.

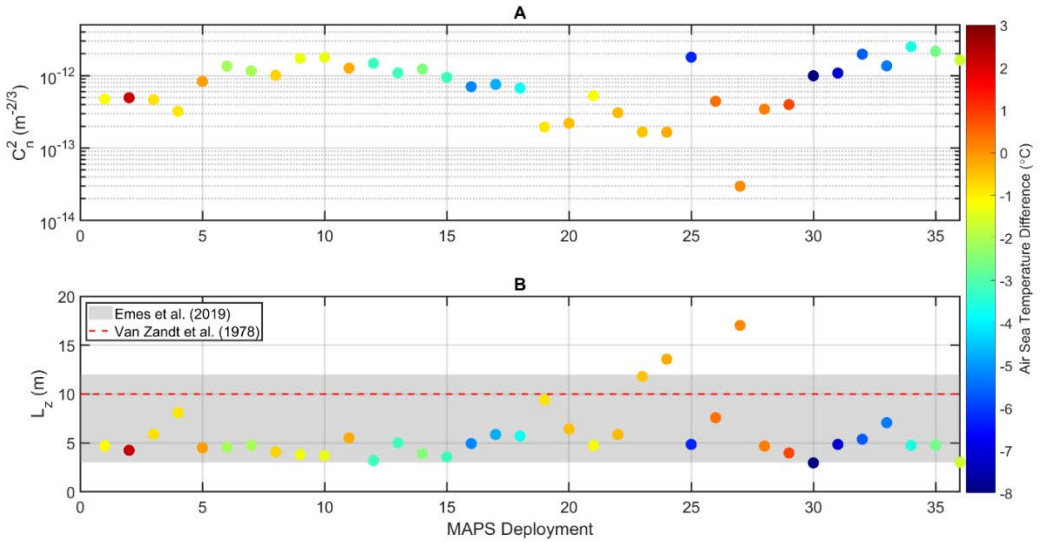

Figure 6.5. (A) Refractive index structure constant (C_n^2) estimated via NAVSLaM from the environmental variables displayed in Figure 6.1 for each MAPS deployment. (B) L_z solutions from the particle swarm optimization corresponding to each MAPS deployment. Included in (B) are previously reported ranges of L_z in the atmospheric surface layer (at ~12 m above the boundary) from Emes et al. (2019) for differing atmospheric stability regimes and L_z reported in VanZandt et al. (1978) for the free atmosphere (10 m).

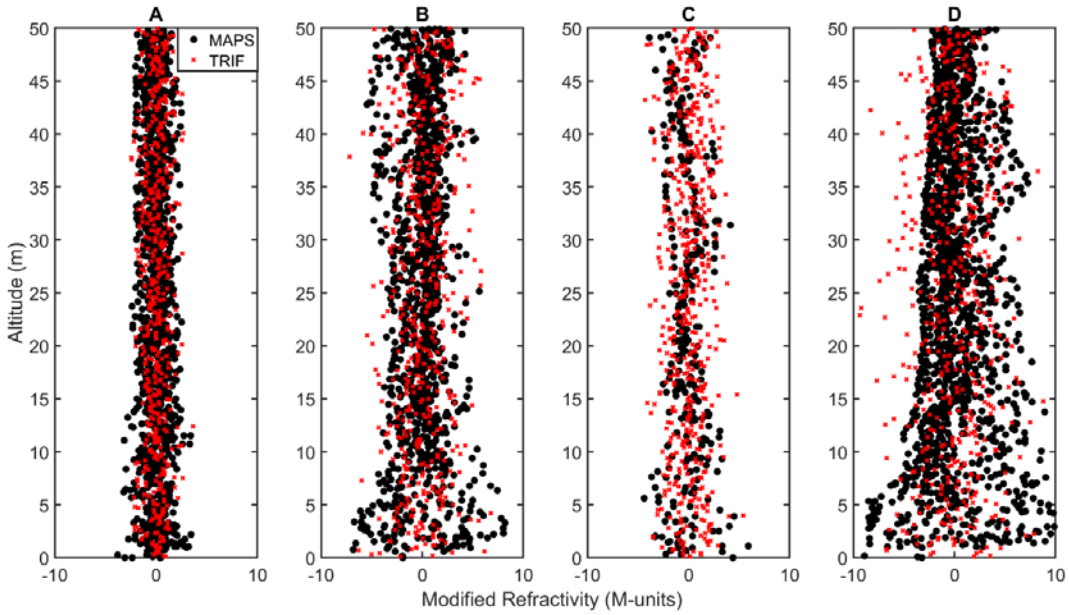

Figure 6.6. Refractive index fluctuations corresponding to example MAPS deployments in Figures 6.1, 6.2, 6.3, and 6.4 with the resultant TRIF model fluctuation realized via particle swarm optimization.

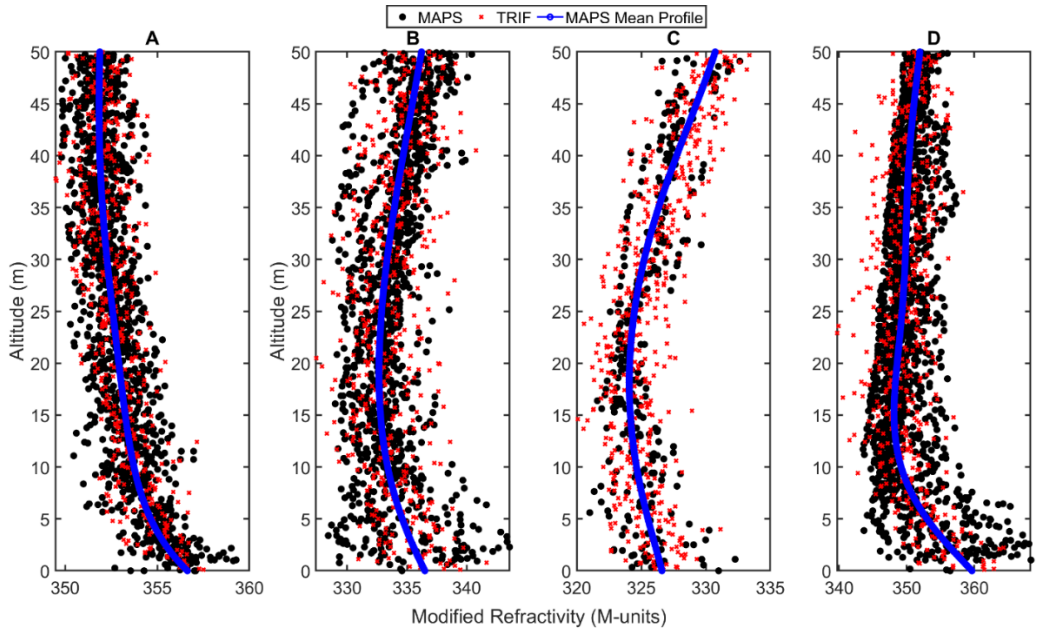

Figure 6.7. MAPS and TRIF instantaneous refractivity and the corresponding MAPS 7th order polynomial fit for the MAPS deployments previously described in Figure 6.6.

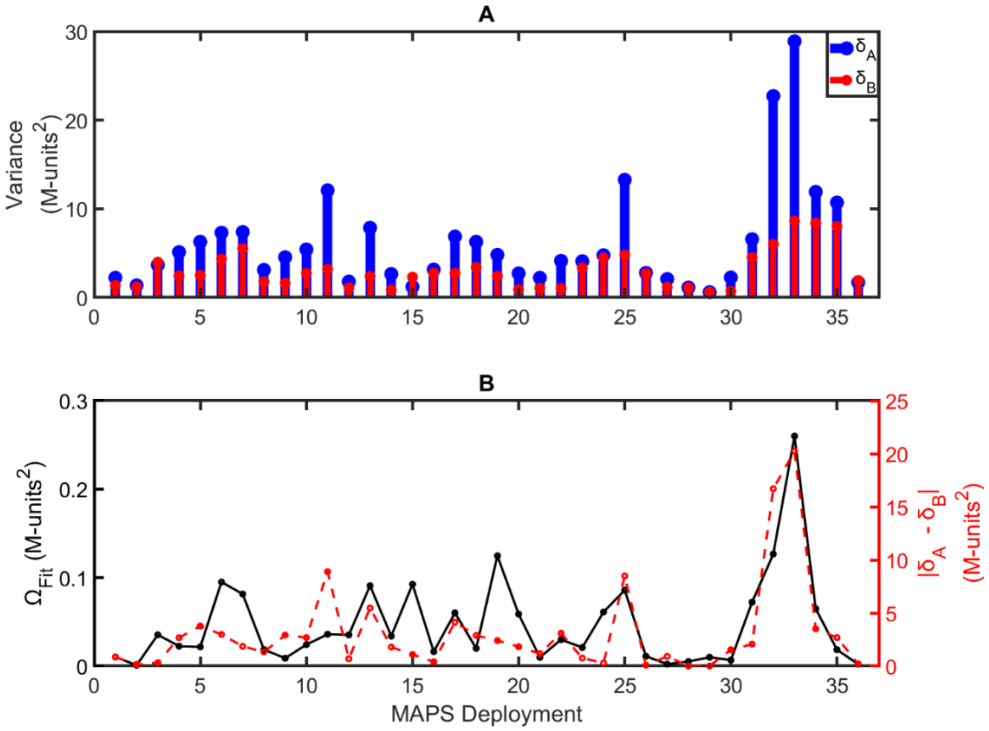

Figure 6.8. (A) Altitudinal variance of MAPS refractive fluctuations (M') displayed for altitudes spanning 0 – 10 m and 10 – 20 m, δ_A and δ_B respectively. (B) the left axis illustrates fitness scores (6.10) corresponding to the MAPS/TRIF optimization experiments outlined in Table 6.1. The magnitude of difference in MAPS refractive fluctuation variance between the 0 – 10 m and 10 – 20 m altitudinal bins ($|\delta_A - \delta_B|$) is illustrated on the right-hand axis.

Chapter 7

Relative Influence of Sea State and Mean, Turbulent, and Heterogenous Refractivity on X-Band Propagation[4]

Nomenclature	Definition
BGH	Beyond the Geometric Horizon
c_0	Potential Refractivity Gradient
C_n^2	Refractive Index Structure Constant
CPS	Correlated Phase Screen
dB	Decibel
EDH	Evaporation Duct Height
eFAST	Extended Fourier Amplitude Sensitivity Test
EM	Electromagnetic
GHz	Gigahertz
L_z	Vertical Outer Length Scale
L	Monin Obukhov Length Scale
m_1	Mixed Layer Slope
MASL	Marine Atmospheric Surface Layer
MPS	Multiple Phase-Screen
NAS	Normalized Average Sensitivity Index
NRAS	Regionally Averaged Normalized Sensitivity Index
NS_{TI}	Normalized Total Order Sensitivity Index

[4] This chapter is based on the submitted manuscript listed below:
Pastore, D. M., & Hackett, E. E. (2023). Relative Influence of Sea State and Mean, Turbulent, and Heterogenous Refractivity on X-Band Propagation. IEEE Transactions on Antennas and Propagation.

Nomenclature	Definition
OAT	One-At-A-Time
P_L	Propagation Loss
PWE	Parabolic Wave Equation
PWE	Parabolic Wave Equation
s_d	EDH Slope Over Range
S_H	Swell Height
S_I	First-Order Sensitivity Index
S_{TI}	Total Sensitivity Index
$\overline{U}$	Wind Speed
$\overline{z_d}$	Mean Duct Height
z/L	Stability parameter
λ	Swell Wavelength

7.1 Chapter Introduction

Discrepancies between predicted and measured propagation, when considering only mean refractivity, could be due in-part to turbulent fluctuations of the refractive index (Chapter 6), spatially heterogenous evaporative ducting environments, and mischaracterization of the rough ocean bottom boundary. To better understand the relative importance of these contributors, this chapter addresses objective (iv) (Chapter 3) investigating the sensitivity of X-band propagation to parameters describing sea-state conditions and refractive environments, including turbulent fluctuations and spatially heterogenous conditions. The extended Fourier Amplitude Sensitivity Test is employed to compute sensitivity indices that evaluate the leading-order effects and effects due to non-linear interactions between these refractive and sea state parameters on a parabolic wave equation electromagnetic propagation simulation. The parameters are delineated and

evaluated in three atmospheric stability regime experiments: stable, neutral, and unstable, and consider both trapping and non-trapping propagation conditions. Parameter sensitivity indices are ranked for each experiment to examine the relative influence of the parameters on X-band propagation predictions.

7.2 Methods

7.2.1 Extended Fourier Amplitude Sensitivity Test

The extended Fourier Amplitude Sensitivity Test (eFAST) is a global sensitivity technique that utilizes variance decomposition to determine the sensitivity of a model to a set of input parameters. eFAST is useful for examining non-linear non-additive models in a computationally efficient manner (Saltelli et al., 1999; Marino et al., 2008). The main benefit of eFAST, relative to other sensitivity techniques, is the computation of both first order sensitivity index (S_I) and total sensitivity index (S_{TI}) of the specified model; inclusion of S_{TI} accounts for interactive effects between parameters on model variance. For this study, eFAST is deemed appropriate due to the complexity of the PWE simulation and its implementation in a prior propagation study (Lentini and Hackett, 2015). A brief description of the eFAST technique will be discussed where a more comprehensive description can be found in Marino et al. (2008), Xu and Gertner (2013), and Lentini and Hackett (2015).

For eFAST, model input parameters are varied based on a sampling scheme utilizing an incommensurate frequency (ω_i) unique to each parameter, X_i. As such, using a transformation function, all parameters are varied simultaneously through a single search variable, *s* (Saltelli et al., 1999, Lentini and Hackett, 2015):

$$X_i(s) = \mathrm{G}(\sin \omega_i s) = \frac{1}{2} + \frac{1}{\pi}\arcsin(\sin \omega_i s + \varphi_i)\,, \quad -\pi \le s \le \pi \tag{7.1}$$

where φ_i is a random phase shift accommodating a starting point anywhere within the search curve (Saltelli et al., 1999). The transformation function employed in (7.1) generates a uniform sampling distribution for each parameter, X_i. This transformation function allows the entire parameter space to be explored by varying one parameter, s, making it computationally efficient. The inclusion of other transformation functions is possible (e.g., Gaussian), but for this study it seems appropriate to explore all parameter search spaces evenly as some variables could be best described by a Gaussian distribution while others a uniform distribution. This transformation function is also the same as that used in Lentini and Hackett (2015).

After model simulations are completed for all eFAST model input parameter combinations determined from (7.1), eFAST method decomposes model output variance into partial variance associated with each parameter (V_i), and partial variance of the complimentary set of each parameter (V_{-i}) computed (Marino et al., 2008; Lentini and Hackett, 2015):

$$V = \frac{1}{N_s}\sum_{r=1}^{N_s} Y_r^2 \tag{7.2}$$

$$V_i = 2\sum_{j=1}^{M_H} A_{j\omega_i}^2 + B_{j\omega_i}^2 \tag{7.3}$$

where Y_r is the amplitude of the oscillations of the model output (in this case PWE simulated propagation loss) at each frequency, N_S is the number of samples in s, and M_H is the number of included harmonics (here, M_H=4). A and B are the Fourier coefficients at

each harmonic j for each incommensurate frequency (w_i) calculated as (Ekstrom, 2005; Lentini and Hackett, 2015):

$$A_j = \frac{1}{N_S}\left\{ Y_0 + \sum_{r=1}^{\frac{N_S-1}{2}} (Y_r + Y_{-r}) \cos\frac{\pi j r}{N_S} \right\}, \quad j \text{ even} = 0, j \text{ odd} \tag{7.4}$$

$$B_j = \frac{1}{N_S}\left\{ Y_0 + \sum_{r=1}^{\frac{N_S-1}{2}} (Y_r - Y_{-r}) \sin\frac{\pi j r}{N_S} \right\}, \quad j \text{ odd} = 0, j \text{ even} \tag{7.5}$$

From the variances computed in (7.2) and (7.3) the sensitivity indexes S_{TI} and S_I for each parameter (X_i) can be computed as (Lentini and Hackett, 2015):

$$S_{I_i} = \frac{V_i}{V} \tag{7.6}$$

$$S_{TI_i} = 1 - \frac{V_{-i}}{V} \tag{7.7}$$

where -*i* indicates the complimentary set (all parameters except parameter *i*).

Equation (7.6) computes the first-order sensitivity, which represents the amount of variance in the model output explained by that one parameter and would be equivalent to what one would obtain using an OAT approach. Further, (7.7) computes the total order sensitivity, which accounts for the higher-order effects associated with interactions between this parameter and the other parameters, and their combined effect on model output variations.

Aliasing can occur without proper sampling of the search space by the search variable, *s*. Mitigation of this sampling error is achieved through a sampling scheme that accounts for the number of parameters and harmonics used in calculation of the partial variances. This sampling scheme is common practice in eFAST analyses (Saltelli et al.,

1999; Marino et al., 2008; Lentini and Hackett, 2015) and requires that at least 65 model runs per included parameter are performed. A dummy parameter is also included in the set of eFAST input parameters, which varies independently of the model output. The dummy's estimated sensitivity indices (S_{TI} and S_I) are assumed to represent random variance within the model and are used to interpret significance level of sensitivity indices of the other parameters. Sensitivity indices less than or equal to the dummy are considered not significantly different than zero (Marino et al., 2008), and therefore, unimportant to the model.

For this study, eFAST will be used to determine the sensitivity of an EM propagation simulation to the propagation environment. The environment is broken into two categories, the sea surface and the refractivity. The following subsections explain the models used to describe the refractivity and sea surface, where specific parameters of each model are the eFAST input parameters (X_i) that are varied to investigate their relative effects on EM propagation predictions.

7.2.2 Atmospheric Refractivity Model

The atmospheric refractivity model is comprised of three components: i) a parametric refractivity model describing "mean" atmospheric refractivity, ii) an EDH heterogeneity model accounting for range variation of EDH, and iii) a stochastic refractive index fluctuation model emulating turbulent fluctuations of the refractive index. To the authors' knowledge, this is the first time a refractivity model has included aspects of mean refractivity, turbulence, and spatial heterogeneity to comprehensively describe the atmospheric refractivity within a PWE simulation. The individual model components of refractivity are further discussed below.

Mean refractivity is modeled via a parametric refractivity model (Gerstoft et al., 2003; Saeger et al., 2015; Penton and Hackett, 2018; Matsko and Hackett, 2019, Pastore et al., 2022):

$$\bar{M}(r,z) = M_0 + \begin{cases} c_0\left(z - z_d(r)\ln\left(\frac{z+0.00015}{0.00015}\right)\right) & , z \le z_L \\ m_1 z - M_1 & , z > z_L \end{cases} \tag{7.8}$$

where $M_0 = 333$ M-units representing surface refractivity, $z_d(r)$ is evaporation duct height as a function of range (r), m_1 is mixed layer slope, and M_1 is a term defined by c_0, z_d, and m_1 ensuring a continuous profile between layers. The potential refractivity gradient (Paulus, 1990), c_0, allows modification of the shape of the refractivity profile within the evaporation layer for a specified duct height (Saeger et al., 2015; Penton and Hackett, 2018, Pastore et al., 2022). The evaporation layer extends from the surface to $z_L \equiv 2z_d$. M_0 is held constant throughout this study because the propagation is influenced by the refractivity gradients and not the absolute values.

Incorporation of EDH heterogeneity over range is included within (7.8) via a linear variation of z_d:

$$z_d(r) = s_d r + \frac{\bar{z_d}}{2} \tag{7.9}$$

where, s_d is EDH slope, and $\bar{z_d}$ is the mean EDH over the range transect of duct heights modeled in (7.9). Application of $z_d(r)$ to (7.8) makes modified refractivity a function of both height and range, $\bar{M}(r,z)$, and creates a set of modified refractivity profiles describing a single transect of a spatially varying mean refractive environment. A linear function to describe variation of z_d in range was chosen for multiple reasons. First, range heterogeneity of refractivity is not yet well understood and can be characterized by a variety of n^{th} degree polynomial functions, where linear functions are dominant in weather model forecasts

(Greenway, 2020; Greenway et al., 2023). And second, few studies account for variation of z_d in range (Zhou et al., 2017) but it is known that range variations can have non-negligible effects on EM propagation (Goldhirsh and Dockery, 1998). Further, no knowledge exists describing critical refractive gradient and mixed layer slope variation in range, thus, a simplistic linear model, varying only z_d and assuming c_0 and m_1 to be constant over range, is appropriate and practical. Within the eFAST methodology, c_0 and m_1 from (7.8) as well as $\bar{z_d}$ and s_d from (7.9) are varied to determine S_I and S_{TI} of the propagation model for each of these parameters.

In addition to mean and spatially heterogenous components of refractivity, refractivity is assumed to be constantly perturbed by continuous fluctuations due to turbulence within the atmosphere, following the refractive index turbulence model verified in Chapter 6. Modeling of the random fluctuations is achieved by the decomposition of refractivity (Wagner et al., 2016):

$$M(r,z) = \bar{M}(r,z) + M'(r,z) \tag{7.10}$$

where $\bar{M}(r,z)$ is a mean refractivity vertical profile and $M'(r,z)$ is the random fluctuations considered to be stochastic. For this formulation, it is assumed perturbations do not change in time while EM waves propagate through the medium, which is a reasonable assumption given EM waves travel at the speed of light (far faster than even the shortest turbulent time scale). The stochastic fluctuating component is described by the 2-D Kolmogorov spectrum (Ishimaru, 1997; Chou and Kiang, 2014):

$$\emptyset(\kappa_r,\kappa_z) = \frac{0.0555C_n^2}{(\kappa_r^2+\kappa_z^2+1/L_0^2)^{4/3}} \tag{7.11}$$

where κ is the spatial wavenumber (where subscript indicates directional component), C_n^2 is the refractive index structure constant (with units of $m^{-2/3}$), and L_0 is the outer length

scale delineating the border between energy containing or "mixing" scales from those in the inertial subrange, with units of meters. To account for anisotropy in the MASL, the 2-D Kolmogorov spectrum from (7.11) can be modified (Ishimaru, 1997; Chou and Kiang, 2014):

$$\emptyset(\kappa_r, \kappa_z) = \frac{0.0555 C_n^2 (L_r L_z)^{\frac{4}{3}}}{(\kappa_r^2 L_r^2 + \kappa_z^2 L_z^2 + 1)^{\frac{4}{3}}} \tag{7.12}$$

where L_z and L_r are the vertical and horizontal outer length scales, respectively. The relationship between these outer length scales has been previously studied and will be represented in this study as L_z/L_r = 0.27 (Emes et al., 2019). Within the eFAST analysis, C_n^2 and L_z from (7.12) are included to explore the effects of refractive index turbulent fluctuations on EM propagation. They are assumed to be homogenous in both range and altitude.

7.2.3 Ocean Wave Model

The bottom boundary for the propagation domain is constructed via an ocean wavenumber spectral model. Specifically, a Donelan-Peirson-Banner model accounts for the wind seas and capillary waves (Pierson and Moskowitz, 1964; Donelan et al., 1985; Banner et al., 1989), which is appended with an independent narrow banded Gaussian swell spectrum (Ryan 1991); for brevity the wave model will be referred to as $\emptyset_W$. $\emptyset_W$ is parameterized by the mean wind speed at z = 10 m (U), the swell height (S_H) and swell wavelength (λ). These sea surface characteristics represent parameters describing the shorter (wind seas) and longer (swell) length scales of the rough ocean surface. In this study, the wind wave fields are considered fully developed. Within the eFAST analysis, U, S_H, and λ are varied to explore the sensitivity of X-band propagation to sea state characteristics.

It is important to note, the ocean wave model and the atmospheric refractivity model are not coupled. Thus, certain combinations of the respective model parameters could diverge from physically plausible conditions; this issue is mitigated as much as possible by dividing the sensitivity analysis into several experiments that vary the range of the parameters explored in the eFAST analysis (see section 7.3)

7.2.4 Propagation Simulation

EM propagation predictions are performed utilizing the Variable Terrain Radio-Wave Parabolic Equation (VTRPE) simulation (Ryan, 1991). VTRPE is employed in this study because the simulation can model a variety of environmental conditions and it has been used in prior similar studies (Lentini and Hackett, 2015; Penton and Hackett; 2018; Matsko and Hackett, 2019; Pastore et al., 2021; Pastore et al., 2022). A split step rotated Green's function parabolic equation is used to compute the full wave solution of the EM field (Ryan, 1991, Sirkova, 2012). For this study, like Lentini and Hackett (2015), propagation loss (PL), in dB, are used as the simulation output for the eFAST experiments. PL is defined as:

$$P_L = 20\log(2k_0 r) - 20\log|F| \tag{7.13}$$

where k_0 defines wavenumber of the electromagnetic wave, and F is the propagation factor:

$$F = \left|\frac{\boldsymbol{E}}{\boldsymbol{E_0}}\right| \tag{7.14}$$

where $\boldsymbol{E_0}$ is the electric field in free space and $\boldsymbol{E}$ is the electric field in the modeled environment.

Application of the refractivity model within the propagation simulation is not a trivial process due to the refractive index turbulent fluctuations and range inhomogeneity;

associated challenges are described in multiple previous studies (Rouseff, 1992; Chou et al., 2014; Wagner et al., 2016; Mukherjee and Yardim, 2021). Commonly, stochastic variations in the refractive index are performed via the multiple phase-screen (MPS) method, where the EM field is propagated through successive refractive profile realizations. The MPS method employs the Markov approximation, or the assumption that the phase screens are δ-correlated over propagation space (Charnotski, 2016), this assumption is valid only when the phase-screen spatial resolution (Δr) is approximately (Knepp, 1983; Mukherjee and Yardim, 2021):

$$\Delta r \geq 5L_r \tag{7.15}$$

Consideration of (7.15) in the implementation of the MPS-method is imperative for the physically practical implementation of stochastic turbulence within the PWE, and thus reducing error in the computation of the EM wave field.

EM wave field solution error for a given frequency, independent of stochastic variation in the refractive index, is a function of the PWE solution range step-size. In this study, Δr = 0.3 m to accurately solve the EM wave field over a rough bottom boundary condition (Ryan, 1991) and satisfying the Δr necessary for a propagation frequency of 10.7 GHz and a maximum propagation angle of 6º, an angle shown to be appropriate for propagation through surface ducting conditions (Barrios et al., 2008; Wagner et al., 2016; Mukherjee et al., 2021).

Δr = 0.3 m minimizes error of the PWE solution but violates (7.15) as horizontal outer length scales are on the order of tens to hundreds of meters (Emes et al., 2019). This violation invalidates applicability of the MPS method in this study. To address this limitation, the correlated phase screen (CPS) technique proposed in Mukherjee and Yardim

(2021) is employed. The CPS method relieves the limitations of (7.15), allowing for closely spaced, and thus, correlated phase screens. These vertical phase screens are computed (Mukherjee and Yardim, 2021):

$$S_{\phi}(\kappa_r \kappa_z) = (\Delta r)^2 \emptyset(\kappa_r, \kappa_z) \left(\frac{\sin\left(\frac{\kappa_r \Delta r}{2}\right)}{\frac{k_r \Delta r}{2}} \right)^2 \tag{7.16}$$

Realizations of vertical phase screens obeying (7.16) are performed via convolution of S_{ϕ} and a zero mean 2-D Gaussian field. This process results in a field of modified refractivity fluctuations with sampling intervals of Δz = 0.01 m and Δr = 0.3 m that can be added to the duct height heterogeneous mean refractive profiles computed via (7.8) and (7.9). The resulting set of profiles, including heterogeneity and turbulence in the refractive index, are implemented within the PWE. It is important to note two limitations of the turbulence model: (i) the MAPS data used to verify the TRIF model (Chapter 6) contains influence from turbulence at all resolved scales whereas the TRIF model represents only inertial range turbulence, and (ii) the TRIF model does not account for all spatial correlations resulting from turbulence, such from coherent structures, due to the convolution of the Kolmogorov spectrum with the Gaussian field for generating fluctuation realizations. These TRIF model limitations could impact propagation predictions and thus eFAST sensitivity indices.

7.3 eFAST Experiments

For this study, propagation simulations are performed at a frequency of 10.7 GHz transmitted at an altitude of 15 m with vertical polarization and a Gaussian antenna pattern. The dielectric bottom boundary conditions are held constant with a sea surface temperature of 20 °C and a salinity of 35 ppt. Numerical experiments are performed for simulation

domains of 0-100 m in altitudeand 0 – 60 km in range, fully exploring the MASL including over the horizon propagation.

eFAST sensitivity experiments are performed for the parameters listed in Table 7.1. As discussed in §7.2.1, 65 model runs are needed for each parameter, so with ten parameters (Table 7.1), a total of 650 model runs were required for each sensitivity experiment. Atmospheric refractivity model parameters (§7.2.2) are varied separately for three different atmospheric stability conditions: stable, neutral, and unstable. Categorization of the atmosphere based on stability is defined via the stability parameter, $\left(\frac{z}{L}\right)$ (Panofsky and Dutton, 1984), where L is the Monin Obuhkov length scale (Foken, 2006). Stable regimes are defined as $0.5 \geq \frac{z}{L} > 0.01$, neutral as $-0.01 < \frac{z}{L} < 0.01$, and unstable regimes as $-5 < \frac{z}{L} \leq -0.01$ (Garratt, 1994). Specifically, C_n^2, L_Z, and C_0 have been shown to be stability dependent (Frederickson et al., 2000; Emes et al., 2019; Wessinger et al., 2022) and thus, their respective search spaces will vary between stability experiments, as outlined in Table 7.1. Search spaces are determined from the literature and are also supported by analysis of CASPER meteorological data (Frederickson, 2016; Wang et al., 2018; Pastore et al., 2022; Wessinger, 2022; Pastore et al., 2023; see Table 7.1). Other parameters included such as, EDH slope over range (s_d), mean EDH ($\overline{z_d}$), and m_1, have search spaces that are the same for each stability experiment due to a lack of consistent findings in the literature on the relationship between these parameters and atmospheric stability.

Along with experiments delineated by stability, each stability experiment is broken up into two scenarios, trapping and non-trapping. In this study, the trapping and non-trapping nomenclature specifically describes conditions where $\overline{z_d}$ is greater than the transmitter height (Tx; 16 m $\leq \overline{z_d} <$ 30 m) referred to as the trapping condition, and

conditions where $\overline{z_d}$ is less than the Tx (5 m < $\overline{z_d}$ ≤ 14 m), referred to as the non-trapping condition; application of this nomenclature does not define when trapping occurs, although it is more likely to occur under the respective name of each scenario. The trapping and non-trapping nomenclature is specific to $\overline{z_d}$, where duct height environments varying over range can breach the transmitter height (15 m) due to refractive conditions set by s_d. This breaching occurs in approximately 16% of simulation runs for each of the six experiments. Wave model (§7.2.3) parameters, specifically swell height (S_H) and wind speed (U) search spaces are based on the Beaufort scale encompassing force 0 ("calm") to force 7 ("near gale"). Swell wavelength (λ) search space encompasses a large range of wavelengths from coastal to open ocean swell. While feedback between atmospheric stability and sea state conditions exists, in this study, sea state parameter search spaces are not varied across the atmospheric stability regime experiments as this interaction is more complex than can be accounted for with the present models.

7.4 Results and Discussion

First order (S_I) and total order sensitivity indices (S_{TI}) are presented in subsections for each stability regime (stable, neutral, and unstable) experiment described in §7.3. Recall that the effect of the duct height crossing the transmitter height is largely omitted here due to the division of the experiments into trapping and non-trapping cases. The most significant factor to the propagation is well known to be whether a duct does or does not trap radiated energy (Turton et al., 1988; Craig and Levy, 1991; Cherrett, 2015; Pastore et al., 2021); thus, the results presented here are secondary to this mechanism for propagation variation, and sensitivities reported for $\overline{z_d}$ likely correspond primarily to variations in energy leakage by the duct.

Experiment results are presented as the average sensitivity index beyond the geometric horizon (BGH) normalized by the maximum average sensitivity index over all parameters, referred to as normalized average sensitivity index (NAS). This metric gives insight into the relative influence of each parameter on long-range propagation and allows for easier comparison between experiments. A NAS of one indicates the most influential parameter at a specific location and values below 1 indicate the relative importance of that parameter with respect to this most influential parameter.

Regionally averaged normalized sensitivity index (NRAS) is also presented for averages taken over three altitudinal regions, 2 – 10, 10 – 50, and 50 – 100 m. These results highlight locations of high/low sensitivity of radio-wave propagation within the modeled propagation domain for each of the parameters. The lowest region (2 – 10 m) excludes the lowest altitudes (1 – 2 m) to ensure effects of blockage (by sea surface waves) on averaged sensitivities are minimized (Benhmammouch et al., 2009). Furthermore, this region is capped at 10 m to capture variations in propagation well below the transmitter. The mid altitude region (10 – 50 m) encompasses a region that generally includes the transition of the refractive environment from super refractive (evaporation duct) to the mixed layer (sub-refractive) and encompasses the altitude of the transmitter. The upper altitudinal region (50 – 100 m) is delineated to capture the portion of the propagation domain explicitly within the mixed layer environment and well above the transmitter.

C_n^2, $\overline{z_d}$, and U are examined further as they tend to have the largest influence on propagation throughout this study, which has also been observed in previous studies of BGH propagation (Turton et al., 1988; Craig and Levy, 1991; Gerstoft et al., 2003; Freund et al., 2007; Chou and Kiang, 2014; Lentini and Hackett, 2015; Pastore et al., 2021).

Specifically, normalized total order sensitivity (NS_{TI}) is computed by normalizing each parameter's S_{TI} at each range and altitude of the propagation domain by the maximum S_{TI} across all parameters at that location. Thus, analogous to NAS, $NS_{TI} = 1$ indicates the most influential parameter at a specific location and values below 1 indicate the relative importance of that parameter with respect to this most influential parameter. Distributions of NS_{TI} for C_n^2, $\overline{z_d}$, and U over the propagation domain enable direct comparison of the relative role of turbulence, mean refractivity, and sea state in various regions of the modeled domain for X-band propagation.

7.4.1 Stable Regime

Normalized average S_I (NAS_I) and S_{TI} (NAS_{TI}) for trapping and non-trapping scenarios are illustrated in Figure 7.1. In this stable case, generally, mean refractive parameters within the duct (i.e., $\overline{z_d}$ and c_0) are shown to have the largest sensitivities within the atmospheric parameters, for both NAS_I and NAS_{TI} over trapping and non-trapping scenarios. These results are consistent with those reported in the sensitivity study of Lentini and Hackett (2015). This result suggests that while evaporation ducts may not always be present under stable conditions, when they do exist, their mean refractive characteristics tend to be the dominant factors in the propagation. The duct height is, of course, well-known to influence propagation and the c_0 parameter is similar to a measure of duct strength, which is also known to significantly impact propagation (Turton et al., 1988; Hitney and Vieth, 1990; Levy and Craig, 1990 Cherrett, 2015; Pastore et al., 2021). Recall, the duct height has the effect of the duct height crossing the transmitter removed, thus, the duct strength being more influential than duct height in some cases is logical.

In both the trapping and non-trapping cases, the sea surface is shown to be significantly influential relative to the mean refractivity characteristics. This result is expected as variations in wind-waves change multipath null locations and thus cause significant variations in the propagation loss at locations near the multipath nulls as sea state is varied (Penton and Hackett, 2018). NAS_{TI} for U is larger than that of swell wave height (S_H), while for NAS_I the opposite is true. This difference indicates that parameter interactions cause the influence of S_H to diminish relative to the influence of U. This result is consistent with the concept that EM propagation variations due to forward scattering are primarily driven by smaller-scale wind waves (less than ~50 m wavelength) rather than swell (wavelength much larger than 50 m).

Relative to the mean refractive and sea-surface conditions, turbulent fluctuations in the refractive index and duct height heterogeneity are shown to have a relatively negligible effect on propagation. During stable conditions, thermal stratification of the atmosphere is expected to dampen (mechanical and convective) turbulence in the MASL and thus fluctuations within the surface layer are small (Table 7.1) reducing their influence on EM waves. This result is reflected in Figure 7.1 by the small sensitivities for C_n^2 and L_Z. Like the turbulence, propagation sensitivity to evaporation duct height slope (s_d) is minimal relative to the other parameters.

Figure 7.2 shows $NRAS_{TI}$. For all altitudes, and consistent with the results shown in Figure 7.1, the mean refractivity parameters within the duct ($\overline{z_d}$ and c_0) and the wind speed are shown to be the most influential on propagation for both trapping scenarios; however, near the sea surface (2-10 m altitude range), the wind speed parameter emerges as the most influential parameter while at the other altitudes the mean refractivity

parameters are most dominant. It is also notable that swell plays a small role at higher altitudes (>10 m) but not as much at the lowest altitudes (<10 m) – indicating the influence of shifting multipath null locations on propagation variability at the higher altitudes.

In Figure 7.2, differences between $\mathrm{NRAS_{TI}}$ for trapping and non-trapping scenarios are apparent. To further explore these differences and visualize the regions of the domain where the relative roles of turbulence, mean refractivity, and sea state can be ranked, Figure 7.3 shows normalized S_{TI} ($\mathrm{NS_{TI}}$) for C_n^2, $\overline{z_d}$, and U (from top to bottom) in trapping (left column) and non-trapping (right column) scenarios; the dashed red line denotes the range of the geometric horizon for all altitudes. Visual differences between $\mathrm{NS_{TI}}$ for the trapping (Figure 7.3A, C, and E) and non-trapping (Figure 7.3B, D, and F) scenarios are noticeable.

The overall importance of $\overline{z_d}$ (Figure 7.3C and D) over the influence of C_n^2 (Figure 7.3A and B) and U (Figure 7.3E and F) is apparent when comparing along the columns of subfigures in Figure 7.3 for the trapping and, especially, the non-trapping scenario. In the trapping scenario, the sea state (U) plays a comparable role to that of the duct height.

In the trapping scenario, the low sensitivities of the duct height below the transmitter are due to the experiments being divided into the trapping and non-trapping scenarios. Variations in propagation due to the duct height crossing the transmitter height are not captured here intentionally so not to dominate the sensitivity results as this effect on propagation is well understood. Because all the propagation loss simulations have a "trapping" influence on the propagation for the trapping scenario, the duct height sensitivity is small there. The region just above the transmitter is influenced due to differences in leakage from the duct due to the proximity of the duct height to the transmitter height changing. In non-trapping scenarios, the duct height is the most

influential parameter in nearly the entire domain BGH and above the transmitter. Again, this region's sensitivity is presumably due to variations in propagation loss due to the duct height's proximity to the transmitter influencing this entire region for non-trapping scenarios. Similar results are discussed anecdotally in Pastore et al. (2021), but for unstable environments.

The sea state, through the wind speed, shows the low altitude propagation to be most significantly influenced by sea surface forward scatter that diminishes in importance with range in non-trapping scenarios but does not diminish in trapping scenarios. For trapping scenarios, the sea state is also observed to have an influence in the same region as the duct height, just above the transmitter, indicating a possible interaction between these parameters, potentially involving duct leakage, in trapping conditions. Large NS_{TI} is also observed for U near locations of multipath nulls, as expected. Turbulence (C_n^2) plays an insignificant role relative to mean refractivity and sea state evidenced by the low NS_{TI} for both trapping and non-trapping scenarios.

7.4.2 Neutral Regime

Neutral regime NAS_I and NAS_{TI} are illustrated in Figure 7.4, where similarly to the stable case, mean duct height and sea-surface parameters show the largest NAS_{TI}. A strong influence of duct height and sea surface characteristics in neutral regimes is supported in many prior studies (Turton 1988; Benhmammouch et al., 2009; Cherret, 2015; Lentini and Hackett, 2015). However, contrary to the stable case, there is more relative influence of turbulence and duct height heterogeneity on propagation, where the contributions to PL variations from these phenomena are roughly equal, especially for the trapping scenario

(Figure 7.4B). The role of duct strength (c_0) is also significantly smaller for the neutral case relative to the stable case.

In a neutral environment, the magnitude of C_n^2 is larger than a stable atmosphere (see Table 7.1), due to mechanical mixing no longer being inhibited by stable stratification, and consequently turbulent fluctuations of the refractive index are larger, causing more variation of the EM signal BGH. In fact, without parameter interactions, EM variations due to turbulence can cause large effects on propagation as evidenced by the highest NAS_I for C_n^2 in the non-trapping scenario.

The more constrained parameter range for duct curvature (see Table 7.1 – c_0) observed in neutral atmospheres likely diminishes the role of duct strength on the propagation in favor of duct height variations in range causing more significant changes in propagation. Thus, while duct height proximity to the transmitter and forward scatter of EM energy remains the primary mechanisms for variation in BGH propagation, turbulence and duct height heterogeneity start to become relevant to second-order variations in propagation for the neutral regime, and duct shape effects are less significant (and variable).

The regional analysis presented in Figure 7.5 (analogous to Figure 7.2), reveals similar results relative to the stable case. For all altitudes BGH, duct height ($\overline{z_d}$) and sea-state conditions (S_H and U) primarily vary EM propagation. At the lowest altitude bin (2-10 m) for trapping conditions, wind speed is the dominate source of propagation variation, while duct height dominates at altitudes above 10 m. For the non-trapping case, wind speed and duct height play nearly equal roles in propagation variability at all altitudes. Similar to

Figure 4, turbulence and duct height heterogeneity play a more significant role, relative to the stable case at all altitudes.

Figure 7.6 shows distributions of NS_{TI} for C_n^2, $\overline{z_d}$, and U for the two trapping scenarios for the neutral experiment. Again, similar to the stable case, the mean duct height is the most significant factor in most regions BGH for both trapping and non-trapping scenarios. The influence of the duct height for trapping scenarios is slightly more significant (larger NS_{TI} BGH) than that for the stable experiment. For both trapping and non-trapping scenarios, the influence of mean wind speed is largest below 10 m at all ranges.

Above 10 m, in the trapping scenario, the sea state and duct height contribute nearly equal roles to the propagation variability BGH; in contrast, for the non-trapping scenarios the duct height is most influential outside of areas near multipath nulls. Compared to the influence of sea state (wind speed) and mean duct height in propagation variability, the turbulence (C_n^2) is a relatively insignificant factor. Its most significant effects on propagation variability occur at around mid-altitudes (~25-75 m) at long range (> 50 km) – far from the transmitter, similar to results illustrated in Chou and Kiang (2014). This sensitivity is likely due to interactions between other, more significant factors like the duct height, and propagation variations due to cumulative effects of the turbulence over the long path length.

7.4.3 Unstable Regime

Unstable regime NAS_I and NAS_{TI} are presented in Figure 7.7. Unlike the neutral and stable experiments, for the unstable condition, turbulence, C_n^2 (Figure 7.7), dominates propagation variability BGH. Larger C_n^2 is associated with unstable atmospheric conditions

(see Table 7.1) due to convective processes combining with mechanical turbulence. The larger C_n^2 translates to increases in the fluctuation of the refractive index causing increased variations of EM energy throughout the propagation domain.

The mean duct height remains a significant factor as with the other two experiments. One may find it surprising that the duct height is not the most significant factor in this experiment but, recall the omission of the primary trapping effects of EDH in this study thus, these results indicate that the duct height remains important even after removing this aspect but is not as influential as the turbulence in its secondary effects (e.g., changes in duct leakage as the distance between the duct height and transmitter changes). The regional delineation of $NRAS_{TI}$ is presented in Figure 7.8. At the higher altitudes (10 – 100 m), C_n^2 is shown to be the dominant parameter in varying propagation, with all the remaining parameters having similarly important secondary effects. At the lowest altitudes (2-10 m), all parameters contribute in a nearly equal manner to propagation variability. The sea state plays a smaller relative role even at the lowest altitudes compared to the neutral and stable experiments. Duct height variability in range shows slightly lower $NRAS_{TI}$ at all altitudes relative to most of the other parameters, suggesting that spatial inhomogeneity is the least significant factor relative to the other phenomena examined (mean refractivity, sea state, and turbulence).

The mean mixed layer slope being important to propagation variability was also shown in the sensitivity study of Lentini and Hackett (2015). This (often) sub-refractive mixed layer likely increases propagation loss in the mid-altitudinal region as EM waves are deflected upward away from the duct.

These results are further delineated in Figure 7.9, where NS_{TI} is displayed for the entire propagation domain for C_n^2, $\overline{z_d}$, and U. The dominance of the turbulence (C_n^2) over the other two parameters in most of the domain is apparent and in stark contrast to the stable and neutral cases. However, at the lowest altitudes, C_n^2 is not as influential as the sea state, or EDH at long range for non-trapping conditions.

The sea state still dominates at the lowest altitudes but presumably due to the increased scatter from the turbulence, the multipath nulls are so washed out that the influence of the sea state even surrounding null positions is not present in the unstable experiment. The mean duct height secondary effects (i.e., after removing effects of trapping vs. non-trapping) are much less significant than in the stable and neutral cases with the duct height being of least consequence in the trapping scenario. This result indicates that if it is known that the duct height is above the transmitter, then the precision to which the duct height is known becomes less consequential for unstable atmospheres.

7.5 Summary and Conclusions

This study investigates and quantifies the relative importance of atmospheric and sea-surface conditions on EM propagation within the marine atmospheric surface layer. The extended Fourier Amplitude Sensitivity test is employed to quantify the global sensitivity of a set of parameters describing mean, turbulent fluctuations, and spatial heterogeneity of refractivity as well as swell and wind-wave characteristics of the sea-surface for X-band propagation. Parameter distributions are delineated over atmospheric stability regimes via the stability parameter (Panofsky and Dutton, 1984) for stable, neutral, and unstable atmospheric stabilities. Furthermore, sensitivity experiments for each regime are performed for trapping and non-trapping scenarios to more thoroughly explore how

parameters, outside of EDH, vary propagation predictions. This division largely removes the effect of the duct resulting in either trapping or non-trapping propagation so that this effect does not dominate the sensitivities as it is well known. Thus, here, sensitivities to the duct height are beyond this fundamental effect and explore the effects of the finer details of mean duct height variation on propagation (e.g., duct leakage) relative to other secondary effects.

Normalized first and total order sensitivity averaged beyond-the-geometric horizon are presented to understand variations in long range propagation, where normalized average total order sensitivity is further explored for three altitudinal regions. To illustrate the relative influence of turbulence, mean refractivity, and sea state as well as explore how the influence of these phenomena vary over the domain, especially BGH, normalized sensitivity over the simulation domain is presented for C_n^2, $\overline{z_d}$, and U – as representative of these components, respectively. Main results and conclusions are summarized in the following:

In stable regimes, mean duct height and curvature as well as the sea state are important drivers of propagation variability. The sea state plays a significant role near the surface (< 10m) and near locations of multipath nulls. The secondary effects of the duct height are significant and primarily influence the region just above the transmitter where effects of duct leakage will change as the proximity between the duct height and transmitter vary.

In neutral regimes, similar trends as the stable regime are observed except that turbulence and spatial inhomogeneity also tend to take on important secondary roles.

Notably, spatially heterogenous EDH causes the most influence on propagation in this regime relative to other stability regimes.

In unstable regimes, variability of propagation becomes significantly influenced by turbulence, which becomes the leading order effect outside of trapping vs. non-trapping conditions. The secondary effects from the duct height are much more limited in this experiment and the influence of the sea state is constrained to just the lowest 10 m, presumably due to the wash out of multipath nulls from the turbulence.

Table 7.1. Global sensitivity study atmospheric refractivity and sea-state parameter ranges and related citations for each atmospheric stability regime experiment.

Parameter Nomenclature	Parameter	Stable Regime		Neutral Regime		Unstable Regime		Citations
		Minimun	Maximum	Minimun	Maximum	Minimun	Maximum	
C_n^2	Structure Constant ($m^{-2/3}$)	$5x10^{-16}$	$5x10^{-13}$	$1x10^{-16}$	$1x10^{-12}$	$1x10^{-15}$	$5x10^{-12}$	Junwei et al. (2011); Qing et al. (2016); Wang et al. (2018)
L_z	Outer Length Scale (m)	1	3	3	6	6	8	Van Zandt et al. (1978); Emes et al. (2019)
s_d	Evaporation Duct Height Slope Over Range (m/km)	-5/60	5/60	-5/60	5/60	-5/60	5/60	Zhao et al. (2017); Wang et al. (2018)
$\overline{z_d}$	Mean Duct Height (m)	5	30	5	30	5	30	Skolnik (2001); Wang et al. (2018)
C_0	Duct Curvature (M-units/m)	0.025	0.2	0.115	0.135	0.2	0.45	Paulus (1990); Wang et al. (2018) ; Wessinger (2022)
m_1	Mixed Layer Slope (M-units/m)	0.08	0.12	0.08	0.12	0.08	0.12	Zhang et al. (2011); Wang et al. (2018)
U	Wind Speed (m/s)	0.1	17	0.1	17	0.1	17	Beaufort Scale (0-7)
S_H	Swell Height (m)	0.1	6	0.1	6	0.1	6	Generalized based on Beaufort Scale (0-7)
λ	Swell Wavelength (m)	50	250	50	250	50	250	Coastal swell to open sea swell

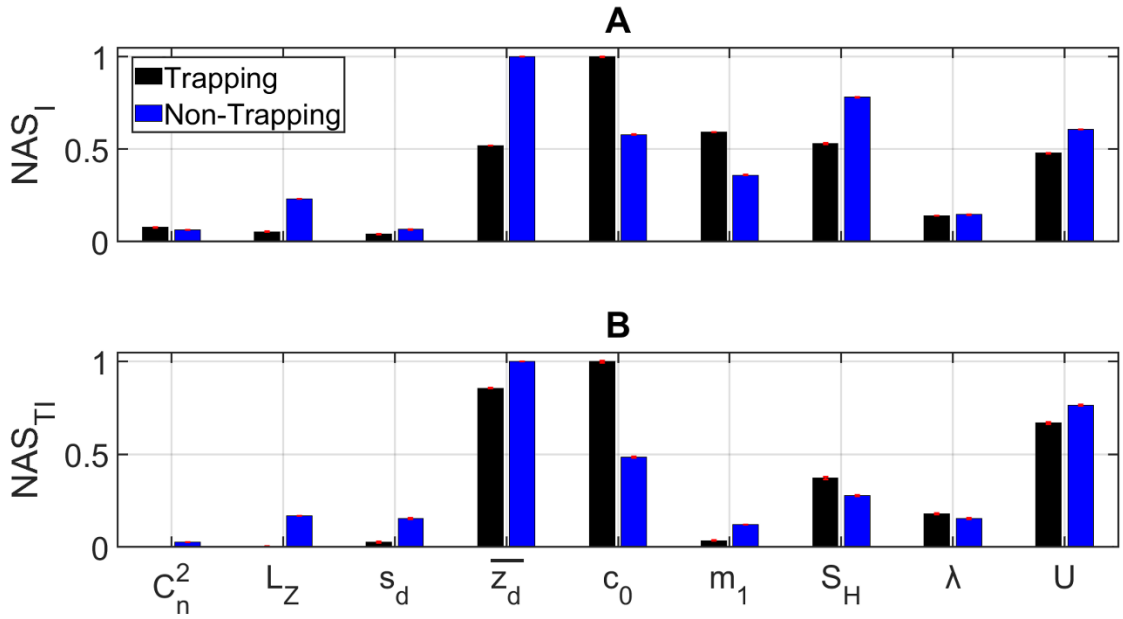

Figure 7.1. Stable regime (A) first-order (NAS_I) and (B) total-order (NAS_{TI}) normalized average sensitivity indices. Sensitivity indices for each parameter are averaged over ranges and altitudes beyond-the-geometric horizon and normalized by the maximum S_I and S_{TI}, respectively, for trapping (16 m $\leq \overline{z_d} <$ 30 m) and non-trapping (5 m $< \overline{z_d} \leq$ 14 m) scenarios. Red error-bars denote 99% confidence intervals.

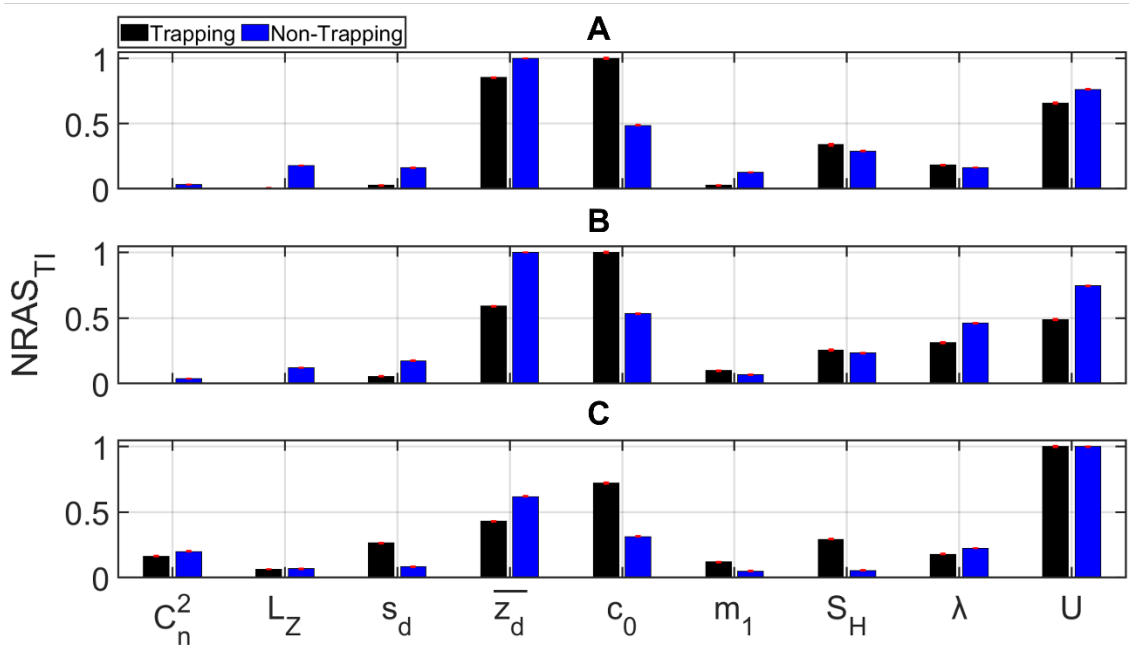

Figure 7.2. Stable regime regionally averaged total-order sensitivity ($NRAS_{TI}$), averaged over ranges beyond-the-geometric horizon and altitudes and of (A) 50 – 100 m, (B) 10 – 50 m, and (C) 2 – 10 m, normalized by the maximum S_{TI} over all parameters for trapping and non-trapping scenarios (NRAS). Red error-bars denote 99% confidence intervals.

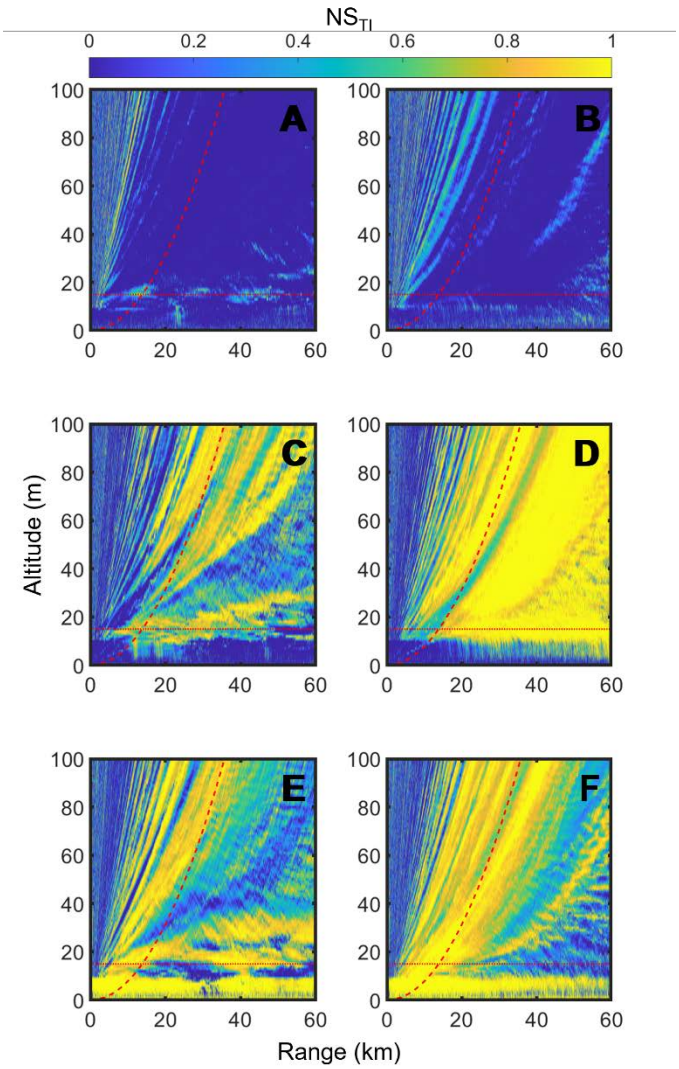

Figure 7.3. Stable regime total-order sensitivity (S_{TI}) normalized by the largest magnitude S_{TI} across all parameters, for each range and altitude. Normalized sensitivities (NS_{TI}) are shown for trapping (A, C, and E) and non-trapping (B, D, and F) scenarios; parameters illustrated are (A & B) C_n^2, (C & D) $\overline{z_d}$, and (E & F) U. These parameters are representative of the turbulence, mean atmospheric refractivity, and sea-state components, respectively. The dashed red line represents the geometric horizon, and the dotted horizontal red line represents the RF transmitter height (15 m).

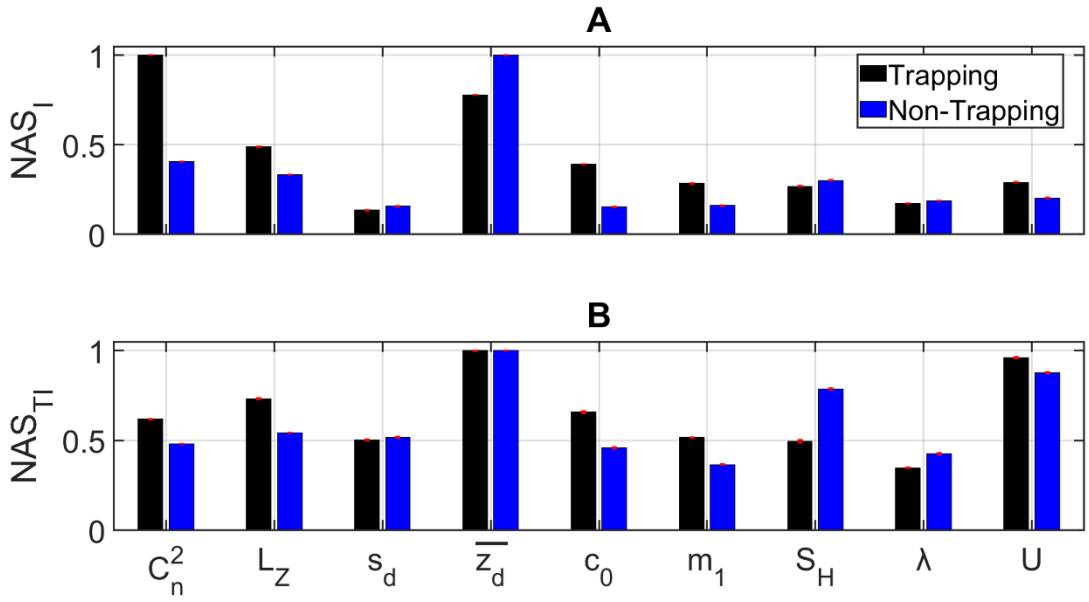

Figure 7.4. Neutral regime (A) first order (NAS_I) and (B) total-order (NAS_{TI}) sensitivity averaged over ranges and altitudes beyond-the-geometric horizon and normalized by the maximum S_I and S_{TI}, respectively, for trapping (16 m ≤ $\overline{z_d}$ < 30 m) and non-trapping (5 m < $\overline{z_d}$ ≤ 14 m) scenarios. Red error-bars denote 99% confidence intervals.

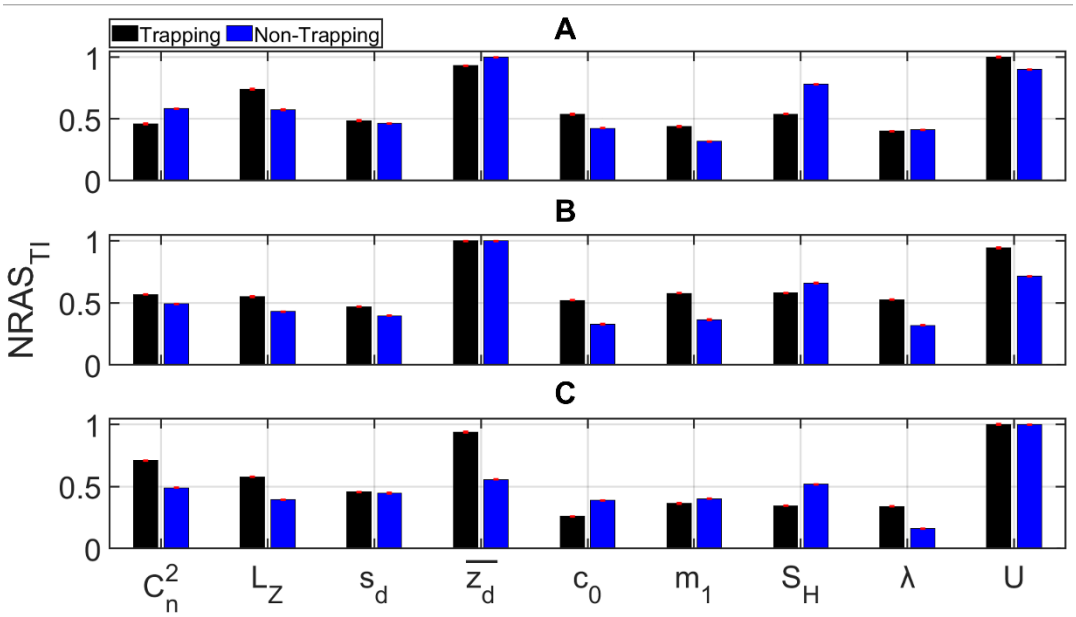

Figure 7.5. Neutral regime regionally averaged total-order sensitivity ($NRAS_{TI}$) averaged over ranges beyond-the-geometric horizon and altitudes of (A) 50 – 100 m, (B) 10 – 50 m, and (C) 2 – 10 m, normalized by the maximum S_{TI} over all parameters for trapping and non-trapping scenarios. Red error-bars denote 99% confidence intervals.

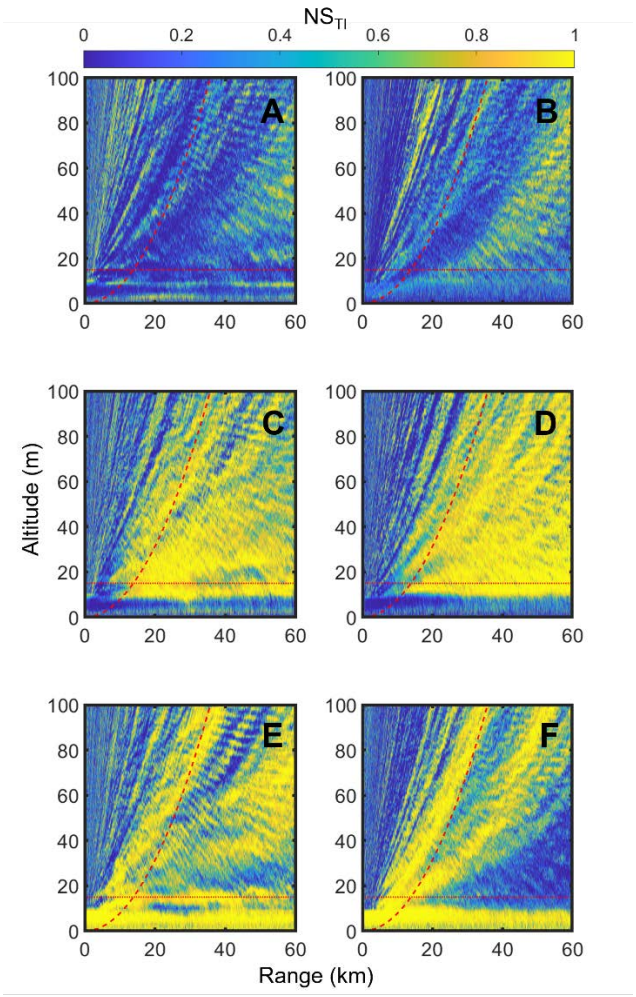

Figure 7.6. Neutral regime total-order sensitivity (S_{TI}) normalized by the largest magnitude S_{TI} over all parameters, at each range and altitude. Normalized sensitivities (NS_{TI}) are shown for trapping (A, C, and E) and non-trapping (B, D, and F) scenarios; parameters illustrated are (A & B) C_n^2, (C & D) $\overline{z_d}$, and (E & F) U. These parameters are representative of the turbulence, mean atmospheric refractivity, and sea-state components, respectively. The dashed red line represents the geometric horizon, and the dotted horizontal red line represents the RF transmitter height (15 m).

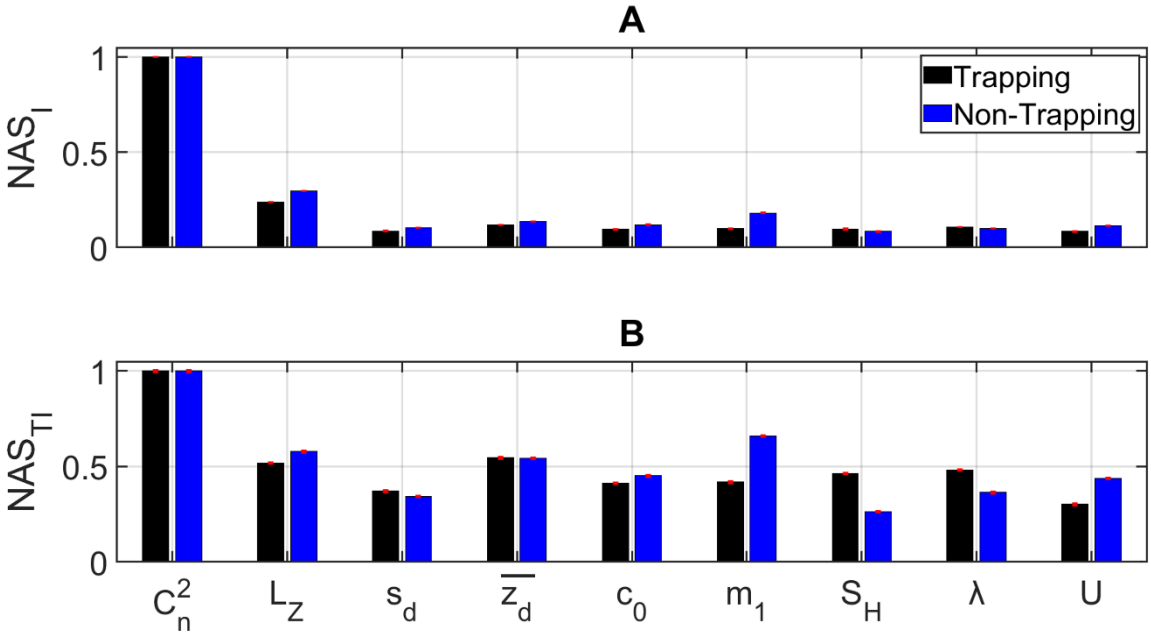

Figure 7.7. Unstable regime (A) first order (NAS_I) and (B) total-order (NAS_{TI}) sensitivity averaged over ranges and altitudes beyond-the-geometric horizon and normalized by the maximum S_I and S_{TI}, respectively, for trapping (16 m ≤ $\overline{z_d}$ < 30 m) and non-trapping (5 m < $\overline{z_d}$ ≤ 14 m) scenarios. Red error-bars denote 99% confidence intervals.

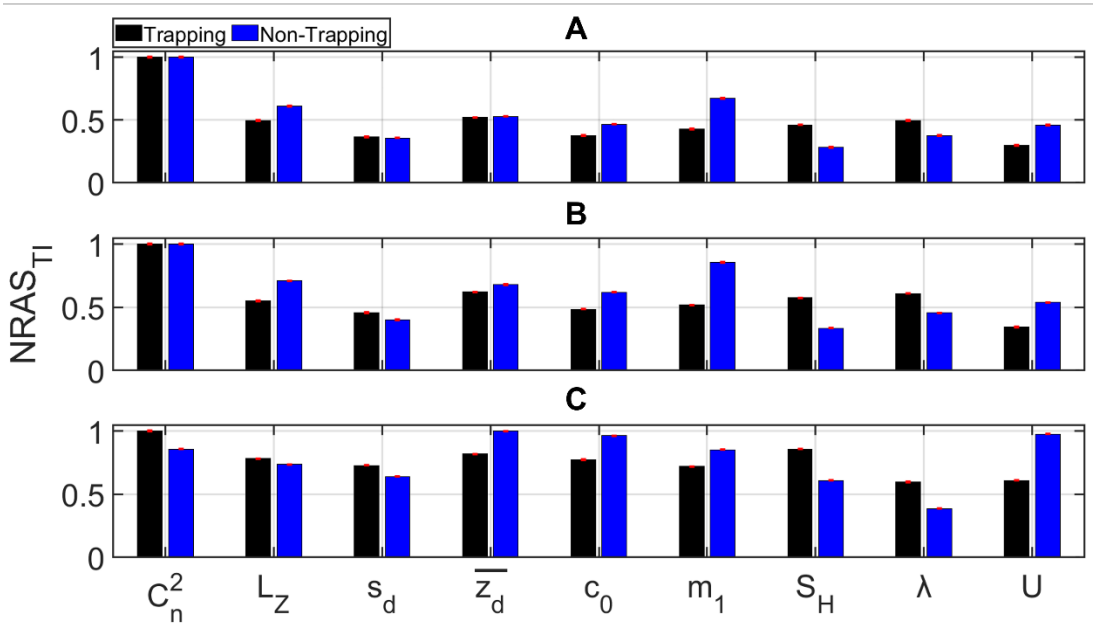

Figure 7.8. Unstable regime regionally averaged total-order sensitivity ($NRAS_{TI}$) averaged over ranges beyond-the-geometric horizon and altitudes of (A) 50 – 100 m, (B) 10 – 50 m, and (C) 2 – 10 m, normalized by the maximum average S_{TI} over all parameters for trapping and non-trapping scenarios. Red error-bars denote 99% confidence intervals.

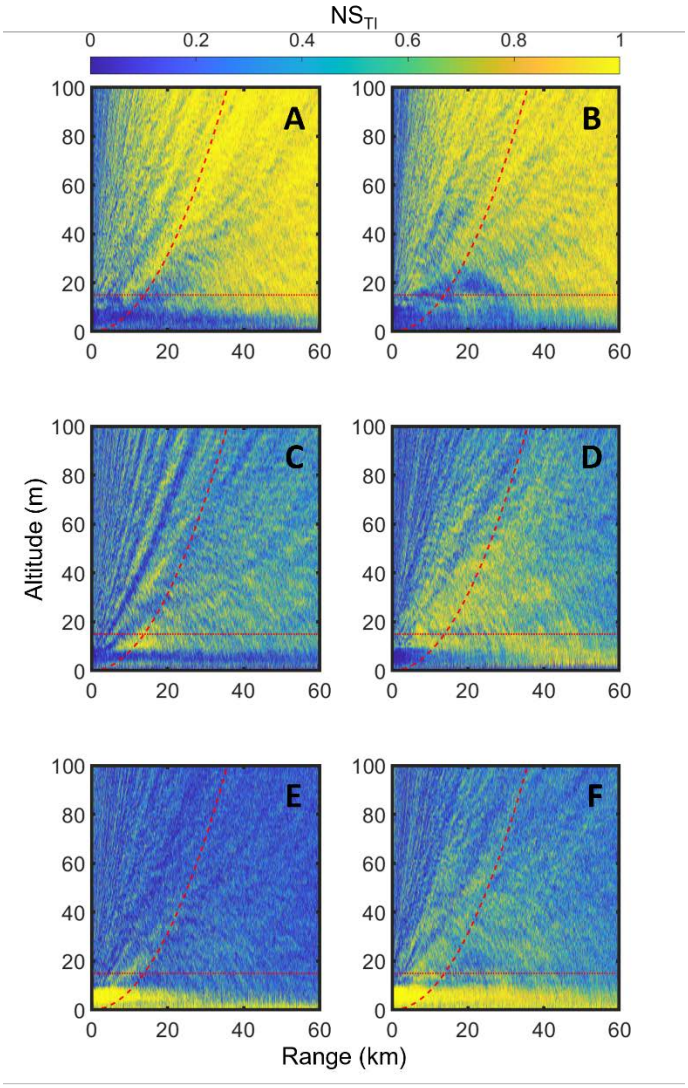

Figure 7.9. Unstable regime total-order sensitivity (S_{TI}) normalized by the largest magnitude S_{TI} over all parameters, at each range and altitude. Normalized sensitivities (NS_{TI}) are shown for trapping (A, C, and E) and non-trapping (B, D, and F) scenarios; parameters illustrated are (A & B) C_n^2, (C & D) $\overline{z_d}$, and (E & F) U. These parameters are representative of the turbulence, mean atmospheric refractivity, and sea-state components, respectively. The dashed red line represents the geometric horizon, and the dotted horizontal red line represents the RF transmitter height (15 m).

Chapter 8

Summary and Conclusions

Nomenclature	Definition
COAMPS®	Coupled Ocean-Atmosphere Mesoscale Prediction System
COARE	Coupled Ocean-Atmosphere Response Experiment
EDH	Evaporation Duct Height
EM	Electromagnetic
MAPS	Marine Atmospheric Profiling System
MASL	Marine Atmospheric Surface Layer
Tx	Transmitter Height

Accurate prediction of atmospheric refractivity and sea surfaces within the MASL are an essential part of optimizing X-band radar system performance in marine environments. Specifically, evaporation ducts are an essentially permanent feature over marine surfaces and can cause propagation anomalies. Characterization of EDs via evaporation duct height, curvature, and evaporation duct strength (or M-deficit) relate to mean characteristics of evaporation ducts. Variations not captured by the mean refractive environment – such as turbulent fluctuations and spatial heterogeneity in refractivity – may enhance the fidelity of propagation predictions if included. Estimation of the rough sea surface also impacts propagation predictions within the MASL. While these refractive and sea surface effects on propagation have been studied independently, their relative leading

order and coupled effects on X-band propagation predictions within the MASL have not been explored.

To this end, this dissertation addresses the following question: how does evaporation duct height and curvature, considered primary drivers of propagation variability, and turbulent refractivity fluctuations, refractivity heterogeneity, and sea state, considered secondary drivers of propagation variability, influence propagation within the MASL. Specifically, to what extent each needs to be accurately characterized to predict EM propagation to various accuracies. This question is detailed in Chapter 3, where the studies addressing associated dissertation objectives pertaining to the question are presented in Chapters 4-7.

Estimation of mean atmospheric refractivity, and subsequent effects on propagation, are explored in Chapters 4 and 5, where numerical weather prediction (COAMPS®), semi-empirical surface layer model (COARE), tethered-balloon-based meteorological measurements (MAPS), and RF inversion methods are compared. Limitations of refractivity modeled via COAMPS® and COARE are well documented for thermally stable atmospheric conditions and are corroborated in this work; as the environment becomes near neutral or thermally stable, agreement between *in-situ* refractive observations, the semi-empirical models, and the inversion degrades (Chapter 4 and 5). These discrepancies in refractivity are reflected in the respective EDH, profile curvature, and M-deficit parameters used to characterize the profiles.

The effects of mean EDH on propagation are well documented within the literature and are scrutinized throughout this dissertation. Along with investigation of mean refractive parameters in Chapters 4 and 5, Chapter 7 employs global sensitivity analysis

further exploring the effects of mean EDH on propagation, specifically beyond the geometric horizon. Comparison of multiple refractive estimation methods clearly showed that location of EDH relative to the Tx is of utmost importance and most influential on propagation predictions. Chapter 4 showed that when EDH > Tx from one method and EDH < Tx for another method, the largest discrepancies in propagation are observed. As a result, the sensitivity analysis experiments described in Chapter 7 were divided into two scenarios: Tx above the EDH and Tx below the EDH to remove this significant effect from saturating the results of the sensitivity analysis. The results showed that even with this large effect removed EDH can still have leading order effects relative to the other secondary effects due to phenomena like duct leakage being important. Chapter 7 showed that secondary effects of the EDH (i.e., duct leakage) due to the proximity of EDH to the transmitter greatly affect propagation variations, which can be seen anecdotally in the comparisons of individual propagation predictions in Chapter 4. This role of the EDH as a primary secondary influence on propagation is observed in stable and neutral environments. In stable environments, inversion-based EDH is shown to be higher than that from forward refractivity estimation methods, which resulted in more accurate propagation predictions at altitudes below 12 m. Further, the importance of EDH at low altitudes is confirmed in the sensitivity analysis, where the mean EDH parameter is the primary refractive parameter affecting propagation at altitudes $\leq$ 10 m in all stability regimes. While mean EDH is a primary driver of propagation variation, variations in EDH spatially do not tend to vary propagation substantially as shown by the sensitivity analysis presented in Chapter 7. This result is also illustrated in Chapter 5, where inversion-based refractivity propagation predictions, using only mean refractive parameters, better match

propagation measurements than forward modeled propagation employing refractivity with spatially varying EDH. Thus, accurate estimation of mean EDH is of primary importance for accurate prediction of propagation within the MASL.

Variations in propagation are also influenced by the gradients below the EDH, described by duct curvature, M-deficit (duct strength), and in parametric refractive models (Equation 7.8) by the parameter c_0. Comparison of different refractive estimation methods (Chapter 4) shows that, in non-trapping conditions, the effects of differences in duct strength between methods causes larger differences in propagation predictions relative to trapping conditions. This result is upheld in the sensitivity analysis for all stability regimes, where c_0 (akin to curvature of the ED) sensitivity is ranked higher relative to other mean parameters in non-trapping conditions. Furthermore, based on the sensitivity analysis, variations in propagation due to c_0 are most prominent in stable and neutral regimes where turbulence in the atmosphere is either suppressed or purely mechanical.

While turbulent variations are secondary to the mean evaporation duct properties, influence from turbulent fluctuations of heat and moisture can promote substantial variations in MASL refractivity. Direct observations of temperature and humidity show large variability, demonstrated in Chapter 6 with MAPS observations. These fluctuations were effectively modeled via a Turbulent Refractive Index Fluctuation (TRIF) model (Chapter 6). This model was subsequently implemented in the sensitivity analysis (Chapter 7). Results in Chapter 7 show that turbulent fluctuations of the refractive index can be a significant secondary source of propagation variability in unstable atmospheric conditions. This effect is pervasive throughout the modeled propagation domain but is most prevalent at higher altitudes and further ranges from the transmitter. At low altitudes, the role of

turbulence, even in unstable atmospheric regimes, is, at-most, similar to that of other factors, like mean refractive parameters. In neutral stabilities, turbulence model parameter sensitivities decline relative to unstable regimes but are still influential. Contrary, in stable regimes, turbulence has a rather insignificant effect on propagation due to the small fluctuations of the refractive index resulting from suppression of mechanical and thermal turbulence by the stable stratification.

Along with atmospheric refractivity, the rough sea surface has a significant role in varying propagation. Wind driven sea surface variability drives variations throughout the propagation domain, specifically near multipath nulls as reflected in the sensitivity analysis results. Sensitivity analysis also indicates swell characteristics of the sea surface can have first order effect on propagation, but interactive effects of refractive and sea state properties diminish the effects of swell, suggesting primary forward scattering effects on propagation from the sea surface are mostly related to smaller-scale wind waves versus swell. In all stability regimes, regional sensitivity analysis illustrates that low altitude (2 – 10 m) propagation is dominated by forward scattering from the sea surface, especially in trapping environments. Furthermore, the sensitivity study shows that relative to the included refractive characteristics (turbulence, spatial heterogeneity, and mean field), forward scattering from the wind driven sea surface is as important as other secondary effects on propagation within the MASL. Therefore, proper emulation of the sea surface as the bottom boundary is essential for the accurate prediction of propagation within the MASL.

The results described in this dissertation relate only to X-band propagation. Future work should investigate refractive and sea state effects on different radar frequencies as it is expected that results discussed herein will vary with the EM wave frequency. For

example, turbulence may have more relative influence on EM propagation at higher radar frequencies, and at lower frequencies, mean refractive characteristics may be more influential in varying propagation predictions. Such results would inform a wider range of communication and radar applications, and ultimately, contribute to a comprehensive understanding of EM propagation within the MASL.

References

Abdi, H., & Williams, L. J. (2010). Principal component analysis. Wiley interdisciplinary reviews: computational statistics, 2(4), 433-459.

Alappattu, D. P., Wang, Q., Rainer, R., Yamaguchi, R., & Lind, R. J. (2016). Characteristics of surface layer scalar profiles using the in-situ measurements from an undisturbed marine environment. In Proceedings of the 20th Conference on Air–Sea Interaction, 4.4.

Anderson, D. L. (1995). The tropical ocean global atmosphere program. Contemporary Physics, 36(4), 245-265.

Anderson, R., Vasudevan, S., Krolik, J. L., & Rogers, L. T. (2001, July). Maximum a posteriori refractivity estimation from radar clutter using a Markov model for microwave propagation. In IGARSS 2001. Scanning the Present and Resolving the Future. Proceedings. IEEE 2001 International Geoscience and Remote Sensing Symposium (Cat. No. 01CH37217) (Vol. 2, pp. 906-909). IEEE.

Babin, S. M., Young, G. S., & Carton, J. A. (1997). A new model of the oceanic evaporation duct. Journal of Applied Meteorology, 36(3), 193-204.

Banner, M. L., Jones, I. S., & Trinder, J. C. (1989). Wavenumber spectra of short gravity waves. Journal of Fluid Mechanics, 198, 321-344.

Barrios, A. E. (1994). A terrain parabolic equation model for propagation in the troposphere. IEEE Transactions on Antennas and Propagation, 42(1), 90–98.Bean, B. R., & Dutton, E. J. (1968). Radio Meteorology (1st ed.). Dover.

Beljaars, A. C. M., & Holtslag, A. A. M. (1991). Flux parameterization over land surfaces for atmospheric models. Journal of Applied Meteorology, 30(3), 327-341

Benhmammouch, O., Caouren, N., & Khenchaf, A. (2009). Influence of sea surface roughness on electromagnetic waves propagation in presence of evaporation duct. In 2009 International Radar Conference "Surveillance for a Safer World" (RADAR 2009) (pp. 1-6).

Brown, R. M., & Miller, A. R. (1974). Geometric-optics theory for coherent scattering of microwaves from the ocean surface. NAVAL RESEARCH LAB WASHINGTON DC.

Buck, A. L. (1981). New equations for computing vapor pressure and enhancement factor. Journal of Applied Meteorology, 20(12), 1527-1532.

Businger, J. A., Wyngaard, J. C., Izumi, Y., & Bradley, E. F. (1971). Flux-profile relationships in the atmospheric surface layer. Journal of the Atmospheric Sciences, 28(2), 181-189.

Cavaleri, L. (2006). Wave modeling: Where to go in the future. Bulletin of the American Meteorological Society, 87(2), 207-214.

Charnotskii, M. (2016). Wave propagation modeling with non-Markov phase screens. Journal of the Optical Society of America A, 33(4), 561.

Cherrett, R. C. (2015). Capturing characteristics of atmospheric refractivity using observations and modeling approaches [Doctoral dissertation, Naval Postgraduate School]. ProQuest Dissertations Publishing.

Chou, Y. H., & Kiang, J. F. (2014). Effect of turbulence on wave propagation in evaporation ducts above a rough sea surface. Forum for Electromagnetic Research Methods and Application Technologies, 12.

Compaleo, J., Yardim, C., Xu, L., Wijesundara, S., Johnson, J., & Burkholder, B. (2018). Preliminary refractivity from clutter (RFC) evaporation duct inversion results from CASPER west experiment. In Proceedings of the 2018 IEEE Radar Conference (pp. 1-6). IEEE.

Craig, K. H., & Levy, M. F. (1991, April). Parabolic equation modelling of the effects of multipath and ducting on radar systems. IEE Proceedings F (Radar and Signal Processing), 38(2), 153-162. https://doi.org/10.1049/ip-f-2.1991

Donelan, M. A., Hamilton, J., & Hui, W. (1985). Directional spectra of wind-generated ocean waves. *Philosophical Transactions of the Royal Society of London. Series A, Mathematical and Physical Sciences*, 315(1534), 509-562.

Dyer, A. J. (1974). A review of flux-profile relationships. Boundary-Layer Meteorology, 7(3), 363-372.

Edson, J. B., Zappa, C. J., Ware, J. A., McGillis, W. R., & Hare, J. E. (2004). Scalar flux profile relationships over the open ocean. Journal of Geophysical Research: Oceans, 109(C8).

Ekstrom, P. (n.d.). Eikos: A Simulation Toolbox for Sensitivity Analysis in MATLAB®. http://ecolego.facilia.se/ecolego/show/Sensitivity+analysis+toolbox/

Emes, M. J., Arjomandi, M., Kelso, R. M., & Ghanadi, F. (2019). Turbulence length scales in a low-roughness near-neutral atmospheric surface layer. Journal of Turbulence, 20(9), 545-562.

Fairall, C. W., Bradley, E. F., Hare, J. E., Grachev, A. A., & Edson, J. B. (2003). Bulk parameterization of air-sea fluxes: Updates and verification for the COARE algorithm. Journal of Climate, 16(4), 571-591.

Fairall, C. W., Bradley, E. F., Rogers, D. P., Edson, J. B., & Young, G. S. (1996). Bulk parameterization of air-sea fluxes for tropical ocean-global atmosphere coupled-ocean atmosphere response experiment. Journal of Geophysical Research: Oceans, 101(C2), 3747-3764.

Foken, T. (2006). 50 years of the Monin-Obukhov similarity theory. Boundary-Layer Meteorology, 119, 431-447.

Fountoulakis, V., & Earls, C. (2016). Inverting for maritime environments using proper orthogonal bases from sparsely sampled electromagnetic propagation data. IEEE Transactions on Geoscience and Remote Sensing, 54(12), 7166-7176.

Frederickson, P. (2016). Navy Atmospheric Measurements for EM Propagation Modeling. [Executive Summary]. Naval Postgraduate School.

Frederickson, P. A., Davidson, K. L., Zeisse, C. R., & Bendall, C. S. (2000). Estimating the refractive index structure parameter (Cn2) over the ocean using bulk methods. Journal of applied meteorology, 39(10), 1770-1783.

Frederickson, P. A., Hammel, S., & Tsintikidis, D. (2007). Improving bulk Cn2 models for over-ocean applications through new determinations of the dimensionless temperature structure parameter. In Atmospheric Optics: Models, Measurements, and Target-in-the-Loop Propagation (Vol. 6708, pp. 45-54). SPIE.

Freund, D. E., Woods, N. E., Ku, H. C., & Awadallah, R. I. S. (2006). Forward radar propagation over a rough sea surface: A numerical assessment of the Miller-Brown approximation using a horizontally polarized 3-GHz line source. IEEE Transactions on Antennas and Propagation, 54(4), 1292-1304.

Gao, Y., Shao, Q., Yan, B., Li, Q., & Guo, S. (2019). Parabolic Equation Modeling of Electromagnetic Wave Propagation over Rough Sea Surfaces. Sensors, 19, 1252. https://doi.org/10.3390/s19051252

Garratt, J. R. (1994). The atmospheric boundary layer. Earth-Science Reviews, 37(1-2), 89-134.

Geernaert, G. L. (2003). Surface layer. In Encyclopedia of atmospheric sciences (pp. 305-311). Academic Press.

Gerstoft, P., Rogers, L. T., Krolik, J. L., & Hodgkiss, W. S. (2003). Inversion for refractivity parameters from radar sea clutter. Radio Science, 38(3).

Gingras, D. F., Gerstoft, P., & Gerr, N. L. (1997). Electromagnetic matched-field processing: Basic concepts and tropospheric simulations. IEEE Transactions on Antennas and Propagation, 45(10), 1536-1545.

Goldberg, D. E. (1989). Genetic algorithms and Walsh functions: Part II, deception and its analysis. Complex Systems, 3, 153

Goldhirsh, J., & Dockery, D. (1998). Propagation factor errors due to the assumption of lateral homogeneity. Radio Science, 33(2), 239-249.

Gossard, E. E., & Strauch, R. G. (1983). Radar observation of clear air and clouds (Book). Amsterdam and New York, Elsevier Developments in Atmospheric Science., 14.

Grachev, A. A., Andreas, E. L., Fairall, C. W., Guest, P. S., and Persson, P. O. G. (2007). SHEBA flux–profile relationships in the stable atmospheric boundary layer. Boundary-Layer Meteorology, 124(3), 315-333.

Greenway, D. P. (2020). Parametric Model Development For Heterogeneous Atmospheric Conditions. Master Thesis, Coastal Carolina University.

Haack, T., Wang, C., Garrett, S., Glazer, A., Mailhot, J., and Marshall, R. (2010). Mesoscale modeling of boundary layer refractivity and atmospheric ducting. Journal of Applied Meteorology and Climatology, 49(12), 2437-2457.

Halliwell, G., R. Bleck, and E. Chassignet, (1998). Atlantic Ocean simulations performed using a new hybrid-coordinate ocean model. EOS, Trans. AGU, Fall 1998 AGU meeting.

Hitney, H. V. and R. Vieth, (1990). Statistical assessment of evaporation duct propagation. IEEE Trans. Antennas Propagation., Vol. 38, No. 6, 794–799.

Hitney, H. V., Richter, J. H., Pappert, R. A., Anderson, K. D., and Baumgartner, G. B. (1985). Tropospheric radio propagation assessment. Proceedings of the IEEE, 73(2), 265-283.

Hodur, R. M. (1997). The Naval Research Laboratory's coupled ocean/atmosphere mesoscale prediction system (COAMPS). Monthly Weather Review, 125(7), 1414-1430.

Hogan, T. F., Liu, M., Ridout, J. A., Peng, M. S., Whitcomb, T. R., Ruston, B. C., ... & McCormack, J. P. (2014). The navy global environmental model. Oceanography, 27(3), 116-125.

Ishimaru, A. (1978). Wave propagation and scattering in random media (Vol. 2). New York: Academic Press.

Ivanov, V. K., Shalyapin, V. N., & Levadny, Y. V. (2009). Microwave scattering by tropospheric fluctuations in an evaporation duct. Radiophysics and Quantum Electronics, 52(4), 277-286.

Johnson, J. M., & Rahmat-Samii, V. (1997). Genetic algorithms in engineering electromagnetics. IEEE Antennas and Propagation Magazine, 39(4), 7-21.

Kang, D., & Wang, Q. (2016). Optimized estimation of surface layer characteristics from profiling measurements. Atmosphere, 7(2), 14.

Karimian, A., Yardim, C., Gerstoft, P., Hodgkiss, W. S., & Barrios, A. E. (2011). Refractivity estimation from sea clutter: An invited review. Radio Science, 46(06), 1-16.

Karimian, A., Yardim, C., Haack, T., Gerstoft, P., Hodgkiss, W. S., & Rogers, T. (2013). Toward the assimilation of the atmospheric surface layer using numerical weather prediction and radar clutter observations. Journal of Applied Meteorology and Climatology, 52(10), 2345-2355. https://doi.org/10.1175/JAMC-D-12-0267.1

Kennedy, J., & Eberhart, R. (1995). Particle swarm optimization. In Proceedings of ICNN'95-international conference on neural networks (Vol. 4, pp. 1942-1948). IEEE. https://doi.org/10.1109/ICNN.1995.488968

Knepp, D. L. (1983). Multiple phase-screen calculation of the temporal behavior of stochastic waves. Proceedings of the IEEE, 71(6), 722-737.

Lentini, N. E., & Hackett, E. E. (2015). Global sensitivity of parabolic equation radar wave propagation simulation to sea state and atmospheric refractivity structure. Radio Science, 50(10), 1027-1049. https://doi.org/10.1002/2015RS005825

Levadnyi, I., Ivanov, V., & Shalyapin, V. (2012). Simulation of microwave propagation in turbulent evaporation duct. In 2012 6th European Conference on Antennas and Propagation (EUCAP) (pp. 1-3). IEEE. https://doi.org/10.1109/EuCAP.2012.6206222

Marino, S., Hogue, I. B., Ray, C. J., & Kirschner, D. E. (2008). A methodology for performing global uncertainty and sensitivity analysis in systems biology. *Journal of theoretical biology*, *254*(1), 178-196.

Marino, S., Hogue, I. B., Ray, C. J., & Kirschner, D. E. (2008). A methodology for performing global uncertainty and sensitivity analysis in systems biology. Journal of Theoretical Biology, 254(1), 178-196.

Matsko, I. J., & Hackett, E. E. (2019). Impact of radar data sampling on the accuracy of atmospheric refractivity inversions over marine surfaces. Radio Science, 54(7), 704-714. https://doi.org/10.1029/2019RS006827

Mukherjee, S., & Yardim, C. (2021). Accurate computation of scintillation in tropospheric turbulence with parabolic wave equation. IEEE Transactions on Antennas and Propagation, 69(8), 4748-4757.

Panofsky, H. A., & Dutton, J. A. (1984). Atmospheric turbulence: models and methods for engineering applications (No. 04; QC880.4.T8, P3). Wiley.

Pastore, D. M., Greenway, D. P., Stanek, M. J., Wessinger, S. E., Haack, T., Wang, Q., & Hackett, E. E. (2021). Comparison of atmospheric refractivity estimation methods and their influence on radar propagation predictions. Radio Science, 56(9), e2020RS007194. https://doi.org/10.1029/2020RS007194

Pastore, D. M., Wessinger, S. E., Greenway, D. P., Stanek, M. J., Burkholder, R. J., Haack, T., Wang, Q., & Hackett, E. E. (2022). Refractivity inversions from point-to-point X-band radar propagation measurements. Radio Science, 57(2), e2021RS007624. https://doi.org/10.1029/2021RS007624

Paulus, R. A. (1989). Specification for environmental measurements to assess radar sensors. NAVAL OCEAN SYSTEMS CENTER SAN DIEGO CA.

Paulus, R. A. (1990). Evaporation duct effects on sea clutter. IEEE Transactions on Antennas and Propagation, 38(11), 1765-1771. https://doi.org/10.1109/8.102474

Penton, S. E., & Hackett, E. E. (2018). Rough ocean surface effects on evaporative duct atmospheric refractivity inversions using genetic algorithms. Radio Science, 53(6), 804-819. https://doi.org/10.1029/2017RS006507

Percival, D. B. (1993). Simulating Gaussian random processes with specified spectra. In Computing Science and Statistics (Vol. 25, pp. 534-534). Interface Foundation.

Pierson Jr, W. J., & Moskowitz, L. (1964). A proposed spectral form for fully developed wind seas based on the similarity theory of SA Kitaigorodskii. Journal of Geophysical Research, 69(24), 5181-5190. https://doi.org/10.1029/JZ069i024p05181

Plant, W. J., & Irisov, V. (2017). A joint active/passive physical model of the sea surface microwave signatures. Journal of Geophysical Research: Oceans, 122, 3219–3239. https://doi.org/10.1002/2016JC012590

Poli, R., Kennedy, J., & Blackwell, T. (2007). Particle swarm optimization. Swarm Intelligence, 1(1), 33-57. https://doi.org/10.1007/s11721-007-0002-0

Pozderac, J., Johnson, J., Yardim, C., Merrill, C., de Paolo, T., Terrill, E., ... & Frederickson, P. (2018). X -Band Beacon-Receiver Array Evaporation Duct Height Estimation. IEEE Transactions on Antennas and Propagation, 66(5), 2545-2556. https://doi.org/10.1109/TAP.2018.2816219

Qing, C., Wu, X., Li, X., Tian, Q., Liu, D., Rao, R., & Zhu, W. (2017). Simulating the refractive index structure constant in the surface layer at Antarctica with a mesoscale model. The Astronomical Journal, 155(1), 37. https://doi.org/10.3847/1538-3881/aa971d

Rainer, R. B. (2016). In-situ observation of undisturbed surface layer scaler profiles for characterizing evaporative duct properties. Naval Postgraduate School Monterey United States.

Rogers, L. T., Hattan, C. P., & Stapleton, J. K. (2000). Estimating evaporation duct heights from radar sea echo. Radio Science, 35(4), 955-966. https://doi.org/10.1029/2000RS002272

Rogers, L. T., Jablecki, M., & Gerstoft, P. (2005). Posterior distributions of a statistic of propagation loss inferred from radar sea clutter. Radio Science, 40(6). https://doi.org/10.1029/2004RS003218

Rouseff, D. (1992). Simulated microwave propagation through tropospheric turbulence. IEEE Transactions on Antennas and Propagation, 40(9), 1076-1083. https://doi.org/10.1109/8.161362

Ryan, F. J. (1991). Analysis of electromagnetic propagation over variable terrain using the parabolic wave equation (No. NOSC/TR-1453). Naval Ocean Systems Center, San Diego, CA.

Saeger, J. T., Grimes, N. G., Rickard, H. E., & Hackett, E. E. (2015). Evaluation of simplified evaporation duct refractivity models for inversion problems. Radio Science, 50(10), 1110-1130. https://doi.org/10.1002/2015RS005741

Saltelli, A., Tarantola, S., & Chan, K. S. (1999). A quantitative model-independent method for global sensitivity analysis of model output. *Technometrics*, *41*(1), 39-56.

Saltelli, A., Tarantola, S., & Chan, K. S. (1999). A quantitative model-independent method for global sensitivity analysis of model output. Technometrics, 41(1), 39-56.

Sirkova, I. (2011). Propagation factor and path loss simulation results for two rough surface reflection coefficients applied to the microwave ducting propagation over the sea. Progress In Electromagnetics Research M, 17, 151–166.

Sirkova, I. (2012). Brief review on PE method application to propagation channel modeling in sea environment. Open Engineering, 2(1), 19-38. https://doi.org/10.2478/s13531-011-0037-5

Skolnik, M. I. (1990). Radar handbook (2nd ed.). McGraw-Hill.

Skolnik, M. I. (2001). RADAR systems. McGraw-Hill.

Stanek, M. J., Pastore, D. M., & Hackett, E. E. (2023). A Novel Near-Surface Wave-Coherent Instantaneous Profiling System for Atmospheric Measurements. Sensors, 23(8), 4099.

Tabrikian, J., & Krolik, J. L. (1999). Theoretical performance limits on tropospheric refractivity estimation using point-to-point microwave measurements. IEEE Transactions on Antennas and Propagation, 47(11), 1727–1734. https://doi.org/10.1109/8.806742

Tatarskii, V. I. (1971). The effects of the turbulent atmosphere on wave propagation. Israel Program for Scientific Translations.

Tepecik, C., & Navruz, I. (2018). A novel hybrid model for inversion problem of atmospheric refractivity estimation. International Journal of Electronics and Communications, 84, 258–264. https://doi.org/10.1016/j.aeue.2017.11.027

Turton, J. D., Bennetts, D. A., & Farmer, S. G. (1988). An introduction to radio ducting. Meteorological Magazine, 117(1393), 245-254.

Ulate, M., Wang, Q., Haack, T., Holt, T., & Alappattu, D. P. (2019). Mean Offshore Refractive Conditions during the CASPER East Field Campaign. Journal of Applied Meteorology and Climatology, 58(4), 853-874. https://doi.org/10.1175/JAMC-D-18-0141.1

VanZandt, T. E., Green, J. L., Gage, K. S., & Clark, W. L. (1978). Vertical profiles of refractivity turbulence structure constant: Comparison of observations by the Sunset radar with a new theoretical model. Radio Science, 13(5), 819-829. https://doi.org/10.1029/RS013i005p00819

Wagner, M., Gerstoft, P., & Rogers, T. (2016). Estimating refractivity from propagation loss in turbulent media. Radio Science, 51(12), 1876-1894. https://doi.org/10.1002/2016RS006048

Wang, Q., Burkholder, R. J., Yardim, C., Xu, L., Pozderac, J., Christman, A., ... & Wang, Q. (2019). Range and height measurement of X-band EM propagation in the marine atmospheric boundary layer. IEEE Transactions on Antennas and Propagation, 67(4), 2063-2073. https://doi.org/10.1109/TAP.2019.2897792

Wang, Qing, Denny P. Alappattu, Stephanie Billingsley, Byron Blomquist, Robert J. Burkholder, Adam J. Christman, Edward D. Creegan et al. (2018). CASPER: Coupled air–sea processes and electromagnetic ducting research. Bulletin of the American Meteorological Society, 99(7), 1449-1471.

Wang, Qing, Kyle Franklin, Ryan Yamaguchi, David G. Ortiz-Suslow, Denny P. Alappattu, Caglar Yardim, and Robert Burkholder (2018). Ducting conditions during

casper-west field campaign. In 2018 IEEE International Symposium on Antennas and Propagation & USNC/URSI National Radio Science Meeting, pp. 877-878. IEEE.

Webster, Peter J., and Roger Lukas (1992). TOGA COARE: The coupled ocean–atmosphere response experiment. Bulletin of the American Meteorological Society, 73(9), 1377-1416.

Wessinger, S. E. (2022). Improving near Surface Refractivity Estimates in Marine Environments. Master Thesis, Coastal Carolina University.

Whalen, J. D. (1998). Comparison of evaporation duct height measurement methods and their impact on radar propagation estimates. Naval Postgraduate School, Monterey, CA.

Wheelon, Albert D. (2001). Electromagnetic scintillation: volume 1, geometrical optics. Cambridge University Press.

Xiao-Feng, Z., Si-Xun, H., Jie, X., & Wei-Lai, S. (2011). Remote sensing of atmospheric duct parameters using simulated annealing. Chinese Physics B, 20(9), 099201.

Xu, L., Yardim, C., & Haack, T. (2022). Evaluation of COAMPS boundary layer refractivity forecast accuracy for 2–40 GHz electromagnetic wave propagation. Radio Science, 57(6), e2021RS007404.

Yang, Zixuan, Antoni Calderer, Sida He, Fotis Sotiropoulos, James D. Doyle, David D. Flagg, Jamie MacMahan, Qing Wang, Brian K. Haus, Hans C. Graber, and Lian Shen (2018). Numerical Study on the Effect of Air–Sea–Land Interaction on the Atmospheric Boundary Layer in Coastal Area. Atmosphere, 9(2), 51. https://doi.org/10.3390/atmos9020051

Yardim, C., Gerstoft, P., and Hodgkiss, W. S. (2009). Sensitivity analysis and performance estimation of refractivity from clutter techniques. Radio Science, 44(1).

Yue, P., and Yuanliang, M. (2006). Modelling evaporation duct effects on microwave propagation with experiment validation. In 2006 IEEE 7th International Symposium on Antennas, Propagation and EM Theory (pp. 1-4). October.

Zhang, J. P., Wu, Z. S., Zhu, Q. L., and Wang, B. (2011). A four-parameter M-profile model for the evaporation duct estimation from radar clutter. Progress In Electromagnetics Research, 114, 353-368.

Zhang, Q., & Yang, K. (2018). Study on evaporation duct estimation from point-to-point propagation measurements. IET Science Measurement & Technology, 12(4), 456–460. https://doi.org/10.1049/iet-smt.2017.0195

Zhang, Q., Yang, K., & Yang, Q. (2017). Statistical analysis of the quantified relationship between evaporation duct and oceanic evaporation for unstable conditions. Journal of Atmospheric and Oceanic Technology, 34(11), 2489-2497. https://doi.org/10.1175/JTECH-D-17-0071.1

Zhang, Z., Sheng, Z., Shi, H., & Fan, Z. (2016). Inversion for refractivity parameters using a dynamic adaptive cuckoo search with crossover operator algorithm. Computational Intelligence and Neuroscience, (10), 2016. https://doi.org/10.1155/2016/5979621

Zhao, X. (2012). Evaporation duct height estimation and source localization from field measurements at an array of radio receivers. IEEE Transactions on Antennas and Propagation, 60(2), 1020–1025. https://doi.org/10.1109/TAP.2011.2173437

Zhao, X., & Huang, S. (2012). Estimation of atmospheric duct structure using radar sea clutter. Journal of the Atmospheric Sciences, 69(9), 2808-2818. https://doi.org/10.1175/JAS-D-11-0255.1

Zhao, X., Huang, S., & Du, H. (2011). Theoretical analysis and numerical experiments of variational adjoint approach for refractivity estimation. Radio Science, 46, RS1006. https://doi.org/10.1029/2010RS004564

Zhao, X., Yardim, C., Wang, D., & Howe, B. M. (2017). Estimating range-dependent evaporation duct height. Journal of Atmospheric and Oceanic Technology, 34(5), 1113-1123. https://doi.org/10.1175/JTECH-D-16-0193.1